University of Science and Technology of China

Hefei, CHINA

Direct virtual photon production in Au+Au collisions at $\sqrt{s_{NN}}$ = 200 GeV at RHIC

A dissertation submitted

for the degree of

Doctor of Philosophy in Physics

by

Chi Yang

Co-supervisors: Cheng Li, Lijuan Ruan

2014

Dedicated to my dear family

谨献给我亲爱的父母

摘要

大爆炸理论预言在大爆炸发生后约几十微秒的宇宙早期会产生一种特殊的物质形态-夸克胶子等离子体(QGP). 格点QCD计算预言了在高温和低重子密度的条件下的从普通强子物质到这种夸克解禁闭的局部热平衡物质的相变. 位于美国布鲁克海文国家实验室(BNL) 的相对论重离子对撞机(RHIC) 通过高能重离子碰撞提供了一个在实验室中研究这种强关联的夸克胶子等离子体的环境, 研究其行为和性质成为物理学家们非常感兴趣的课题. 这种物质会以直接光子和双轻子的方式发射热辐射. 作为电弱相互作用探针, 因为不参与强相互作用, 直接光子和轻子一旦产生在穿越相对论重离子碰撞产生的高温高密物质时只受到很小的相互作用. 它们被认为能够携带从各个碰撞演化过程中的信息, 对其的研究能够反映碰撞系统最直接最纯净的信息.

本文给出了位于RHIC的螺旋管径迹探测器(STAR)中直接虚光子的首次测量. 这也是在高横动量下首次基于虚光子方法的直接光子测量. 测量是基于2010年与2011 年采集的每核子对质心能量200 GeV的金核金核碰撞数据, 给出了直接虚光子的不变产额及其与单举光子的比例. 这种基于虚光子方法测量的直接光子被称为直接虚光子. 其在横动量区间$1 < p_T < 10\ GeV/c$ 的测量来源于对低不变质量区间的双电子的测量. 2010 年安装完毕的飞行时间谱仪(TOF) 提供了从低到中横动量区间的干净的电子鉴别, 使得双电子的测量成为可能.

观测到的直接虚光子的产额谱在低横动量区间比从质子质子碰撞结果得到的预期有明显的升高. 这种升高说明了在此区间中存在物质热化的贡献. 不变产额谱与理论计算得到的预期向符合, 其包含QGP, 强子气体(hadron gas) 和原初产生的贡献. 在高横动量区间, 直接虚光子的产额谱符合从质子质子碰撞结果得到的预期. 这说明在此区间来自于物质热辐射的贡献非常微弱. 对直接虚光子的测量提供了两个动力学区间: 一个是可以对热化物质进行研究的低横动量区间, 一个是可以研究原初过程中部分子的硬散射的高横动量区间. 一个与初始温度相关的逆坡度参数也可以从不变产额谱中得到.

关键词：直接虚光子, 双电子, 电子鉴别, 夸克胶子等离子体, 热辐射

ABSTRACT

The Big-Bang theory indicates that the Quark Gluon Plasma (QGP) is formed at the very universe in a few tens of microseconds. Lattic QCD predicts a phase transition from hadronic matter to this deconfined and locally thermalized matter at high temperature and low baryon density. Relativistic Heavy Ion Collider (RHIC) at Brookhaven National Laboratory (BNL) provides an opportunity to study this strongly coupled QGP. The research of the behavior and property of QGP is a very interesting topic for physicist. This medium is expected to emit thermal radiation which is in the form of direct photons and dileptons. As electroweak probes, which do not suffer strong interaction, direct photon and lepton will traverse the hot and dense medium created by heavy ion collisions with minimal interactions once they are produced. They are believed to bring the information from all the evolution steps. The research on these probes will provide the most direct and pure information.

In this thesis, the first measurement on direct virtual photon from Solenoidal Tracker at RHIC (STAR) is reported. This measurement is also the first high transverse momentum (p_T) result on direct photon via virtual photon method. This analysis is based on the data of $\sqrt{s_{NN}} = 200\ GeV$ Au+Au collisions taken from year 2010 run and year 2011 run (Run10 and Run11). The invariant yield of direct virtual photon and the fraction of direct virtual photon versus inclusive photon are presented. This direct photon measured by virtual photon method is called direct virtual photon. Its production in the range of $1 < p_T < 10\ GeV/c$ is derived from the di-electron continuum in the low di-electron invariant mass region. The fully installed Time-of-Flight Detector (TOF) in 2010 provides clean electron identification from low to intermediate p_T which enables the di-electron measurement.

From the direct virtual photon invariant yield spectra, a significant enhancement compared to the prediction based on $p+p$ results is observed for $1 < p_T < 4\ GeV/c$. The

invariant yield is consistent with model prediction which includes the contributions from QGP, hadron gas and primordial production. In the high p_T range, the invariant yield is consistent with the N_{coll} scaled $p+p$ results. This indicates a negligible contribution from thermal radiation. The study on the direct virtual photon provides two kinematic ranges: the low p_T range where the thermal matter can be studied, the high p_T range where the hard parton scattering from primordial step can be studied. The inverse slope parameter which is related to the initial temperature is obtained from the invariant yield spectra.

Key word: direct virtual photon, di-electron, electron identification, quark gluon plasma, thermal radiation

Table of Contents

List of Figures

List of Tables

CHAPTER 1

Introduction

1.1 Standard Model and Quantum Chromodynamics

1.1.1 Standard Model

We human beings never stop to explore on the world we live in. Where did the universe come from? What are the fundamental components of the matter? After the electron was discovered in 1897, other particles such as proton and neutron were discovered. Standard Model (SM) is used to describe the fundamental interaction including the electromagnetic, weak, and strong nuclear interactions. The current formulation was finalized in the mid-1970s and explained the experiment results well such as the prediction for the top quark (discovered in 1995), the tau neutrino (discovered in 2000), and the Higgs boson (discovered in 2013).

The Standard Model includes 12 fermions with spin 1/2. Each fermion has a corresponding antiparticle. There are 6 quarks (*up*, *down*, *charm*, *strange*, *top*, *bottom*) and 6 leptons (e, μ, τ and their corresponding neutrinos) which form as 3 generations. The 4 gauge bosons which are the propagators of the interaction between fermions are also predicted in Standard Model. Fig. 1.1 shows these particles in 3 generations. The details properties such as mass, charge and spin are included.

Six quarks are involved in the electromagnetic, weak, and strong nuclear interactions. Six leptons don't have strong nuclear interaction while three neutrinos don't participant in the electromagnetic interaction. The electromagnetic interaction can be described by Quantum Electrodynamics (QED) with the zero mass photon as the propagator. $W^{\pm}, Z^0$

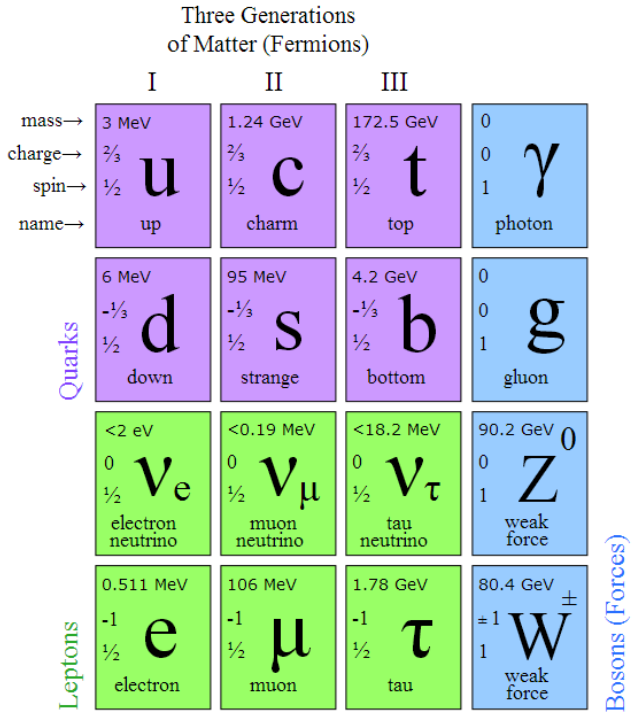

Figure 1.1: The fundamental particles in Standard Model.

are the propagators for weak interaction while the gluon propagates the strong interaction.

1.1.2 Quantum Chromodynamics

Quantum Chromodynamics (QCD) [FG72] is part of the Standard Model that describes the strong forces. The QCD Lagrangian can be written as:

$$\mathcal{L}_{QCD} = -\frac{1}{4}F^{(a)}_{\mu\nu}F^{(a)\mu\nu} + i\sum_q \bar{\psi}^i_q \gamma^\mu (D_\mu)_{ij}\psi^j_q - \sum_q m_q \bar{\psi}^i_q \psi^i_q \tag{1.1}$$

$$F^{(a)\mu\nu} = \partial A^a_\nu - \partial A^a_\mu - g_s f_{abc} A^b_\mu A^b_\nu, \tag{1.2}$$

$$(D_\mu)_{ij} = \delta_{ij}\partial_\mu + i g_s \sum_a \frac{\lambda^a_{ij}}{2} A^a_\mu, \tag{1.3}$$

g_s in Eq. 1.2 is the QCD coupling constant, and the f_{abc} are the structure constants

of the $SU(3)_C$ algebra. γ^μ are the Dirac matrices and $\psi_q^i(x)$ are the 4-component Dirac spinors associated with each quark field of color i and flavor q. The field strength tensor $F^{(a)\mu\nu}$ describes the interaction between gluons. $(D_\mu)_{ij}$ is the covariant derivative with the Gell-Mann matrices λ^i and the Yang-Mills (gluon) fields $A_\mu^a(x)$.

1.1.3 Asymptotic freedom

One peculiar property for strong interaction described by QCD is asymptotic freedom. The static QCD potential can be described as Eq. 1.4.

$$V_s = -\frac{4}{3} \times \frac{\alpha_s}{r} + k \times r \tag{1.4}$$

The first term contributes as the dominant source at small distance. The second term is related to the confinement of quarks and gluons inside hadrons.

The renormalized effective QCD coupling α_s is similar to that in QED (running coupling). The coupling can be expressed as:

$$\alpha_s(\mu) \equiv \frac{g_s^2(\mu)}{4\pi} \approx \frac{4\pi}{\beta_0 \ln(\mu^2/\Lambda_{QCD}^2)} \tag{1.5}$$

As seen from the equation, with the constant $\beta_0 > 0$, the α_s decreases with the increased μ which gives the asymptotic freedom property [GW73b, Pol73, GW73a, HP74]. This means QCD can be calculated perturbatively in high momentum transfer or short distance approach (pQCD). Fig. 1.2 shows the summary of the measurements all over the world.

1.1.4 Quark-gluon plasma and deconfinement

The color charged particles such as quarks and gluons can not be isolated and observed directly. This phenomenon is called confinement which is due to the color charge of gluons. When two quarks separate, the gluon fields form narrow strings of color charge and forces

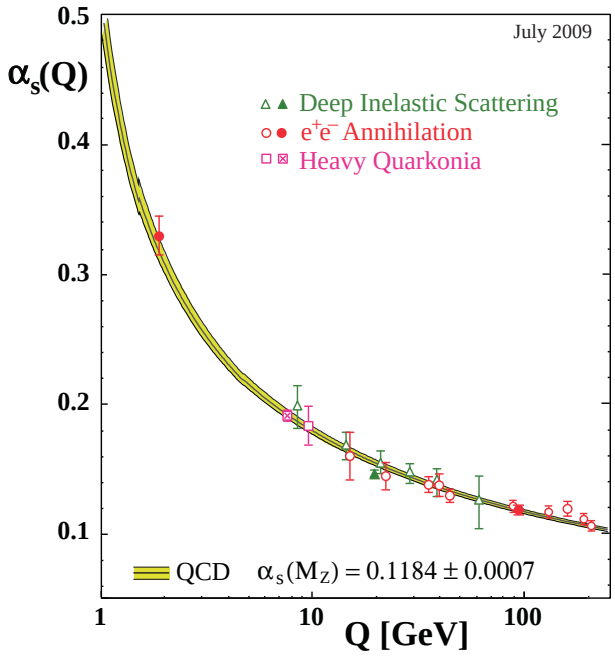

Figure 1.2: Summary of measurements of α_s as a function of the respective energy scale Q. The figure is taken from [Bet09].

the quarks back together. This process is different from the electromagnetic interaction and like that there is a "rubber band" between quarks. If these two quarks have energies large enough, when the "rubber band" is pulled apart, some new quark/anti-quark pairs will appear out of the vacuum to avoid the quarks separating further. So the observation of the quarks generated in high energy will give a cluster-like *jet* which is color-neutral. This is called hadronizaiton.

If the energy density is large enough, the quarks and gluons can move freely compared to the nucleon size (∼1fm). This new phase of matter is called quark-gluon plasma (QGP) while the process from confinement to "free" is called deconfinement. The deconfinement of quarks and gluons in the QGP matter looks like the free fully ionized electrons in the real plasma. Lattice QCD [Gup98] promises a phase transition from hadron gas to QGP matter at high temperature and/or baryon density. The study on this phase transition is one of the most important purposes of heavy ion collisions.

Fig. 1.3 shows a schematic view of the QCD phase diagram which is in [μ_B (baryon chemical potential), $T(temperature)$] plane. A boundary divides the region of matter into

two parts: hadron gas dominated by the hadronic degrees of freedom, quark-gluon plasma which is dominated by quark-gluonic degrees of freedom. This boundary is the first order phase transition line. The "Critical Point" on the boundary predicted by lattice QCD which means the ends of the first order phase transition is on the boundary. When μ_B is very close to 0, the phase transition will be a rapid crossover starting from the critical point.

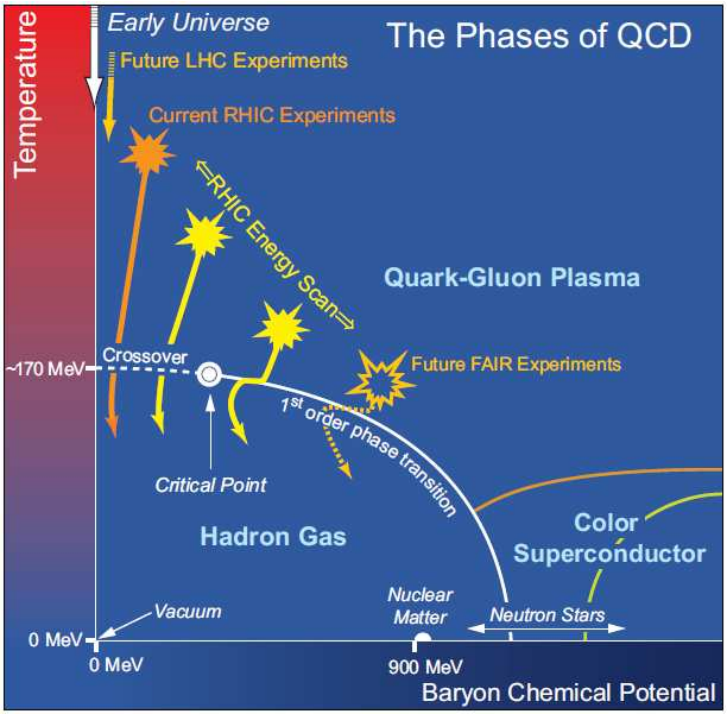

Figure 1.3: Schematic view of the QCD phase diagram. The figure is taken from [Das09].

1.2 Ultra-relativistic Heavy Ion Collisions

As shown in Fig. 1.3, there are two ways to study the QCD phase diagram. One is via the path with high temperature and low μ_B and the other is to study in low temperature and high μ_B condition. The first condition is like the very early universe while the second condition can be found in neutron star which is compressed by its own weight. The Relativistic Heavy Ion Collider (RHIC) at Brookhaven National Laboratory (BNL) is designed for the first way to study the QCD phase diagram and QGP matter. The details

can be found in Chap. 2.

1.3 Di-lepton Measurements

Di-lepton is an ideal probe to study the fundamental properties of the hot and dense medium created in the ultra-relativistic heavy-ion collisions. As can be produced at all stages of the medium evolution and traverses the strongly interacting medium with minimal interactions (only affected by electro-magnetic interaction), it can bring the information of the whole time evolution and dynamics of the medium. The larger the di-lepton pair invariant mass is, the earlier it is produced.

Fig. 1.4 is a schematic view of the di-lepton invariant mass distribution in the ultra-relativistic heavy-ion collisions. The di-lepton from Drell-Yan annihilation between the quark and anti-quark in the colliding nucleons is a dominant source in $M_{ee} > 3\ GeV/c^2$ (high mass region, HM). Other contributions in HM come from the heavy quarkonium (J/ψ and $\psi^{'}$).

In the intermediate mass region (IMR) $1.1 < M_{ee} < 3\ GeV/c^2$, the dominant source is the semi-leptonic decays of charm, bottom hadrons and the QGP thermal radiations. $g\overline{g} \rightarrow c\overline{c}$ shows the generation process for a charm quark pair. The open charm meson pair ($D\ and\ \overline{D}$) will be generated accordingly by the combination of these heavy flavor charms with light flavor quarks. The open charm mesons will emit leptons from weak decays respectively and form a correlated lepton pair. The bottom quark has a similar process to charm. If the lepton pair from charm and bottom sources can be rejected, the QGP thermal radiations contribution left in IMR can be studied more precisely. These thermal di-lepton are considered to bring the information of temperature and radial flow of the thermalized partonic matter. But unfortunately, the background from open charm and bottom impacts a lot and can not be directly measured from their final produced lepton pair. To distinguish this, a Muon Telescope Detector (Chap. 3) is designed and fully installed at the STAR experiment (Sec. 2.2). The dominant source of correlated electron-muon pairs is the semi-lepton decay from open charm and bottom. The measurement of

electron-muon correlation can give the background of thermal radiation in IMR.

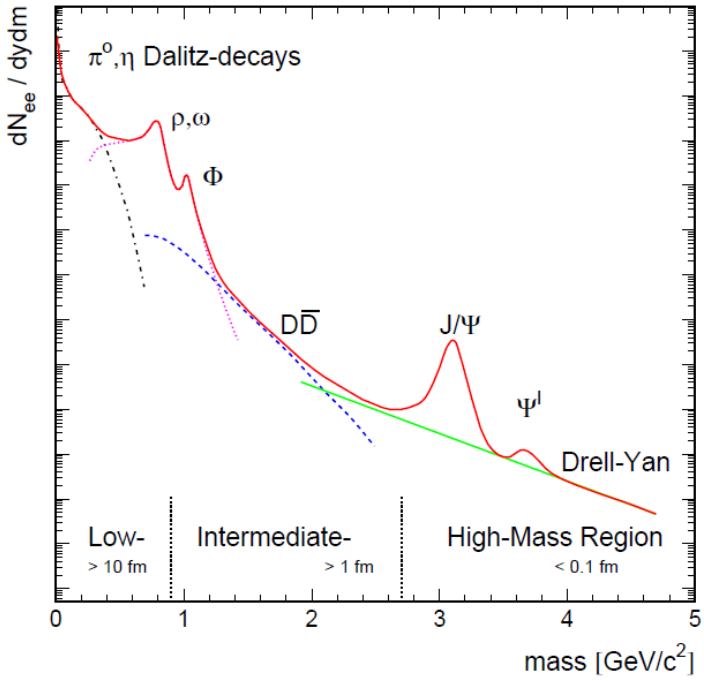

Figure 1.4: Schematic view of the di-lepton invariant mass distribution in the ultra-relativistic heavy-ion collisions. . The figure is taken from [Her01].

In the low mass region (LMR) $M_{ee} < 1.1\ GeV/c^2$), the dominant source is the soft process: Dalitz decays of neutral mesons such as π^0, η, η', ω *and* ϕ and the two body decays of resonance such as ρ, ω *and* ϕ. The short life time (1.3 fm/c) ρ which is strongly coupled with the $\pi\pi$ annihilation is a good probe to study the chiral symmetry and the properties of the medium [Pis82, RW00, Rap02].

1.4 Direct Photon Measurements

Direct photons are all of the photons that arise from processes during the collision, rather than from decays of hadrons. For example, many photons come from the quark-gluon Compton scattering process: $g + g \rightarrow g + \gamma$ and the quark annihilation $q + \overline{q} \rightarrow g + \gamma$. Photon which does not suffer strong interaction is another clean probe for the research of the hot and dense QGP created by the heavy ion collisions. For the minimum interaction, the photon in different transverse momentum (p_T) can access

the properties of the medium in different evolution steps. In low p_T range, the dominant source of direct photon is the thermal radiation from the partonic and hadronic phases. In high p_T range, most direct photons come from the initial hard scattering of the quarks or gluons. In low p_T range, the measurement on the direct photon can study the in-medium effect. The measurement of the photons from QGP thermal radiation can provide a deep looking into the QGP matter. The excess of direct photon in heavy ion collisions compared to N_{coll} scaled $p+p$ results in the QGP thermal kinematics range is observed. This can present a slope temperature with is related to the initial temperature of the medium. The production comparison to $p+p$ results may be also affected by modification of the initial state of the colliding nuclei such as shadowing and antishadowing, the difference between the isospin composition of the colliding nuclei to proton [Arl06].

1.4.1 Measurement methods

Photon is a neutral boson both on charge and color charge with zero mass. It should not interacted with the medium strongly when traversing. It will not bend by the magnetic field, so the momentum can not be reconstructed directly from the helix in magnetic field. Also the detectors which only give the measurements on charged particles can not measure the photon directly. One method for the direct photon measurement is to measure the deposit energy and shower size with calorimeter on the real photon. Another way is to measure its associated virtual photons which can convert to e^+e^- pair. With the measurement of the di-electron pair in the relative invariant mass region, the production of the virtual photon can be deduced by the calculation from QED. With a certain assumption of relationship between direct photon and the associate virtual photon, the direct photon can be produced. In this analysis, the second method is used to generate the direct photon. The detail can be found in Sec. 4.7.

1.4.2 Previous experimental results

In recent years, direct photon is measured in some experiments such as CMS [Cha08] and ALICE [Ver09] at LHC [Eng05] and PHENIX [Adc03] at RHIC [Lud03]. For CMS measurements, the kinematic range is in several tens of GeV while ALICE extended this measurement via real photon to low p_T. For PHENIX measurements, in the low p_T range $1 < p_T < 5$ GeV/c, the method is the virtual photon method which is same to this analysis. In the p_T range $5 < p_T < 20$ GeV/c, the PHENIX group used direct measurement on real photon.

1.4.2.1 PHENIX results

PHENIX collaboration studied direct photon production from p+p, d+Au and Au+Au. The low mass di-electron continuum for $p+p$ and Au+Au can be found in Fig. 1.5. The fraction of direct photon versus inclusive photon from PHENIX is shown in Fig. 1.6 while the yields from $p+p$ and d+Au are shown in Fig. 1.7. For the fraction measurements, the results from PHENIX are consistent with the NLO pQCD calculation in $p+p$ and d+Au. In Au+Au collisions, the fraction is larger than the NLO pQCD prediction for $p_T < 3.5$ GeV/c. An enhanced yield above N_{coll} scaled $p+p$ yield is observed in $1.0 < p_T < 2.5$ GeV/c (Right panel of Fig. 1.7) while there is no similar enhancement in d+Au collisions.

The nuclear modification factor is also studied. Fig. 1.8 shows the PHENIX results for d+Au and Au+Au collisions. As shown on the upper panel, R_{dA} is consistent with unity within the reported uncertainty. Within uncertainties, the data are consistent with these theoretical calculations and do not have sufficient precision to resolve the considered initial-state effects across the entire p_T range [AAA13]. The figure on the lower panel shows a much larger enhancement for $p_T < 2$ GeV/c in Au+Au collisions. This indicates that theoretical calculations assuming standard cold-nuclear-matter (CNM) effects describe the d+Au data well for the entire p_T range and the large enhancement of direct photons observed in Au+Au collisions for low p_T range is attributable to a source other than the initial-state nuclear effects.

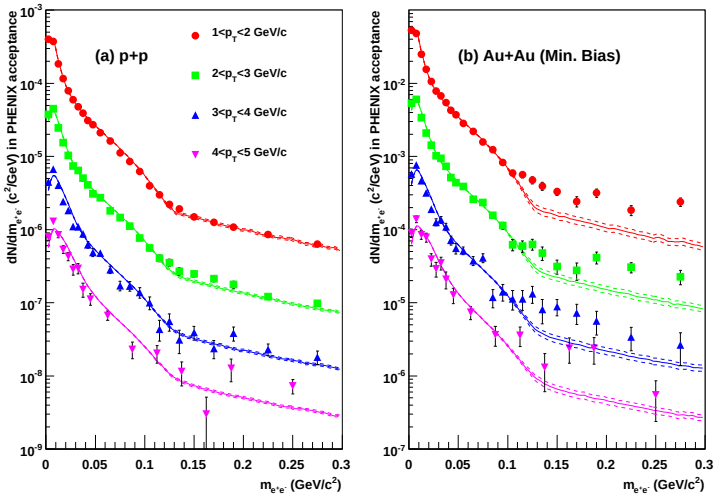

Figure 1.5: Di-electron continuum in different p_T slices for $p+p$ and Au+Au 200 GeV data from PHENIX. The plot is obtained from [Ada10b].

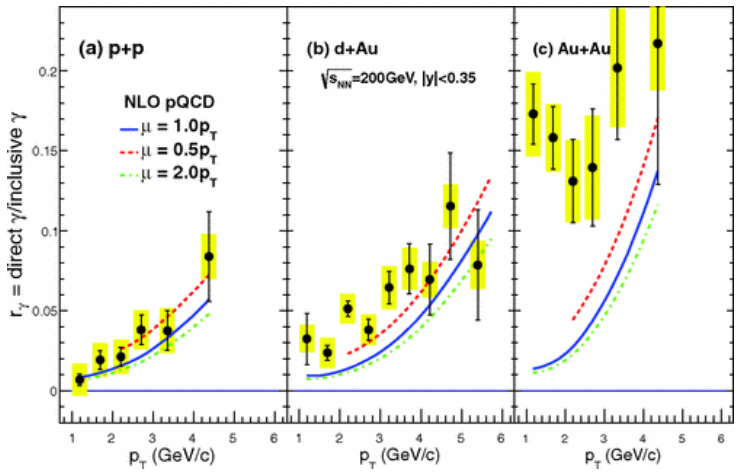

Figure 1.6: The direct photon fractions from the virtual photon analysis as a function of p_T in (a) $p+p$, (b) d+Au, and (c) Au+Au (MB) collisions. The statistical and systematic uncertainties are shown by the bars and bands, respectively. The curves show expectations from a NLO pQCD calculation [VZ08] with different cutoff mass scales: (solid line) $\mu = 1.0p_T$, (dashed line) $\mu = 0.5p_T$, and (dash-dotted line) $\mu = 2.0p_T$. The figure is obtained from [AAA13].

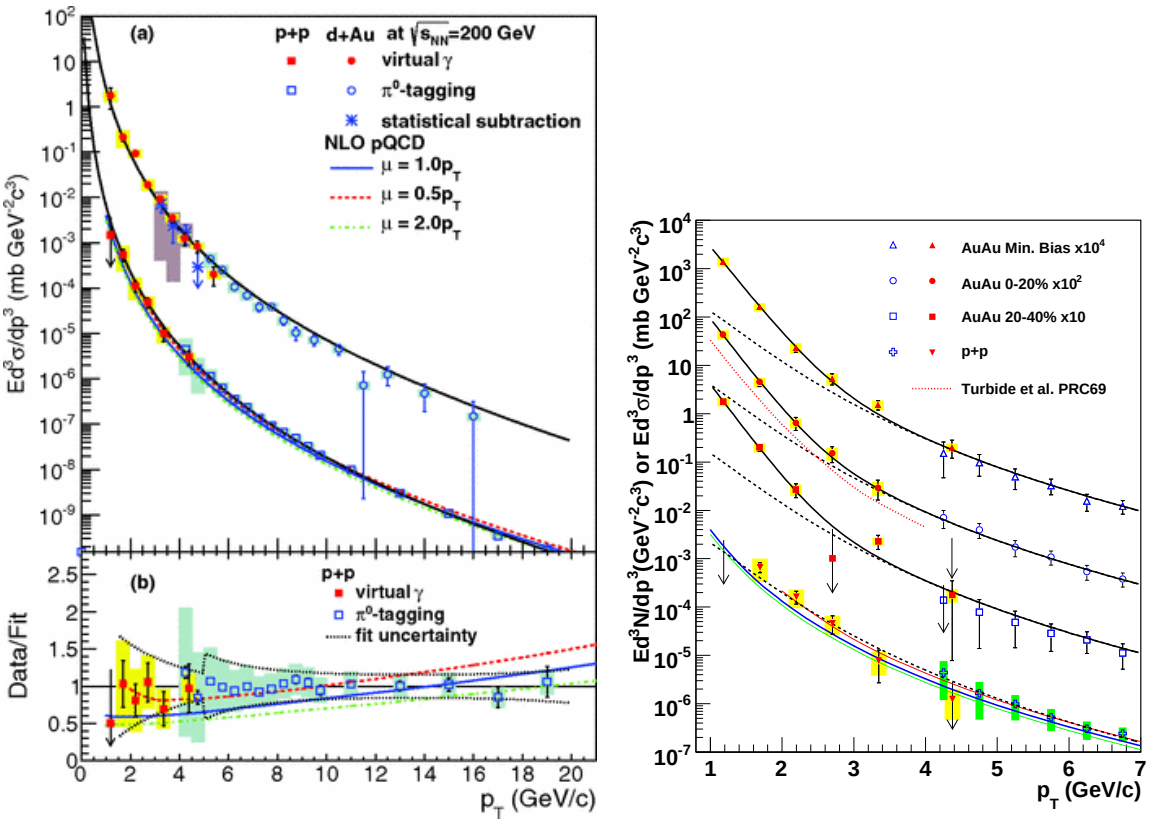

Figure 1.7: The direct photon yields in $p+p$, d+Au and Au+Au collisions at at $\sqrt{s(s_{NN})} = 200GeV$. Left panel shows the d+Au results compared to $p+p$ results. The figure is obtained from [AAA13]. Right panel shows the Au+Au results. The figure is obtained from [Ada10b].

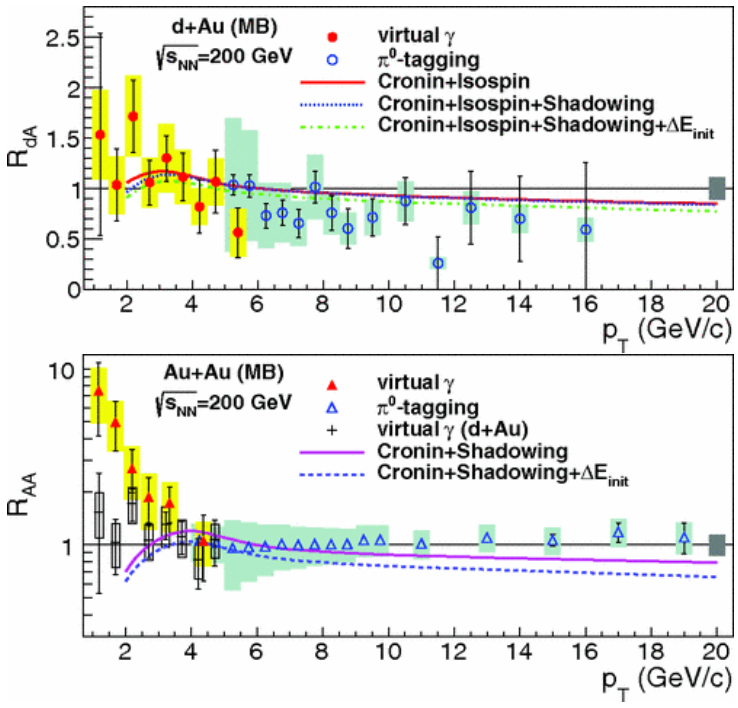

Figure 1.8: The nuclear modification factors from PHENIX d+Au and Au+Au collisions at $\sqrt{s_{NN}} = 200GeV$. Left panel shows the d+Au results compared with model calculations. Right panel is the Au+Au results compared to model prediction and d+Au results. The plots are obtained from [AAA13].

1.4.2.2 ALICE results

Another large experiment ALICE in Large Hadron Collider (LHC) gave the direct photon measurements in $p+p$ and $Pb+Pb$ collisions at $\sqrt{s_{NN}} = 2.76TeV$. With the first measurement of low p_T real photons, the inverse slope parameter of the excess p_T spectrum for $0.8 < p_T < 2.2\ GeV/c$ is extracted as: $T_{LHC} = 304 \pm 51^{syst+stat}\ MeV$. The measured invariant yield is shown in Fig. 1.9. At $p_T > 4\ GeV/c$, the measurement is consistent with the direct photon NLO calculation for $p+p$ at 2.76 TeV scaled by N_{coll}.

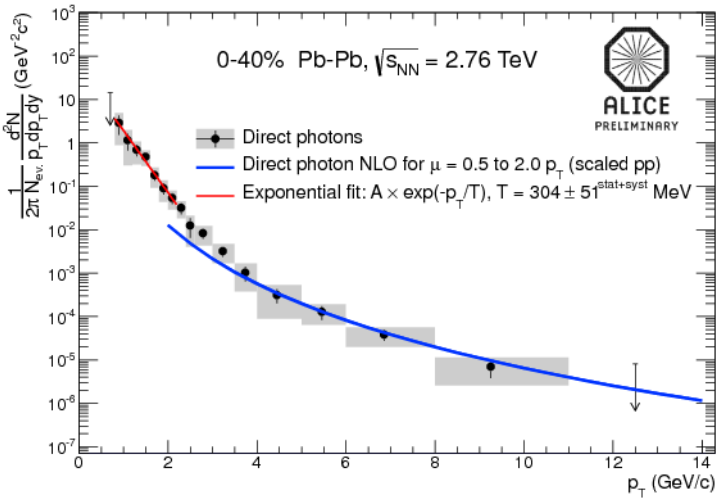

Figure 1.9: Direct photon invariant yield in $Pb+Pb$ collisions at $\sqrt{s_{NN}} = 2.76TeV$ for 0-40% centrality with NLO pQCD predictions and exponential fit in ALICE. The plots are obtained from [Wil13].

1.4.2.3 CMS results

The measurements from CMS are for $p+p$ and $Pb+Pb$ collisions at $\sqrt{s_{NN}} = 2.76TeV$. In this energy, the measurement is at several tens of GeVs. Fig. 1.10 shows the direct photon invariant yield and nuclear modification factor with this data set. As shown in the left panel, the direct photon yields in different centralities with $Pb+Pb$ data and $p+p$ data are consistent with a $p+p$ NLO prediction. The right panel shows the nuclear modification factor compared to model predictions. The curves are obtained with JETPHOX for various nuclear parton distribution functions (PDF) [Cha12].

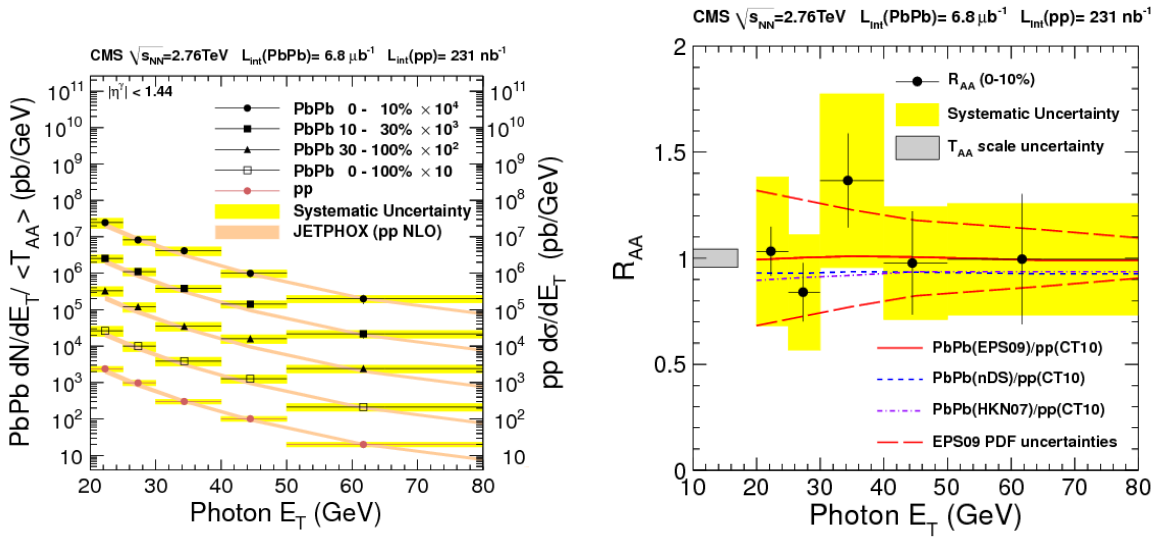

Figure 1.10: The direct photon results from CMS. Left panel: direct photon yield for $Pb + Pb$ in different centralities and for $p + p$ at 2.76 TeV. Right panel: Nuclear modification factor compared with various model predictions. The plots are obtained from [Cha12].

The CMS measured spectra are well described by NLO pQCD calculations. No modification is observed in the measured E_T region over several centralities compared to scaled $p + p$ results. This indicates N_{coll} scaling of perturbative cross sections in $Pb + Pb$ compared to $p+p$ collisions. It confirms that the nuclear parton densities are not significantly modified compared to the proton PDF in the measured kinematic range. High p_T photons are dominantly produced in parton-parton scattering [Cha12]. The direct photon is not affected by the strongly interaction medium produced in heavy ion collisions in the high p_T range.

CHAPTER 2

Experiment Set-up

2.1 Relativistic Heavy Ion Collider, RHIC

The Relativistic Heavy Ion Collider (RHIC) [HLO03] at Brookhaven National Laboratory (BNL) is one of the best mega products in the world for the research on the hot dense matter called Quark Gluon Plasma (QGP). The construction started in 1991 and finished 1999. The operation began in 2000 made it the first heavy ion collider all over the world. RHIC is also the first collider achieved polarized proton-proton collisions. This extraordinary new accelerator is designed to operate in high collision luminosity with a wide range of beam energies and particle species from heavy ion to polarized proton. The top center-of-mass collision energy is 200 GeV per nucleon pair. With these advantages, RHIC provided a excellent environment to study the fundamental properties of a hot, dense medium created in the collisions. With the polarized proton-proton collisions (center-of-mass collison energy up to 510 GeV), an insight on proton spin can be learned. The critical point in QCD phase diagram is searched by the beam energy scan program. Tab. 2.1 shows the luminosities achieved for U-U (Run-12), Au-Au (Run-11), Cu-Au (Run-12), Cu-Cu (Run-5), d-Au (Run-8), and polarized protons (Run-12, Run-13). The time in store was 59% of the total time for Au-Au (Run-11) and 54% p-p (255 GeV, Run-12).

Fig. 2.1 is a schematic view of RHIC complex including a Van de Graaff facility, a Linear Proton Accelerator, the Booster Synchrotron ring, the Alternative Gradient Synchrotron (AGS), and ultimately the RHIC synchrotron ring. In Au+Au collisions, the Au ions with charge Q = -1e from the Pulsed Sputter Ion Source pass through the Tandem

Table 2.1: Achieved luminosities for U-U (Run-12), Au-Au (Run-11), Cu-Au (Run-12), Cu-Cu (Run-5), d-Au (Run-8), and p-p (Run-12, Run-13). The beam energy is stated.

Mode	Beam energy (GeV/n)	L_{peak} $(cm^{-2}s^{-1})$	$L_{storeavg}$ $(cm^{-2}s^{-1})$	L_{week}
U-U	96.4	8.8×10^{26}	5.6×10^{26}	$0.2nb^{-1}$
Au-Au	100	50×10^{26}	30×10^{26}	$1.0nb^{-1}$
Cu-Au	100	120×10^{26}	100×10^{26}	$3.5nb^{-1}$
Cu-Cu	100	2×10^{28}	0.8×10^{28}	$2.4nb^{-1}$
d-Au	100	27×10^{28}	13.5×10^{28}	$40nb^{-1}$
p↑-p↑	100	46×10^{30}	33×10^{30}	$9.3pb^{-1}$
p↑-p↑	255	210×10^{30}	126×10^{30}	$40pb^{-1}$

Van de Graaff with a series of stripping of their electrons with a foil at the Tandem's high voltage terminal, and be accelerated to 1 MeV/nucleon. At the exit, the ions with a net charge of Q = +32e are injected into the Booster Synchrontron and accelerated to 95 MeV/nucleon. Before been injected to APS, these ions are stripped again to Q = +77e. In APS, the ions are finally accelerated to 8.86 GeV/nucleon and injected into the RHIC storage ring over the AGS-to-RHIC Transfer Line (ATR).

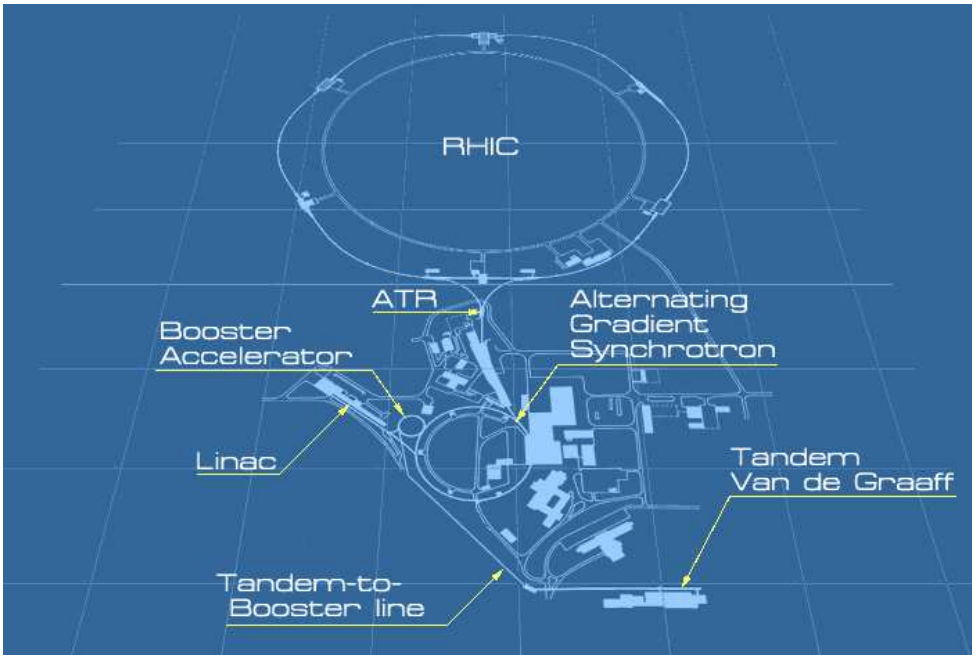

Figure 2.1: Schematic of the RHIC complex.

RHIC consists two concentric hexagonal storage rings ("Yellow" and "Blue") and six

interaction points at the middle of the six relatively straight sections where the two rings cross. The circumference of the ring is 3,834 m. Four interaction points equipped with detectors are shown in Fig. 2.1. Two large experiments, STAR and PHENIX, are located on 6 and 8 o'clock while two small ones which have been de-commissioned since 2008, PHOBOS and BRAHMS are on 10 and 2 o'clock.

2.2 The Solenoidal Tracker at RHIC, STAR

The Solenoidal Tracker at RHIC (STAR) [Ack03] located at 6 o'clock is over 1200 tons of weight and about 10 meters of height. It was constructed to explore the behavior of strongly interacted matter at high energy density and search for the signatures and information of QGP matter (a state of matter believed to exist at high energy densities). It's built with a large uniform acceptance with full azimuthal angle and large polar angle coverage around mid-rapidity. This coverage is designed to suit with the nuclear environment at RHIC which has a large number of produced particles (up to approximately one thousand per unit pseudo-rapidity) and high momentum particles from hard parton-parton scattering. With these features, STAR can measure many observables simultaneously (such as high precision tracking, momentum at mid-rapidity) to study signatures of a possible QGP phase transition and to understand the space-time evolution of the collision process in ultra-relativistic heavy ion collisions. Fig. 2.2 is a layout of STAR detector.

Fig. 2.3 is a cutaway side view of the STAR detector in Run14 including the complete sub-detectors and ongoing ones. As shown in the figure, most sub-detectors are enclosed in a solenoidal magnet [Ber03] which provides a magnetic field parallel to the beam pipe (defined as Z direction). The magnet is designed as a cylinder like one with a length of 6.85 m, a inner diameter of 5.27 m and a outer diameter of 7.32 m. Until Run14, STAR has been operated in full field ($|B_z| = 0.5$ T), reversed full field and half field configuration. To measure the helical trajectory of charged particles passing this magnetic field, the STAR tracking detector can get their momenta.

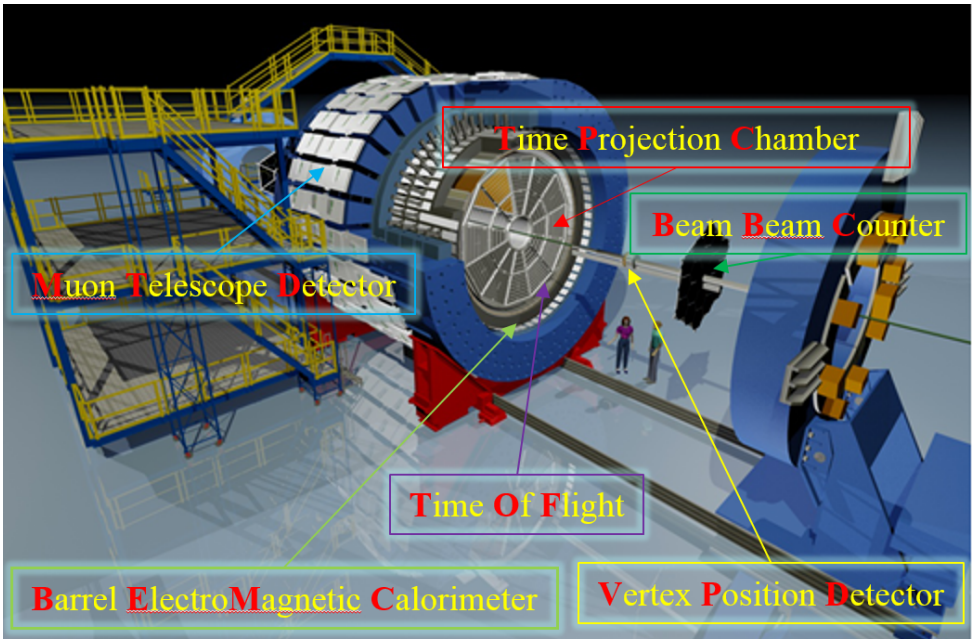

Figure 2.2: Layout of STAR detector.

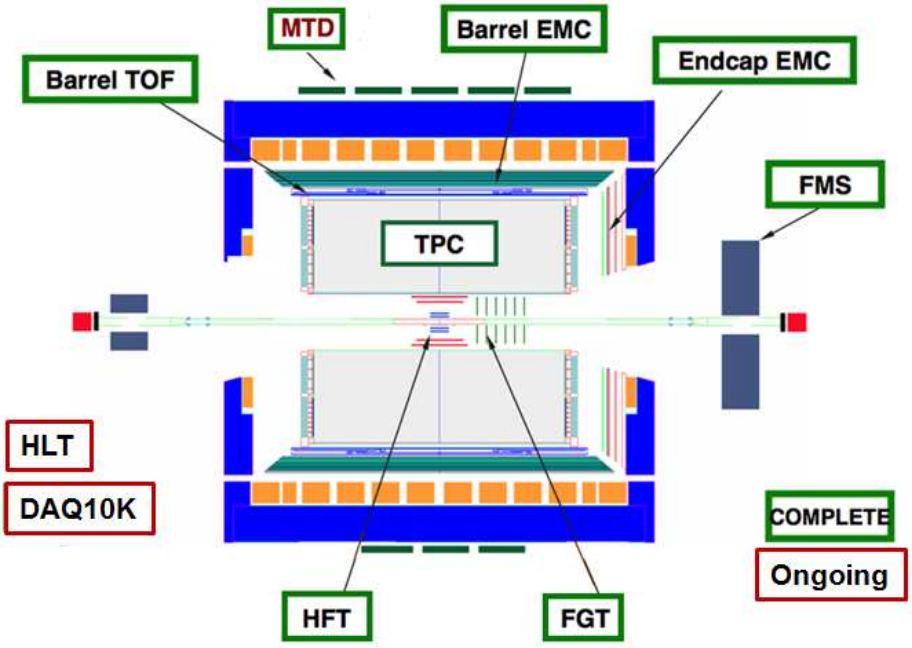

Figure 2.3: A cutaway side view of the STAR detector in Run14 including the complete and ongoing subsystems.

The STAR trigger system is a 10 MHz pipelined system based on the trigger information from fast subsystems. It provides the event selection for the slower tracking subsystems. These fast subsystems include the Zero-Degree Calorimeters (ZDC) located in the forward direction at $\theta < 2$ mrad, the Vertex Position Detector (VPD) and the Beam-Beam Counter (BBC) which consists of a hexagonal scintillator array structure at $\pm$ 3.5m from the nominal interaction point. BBC is a main device to measure the relative luminosity and provide a trigger for the polarized $p + p$ events. Some other detectors are used for special triggers: the Muon Telescope Detector (MTD) is used to trigger the events with muons and the Electro-Magnetic Calorimeter (EMC) is used to trigger on events with high transverse momentum (p_T) particles. All events recorded by STAR Data AcQuisition (DAQ) system is marked with their specific trigger types (triggerId) for the further analysis.

The STAR main tracking detector is the Time Projection Chamber (TPC) which covers the $|\eta| < 1.8$ and 2π in azimuthal. The details on TPC can be found in Sec. 2.2.2. Another Forward TPC (FTPC) is installed covering $2.5 < |\eta| < 4$ and 2π in azimuthal. To provide more valid points in tracking, a Forward GEM (Gas Electron Multiplier) Tracker (FGT) [Sim08] was installed at the forward direction as shown in Fig. 2.3.

The Time Of Flight (TOF) [Sha06a, Don06, Llo05] is installed outside TPC to give a precise measurement on time of flight with less than 100 ps timing resolution. It covered $|\eta| < 0.9$ and 2π in azimuthal. With this detector, the p_T range for π, K, p separation is extended. This will be discussed in Sec. 2.2.3. Combined with TPC, the fully installed TOF enables clean electron identification (EID) from low to intermediate transverse momentum (p_T). This is the key EID method in di-electron related analysis (Sec. 4.2).

The Electro-Magnetic Calorimeter (EMC) [Bed03, All03] used to distinguish high momentum single photons from photon pairs of π and η meson decays and electrons from charged hadrons are installed on STAR as two parts. One is the Barrel Electro-Magnetic Calorimeter located outside of TOF covers $|\eta| < 1$ with 2π coverage in azimuthal, the other is the Endcap Electro-Magnetic Calorimeter with coverage $1 < |\eta| < 2$ and 2π in

azimuth. The EMCs are also a important part of trigger system for high p_T hadron and electron trigger.

The Muon Telescope Detector (MTD) [Rua09] is fully installed in Run14. This detector which is installed outside the STAR magnet return iron bars with a similar technique as TOF will provide the capability of muon identification with low hadron contamination. The MTD is also one of the key parts of the STAR upgrade projects. Another key part is the Heavy Flavor Tracker (HFT) installed in the center of STAR just outside the beam pipe with excellent pointing resolution. The details for MTD will be discussed on Chap. 3.

2.2.1 Vertex Position Detector, VPD

The Vertex Position Detector (VPD) is used both in the STAR Level-0 trigger and offline to measure the location of the collision primary vertex at Z (along the beam pipe) position and the "start time" of the event which is needed by other fast-timing detectors in STAR such as TOF and MTD.

There are two identical detector assemblies in VPD, one on the east and one on the west of STAR. The two assemblies are installed symmetrically with respecto to the center of STAR at a distance of 5.7 m, surrounding the beam pipe. Each assembly has 19 PMT based detectors combined as shown in Fig.2.4 [LZN14].

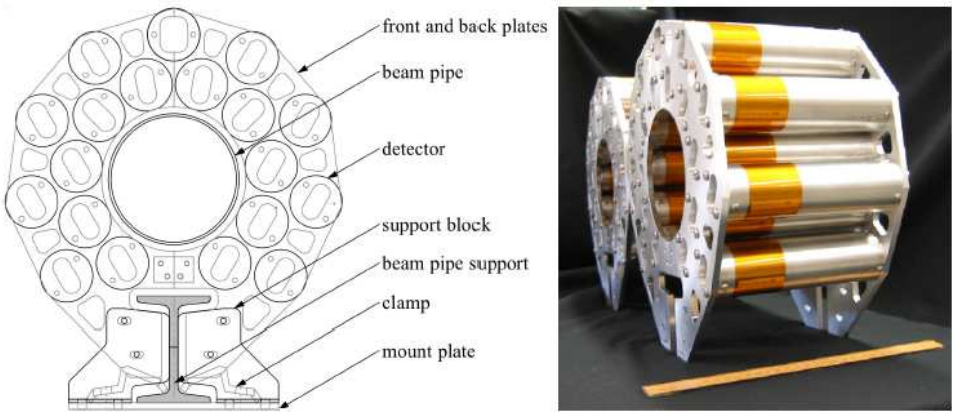

Figure 2.4: On the left is a schematic front view of a VPD assembly, and on the right is a photograph of the two VPD assemblies. A one foot long ruler is shown for scale on the right.

All channels of VPD need to be calibrated to get their offsets once there is a new energy beam injection. These offsets are obtained as the average values of the times in specific lit channels with respect to reference channels (fastest channels in east and west). Fig. 2.5 shows a time difference between east 7 and east 16 (reference channel) at the setting period of Run14 Au+Au 15 GeV collisions. The Gaussian-fit mean value is the generated offset for this specific channel (east 7) which has been implemented online. After this offset correction, a certain distance cut on Z direction of VPD measured vertex is set for specific triggers. To reject pile up events, a correlation between VPD measured vertex and TPC tracking vertex is required in the analysis.

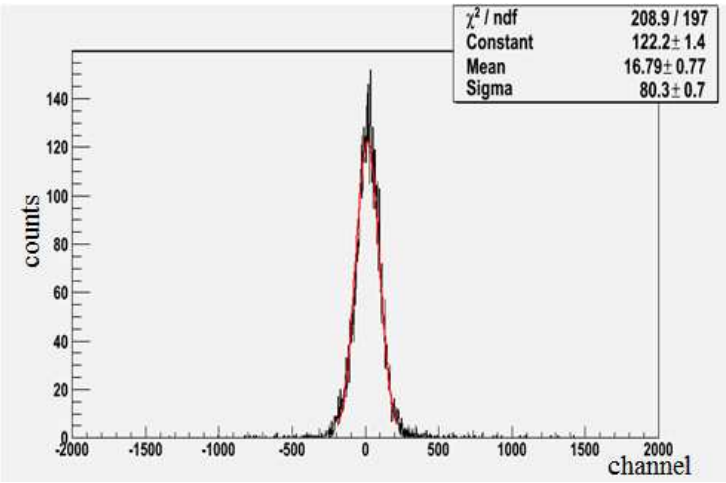

Figure 2.5: Distribution of VPD TAC difference (east 7 - east 16) on MXQ crate. The Gaussian fit mean is the offset of east 7.

To use TPC tracking vertex as a reference, a relative resolution of VPD trigger system can be generated. Fig. 2.6 shows the correlation between VPD measured vertex (from trigger system) and TPC measured vertex. The method for TPC vertex finding can be found in Sec. 2.2.2. A liner function is used to fit the correlation while the slope closed to unity stands for a good correlation. Left panel of Fig. 2.7 is the distribution of the difference of VPD and TPC vertex Z position in a specific reference multiplicity (Sec. 4.1) range. The right panel is a overall distribution of the Gaussian-fit σ as a function of reference multiplicity. The average resolution of the VPD vertex resolution from trigger system is about 20 cm. These figures are from Run9 $p+p$ 200 GeV data.

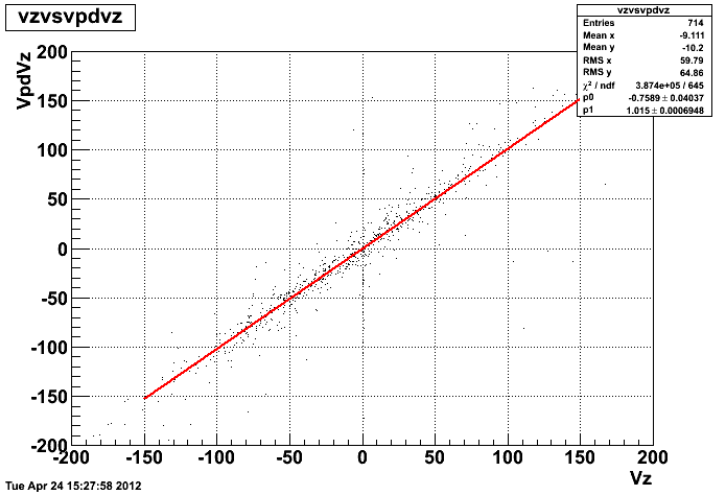

Figure 2.6: Correlation between VPD and TPC measured Vz. VPD Vz is from the trigger system.

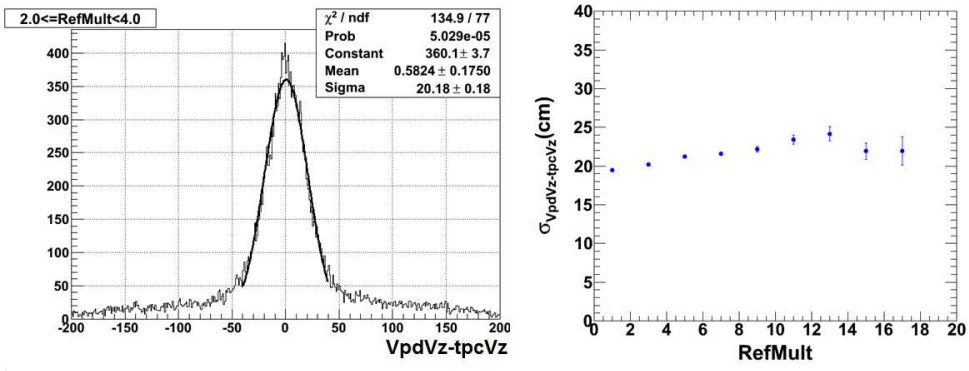

Figure 2.7: Left panel: VPD Vz - TPC Vz in a specific refmult range. Right panel: VPD trigger system relative resolution vs. reference multiplicity.

2.2.2 Time Projection Chamber, TPC

The Time Projection Chamber (TPC) [And03] is a key part which located just outside the beam pipe. As the heart of STAR detector, it is used as a primary tracking device. The tracking information is obtained by the measurement on track, momenta, and ionization energy loss (dE/dx) which is used to identify the particles.

A schematic view of TPC is shown in Fig. 2.8. It is a cylindrical like detector with a length of 4.2 m and a diameter of 4 m which surrounds a beam - beam interaction region and sits in a large solenoidal magnet that operates at 0.5 T at RHIC. The collisions take place near the center of the TPC. The TPC is developed from Multi-Wire Proportional Chamber (MWPC) and Drift Chamber (DC). The charged particles traverse the mixture gas P10 (90% argon, 10% methane) filled in TPC and the ionizing particles are generated due to the ionization energy loss of the charged particles. The fast drift velocity which peaks at a low electric field is the primary attribute of this gas. The drift velocity of P10 gas is 5.45 cm/μs. The transverse diffusion in this gas is about $\sigma_T = 3.3$ mm after drifting 210 cm while longitudinal diffusion is $\sigma_L = 5.2$ mm. These basic parameters are all listed in Tab. 2.2. The detector operating on the peak of the velocity curve will make the drift velocity stable and insensitive to small variations in temperature and pressure. A well-defined, uniform, electric field (135V/cm) is used for the drifting of these ionizing particles.

The readout system is the MWPC with pads on the endcap where these secondary particles can be amplified 1000 - 3000 times by the avalanching in MWPC. The positive ions created in the avalanche induce a temporary projection on the pads which disappears as the ions move away from the anode wire. This projection signal will share several adjacent pads, so the position can be reconstructed to a small fraction of the pad width. The pad will give x-y coordinate position for tracking while the large number of pads (136,608) makes the measurement precise. The Z position will be given by 512 time buckets and the drift velocity. The paths of the charged particles passing the TPC are reconstructed by these precise measurements on x-y-z coordinate.

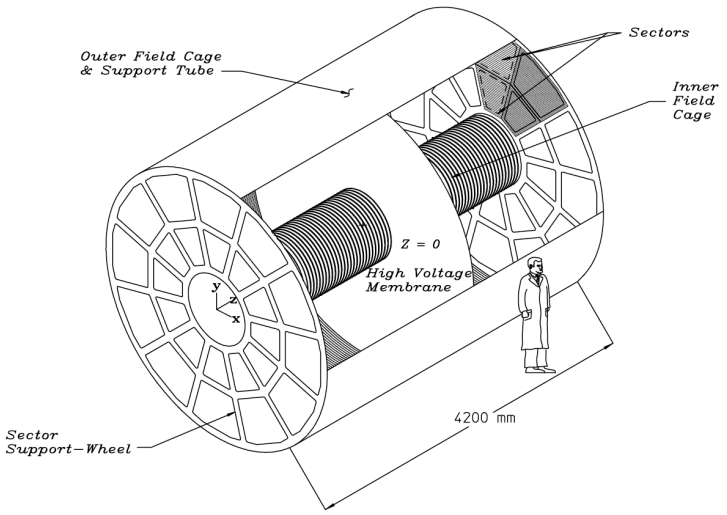

Figure 2.8: The STAR TPC surrounds a beam-beam interaction region at RHIC.

Table 2.2: Basic parameters for the STAR TPC [And03]

Item	Dimension	Comment
Length of the TPC	420 cm	210 cm per half
Outer diameter of the drift volume	400 cm	200 cm radius
Inner diameter of the drift volume	100 cm	50 cm radius
Distance: cathode to ground plane	209.3 cm	Each side
Cathode	400 cm diameter	At the center of the TPC
Cathode potential	28 kV	Typical
Drift gas	P10	90% argon, 10% methane
Pressure	Atmospheric + 2 mbar	
Drift velocity	5.45 cm/μs	Typical
Transverse diffusion σ	230 μ m/$\sqrt{cm}$	140 V/cm & 0.5 T
Longitudinal diffusion σ	360 μ m/$\sqrt{cm}$	140 V/cm
Number of anode sectors	24	12 per end
Number of pads	136 608	
Signal to noise rate	20:1	
Electronics shaping time	180 ns	FWHM
Signal dynamic range	10 bits	
Sampling rate	9.4 MHz	
Sampling depth	512 time buckets	380 time buckets typical
Magnetic field	0, $\pm$0.25 T, $\pm$0.5 T	Solenoidal

The chamber consists of a pad plane and three wire planes. Fig. 2.9 shows the design and parameters of the TPC anode pad plane with one full sector. There are 12 sectors on one side, 24 in total. The outer subsector have continuous pad coverage to get a better dE/dx resolution because the full signal is collected and the statics is improved. For the inner subsector, the track density in this region is very high. To optimized a good resolution for two-hit, the inner sector uses smaller pads and the space between the pad plane and anode is reduced. It also enhances the detection capacity on the particles with lower momentum. The difference between inner and outer subsector can be found in Tab. 2.3.

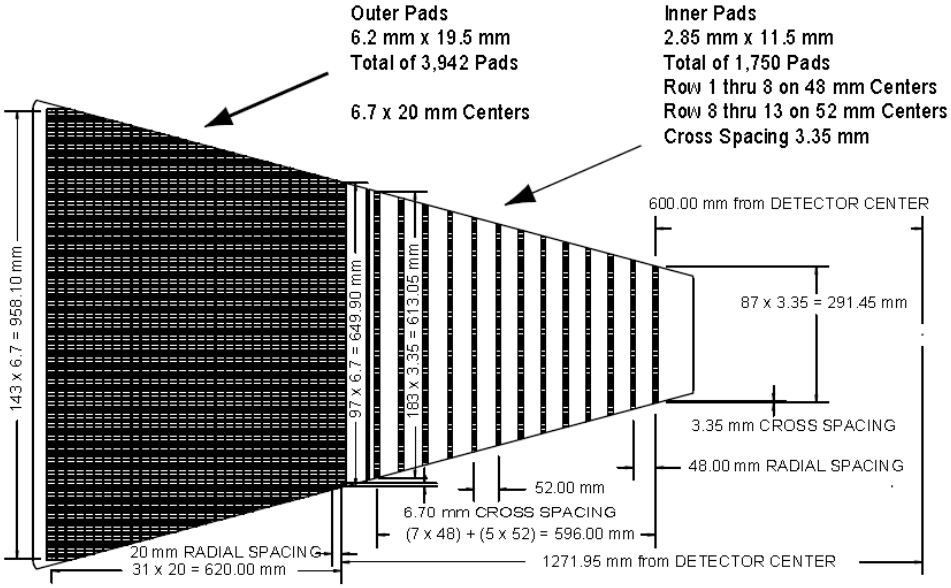

Figure 2.9: The anode pad plane of one full TPC sector. The inner subsector is on the right and it has small pads arranged in widely spaced rows. The outer subsector is on the left and it is densely packed with larger pads [And03].

As mentioned before, with the measurement on x-y-z coordinate position based on the readout pads and drift time, the positions of the ionization clusters along the track can be found separately. The resolution is depend on the angle between the charged particle momentum and the drift direction and the drift length. A longer drift length and bigger angle will give a better resolution. The level of the position resolution is on the level of mm. For the track reconstruction, a helix with considering the energy loss in the gas is fitted to these clusters. The fitted helix can also be extrapolated to other detectors

Table 2.3: Comparison on inner and outer TPC subsector.

Item	Inner subsector	Outer subsector
Pad size	2.85 mm × 11.5 mm	6.20 mm × 19.5 mm
Isolation gap between pads	0.5 mm	0.5 mm
Pad rows	13 (#1-#13)	32 (#14-#45)
Number of pads	1750	3942
Anode wire to pad plane spacing	2 mm	4 mm
Anode voltage	1170 V	1390 V
Anode gas gain	3770	1230

(such as TOF) to find whether there is a nearby hit measured by these detectors. If so, these additional points may be added to the track. Combined with these points, a more complicated fitting method is used to fit all the points. The final conformed track is called global track. By using all the global tracks in a same event, the primary vertex can be found with high accuracy. The resolution of vertex inversely proportional to the statistical error of the number of track. In central Au+Au collisions, with amount of track, the resolution can reach 350 μm. With a distance of closest approach (DCA) which stands for the distance of the track to the primary vertex less than 3 cm, a global track can be refitted by adding the primary vertex. If the refitting is well, this refit track is marked as a primary track and stored in another class for further analysis.

The TPC identifies different particle species by using their energy loss in its volume. This energy loss value can be calculated by the deposit charge collected on up to 45 pad rows. The dE/dx distribution plotted using a 70% truncated mean is shown in Fig. 2.10. Seen from this figure, with less than 8% resolution, the π/K separation is up to p $\sim$ 0.7 GeV/c and proton to (π, K) separation is up to p $\sim$ 1.1 GeV/c. Althrough the TPC is not originally designed to identify particles at high momentum, the particles with high momentum (p $\geq$ 3 GeV/c) [Sha06b, Xu08] can also be identified by the separation of their dE/dx at relativistic rising region. The e/π (e/K) separation is about 3σ (5σ) at p_T = 3 GeV/c and 2σ (3.5σ) at p_T = 10 GeV/c [Xu08].

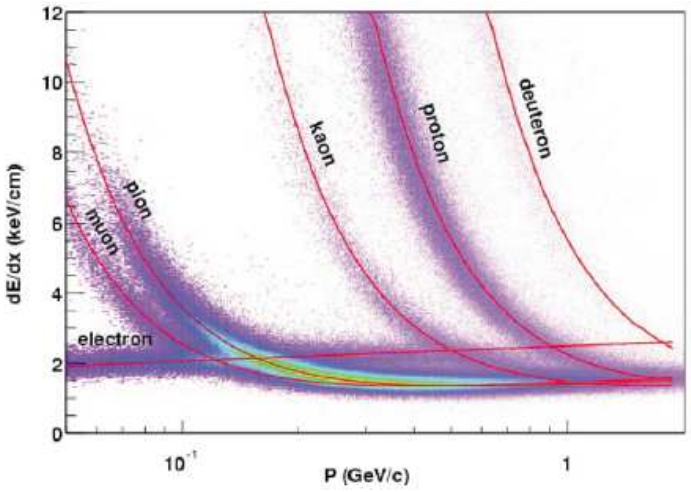

Figure 2.10: The energy loss distribution for primary and secondary particles in the STAR TPC as a function of the p_T of the primary particle. The magnetic field was 0.25 T [And03].

2.2.3 Time Of Flight Detector, TOF

The barrel Time-Of-Flight (TOF) is based on the Multi-gap Resistive Plate Chamber (MRPC) [CCH96] technique with the advantages of low cost, high efficiency and good intrinsic timing resolution. With 120 TOF trays installed outside the barrel TPC (60 trays on $\eta < 0$, 60 trays on $\eta > 0$), STAR had finished the TOF upgrade in 2010. In Run14, until now, 115 out of 120 trays works well in data taking. With the cost-effective MRPC modules, the barrel TOF covers $|\eta| < 0.9$ and 2π azimuthal angle.

Each TOF tray consists of 8 MRPC modules. Fig. 2.11 is the side view of a MRPC module at STAR. The upper and lower views are not at the same scale. The MRPC is basically a stack of resistive plates (0.54 mm thick float glass) with a series of uniform 220 μm gas gaps in between. The resistive plates is utilized to quench the streamers which initiate a spark breakdown. Graphite electrodes are sprayed to cover the outer surface of (wider) outer glass plates. A strong electric field is generated in each gap by applying high voltage (7000 V working voltage) across these electrodes. A charged particle passing the glass stack generates primary ionization along its path inside the gaps, and the strong electric field there produces Townsend amplification avalanches. Because both the electrodes and the glass plates are resistive, they are transparent to this avalanche

charge. Thus, the induced signal on the copper readout pads (outside the electrodes) is the sum of the avalanches in all of the gas gaps.

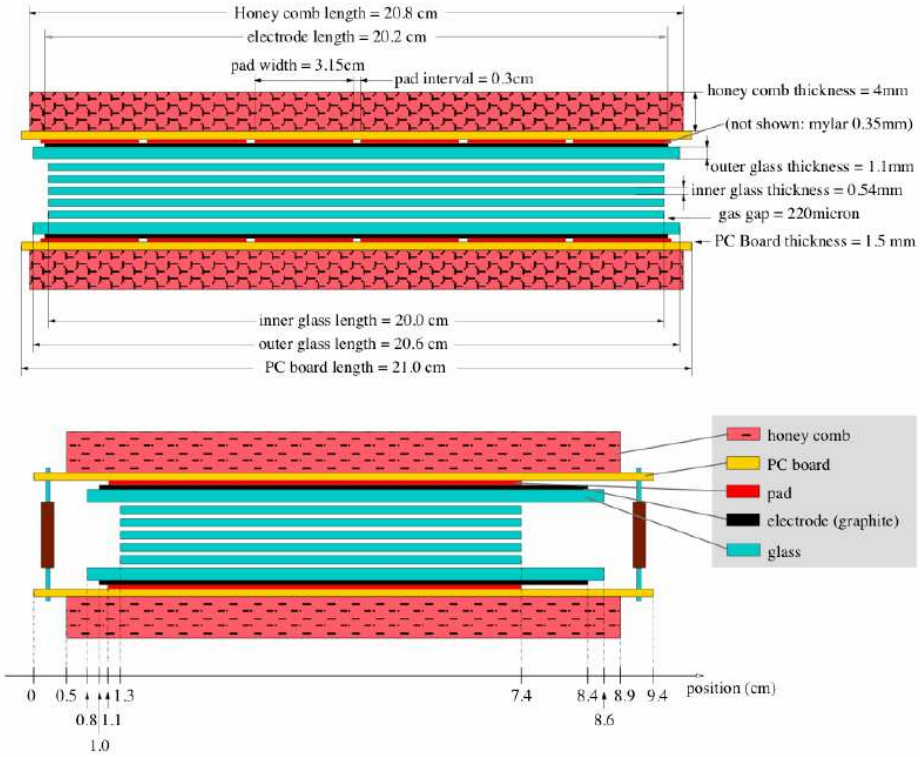

Figure 2.11: Side views of MRPC. The upper(lower) is for long(short) side.

The typical size of the module is $94mm \times 212mm \times 12mm$, its active area is $61mm \times 200mm$. There are 6 readout pads per modules, 61 mm $\times$ 31.5 mm area per pad with 3 mm gap in between. As shown in Fig. 2.12, the readout pads span azimuthal direction. The whole TOF tray covers 6° (360/60) in ϕ direction. With the "start time" measured by VPD, TOF can give the time of flight measurement by measuring the "stop time".

After 2005, the intrinsic timing resolution of TOF with calibration is about 75 ps. Fig. 2.13 is the distribution of inversed velocity ($1/\beta$) as a function of momentum. The distribution bends of π, K, p are clearly showed on the plots. With requiring $1/\beta$ closed to 1 which means the velocity is close to the velocity of light, the electron can be identified with TPC dE/dx distribution. This can be clearly seen in Fig. 2.14 which the distributions of TPC dE/dx before and after TOF velocity cut. This EID method will be discussed in Chap. 4.2.

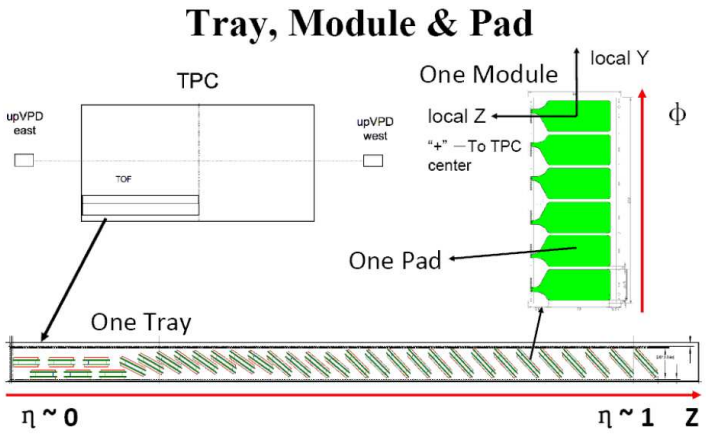

Figure 2.12: TOF geometry for trays, modules and readout pads.

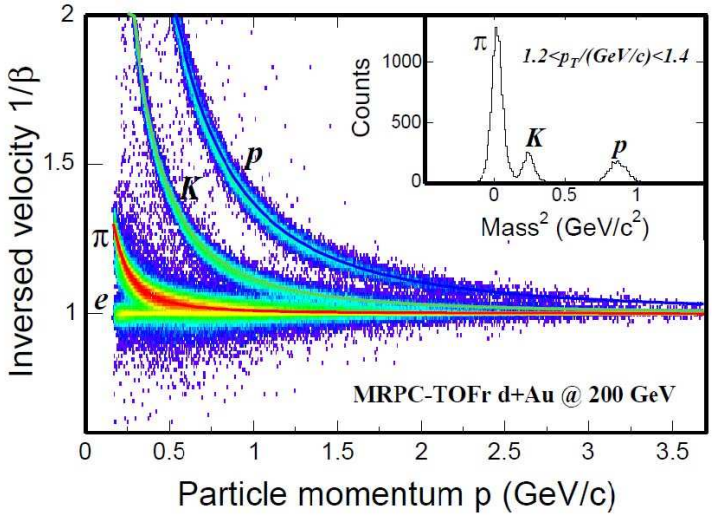

Figure 2.13: Inversed velocity vs momentum from TOFr+pVPD triggered events from $d + Au$ collisions [col].

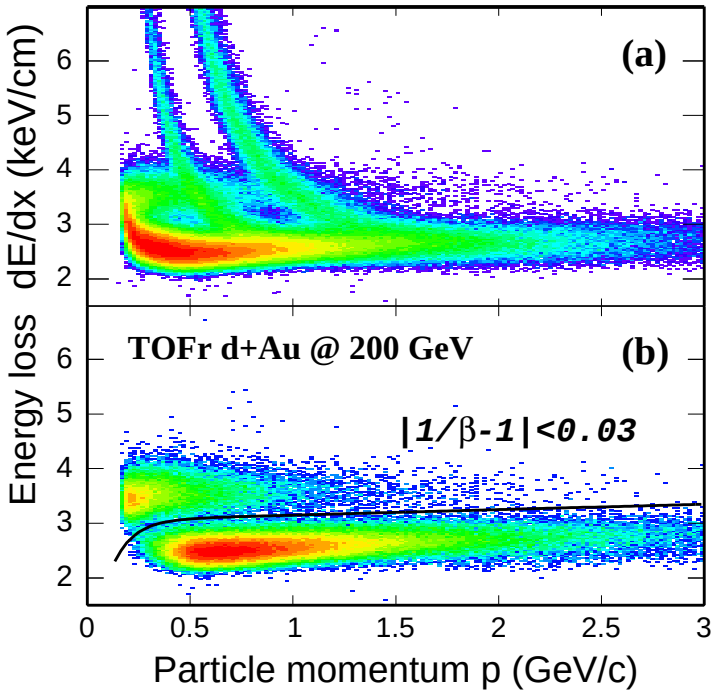

Figure 2.14: The TPC dE/dx distribution as a function of momentum. Panel (a): w/o $1/\beta$ cut. Panel (b): w/ $|1/\beta - 1| < 0.03$ [col].

2.2.4 Barrel Electro-Magnetic Calorimeter, BEMC

The STAR BEMC [Bed03] is a sub-detector which has the ability to trigger on and measure high p_T processes such as jets, leading hadrons, heavy quarks with its high speed. It provides large acceptance for the particle (such photons, electrons) detection. In this analysis, the BEMC triggered events are used for the high p_T di-electron measurements.

The BEMC is located between TOF and the STAR aluminum coil of the STAR solenoid and covers $|\eta| \leq 1$ and 2π in azimuthal. The front face of the calorimeter is at a radius of 220 cm from and parallel to Z axis. There are 120 calorimeter modules with the coverage 6° each in ϕ direction and 1 in η. These modules are mounted 60 in ϕ by 2 in η. Each module is roughly 26 cm wide by 293 cm long with an active depth of 23.5 cm plus about 6.6 cm in structural plates (of which ∼1.9 cm lies in front of the detector).

The modules are divided into 40 towers, 2 in ϕ and 20 in η. The full Barrel Calorimeter is divided into 4800 towers. Fig. 2.15 left panel shows a schematic side view of a module

in η direction while the right panel is the side view of a module showing the mechanical assembly including the compression components and the rail mounting system.

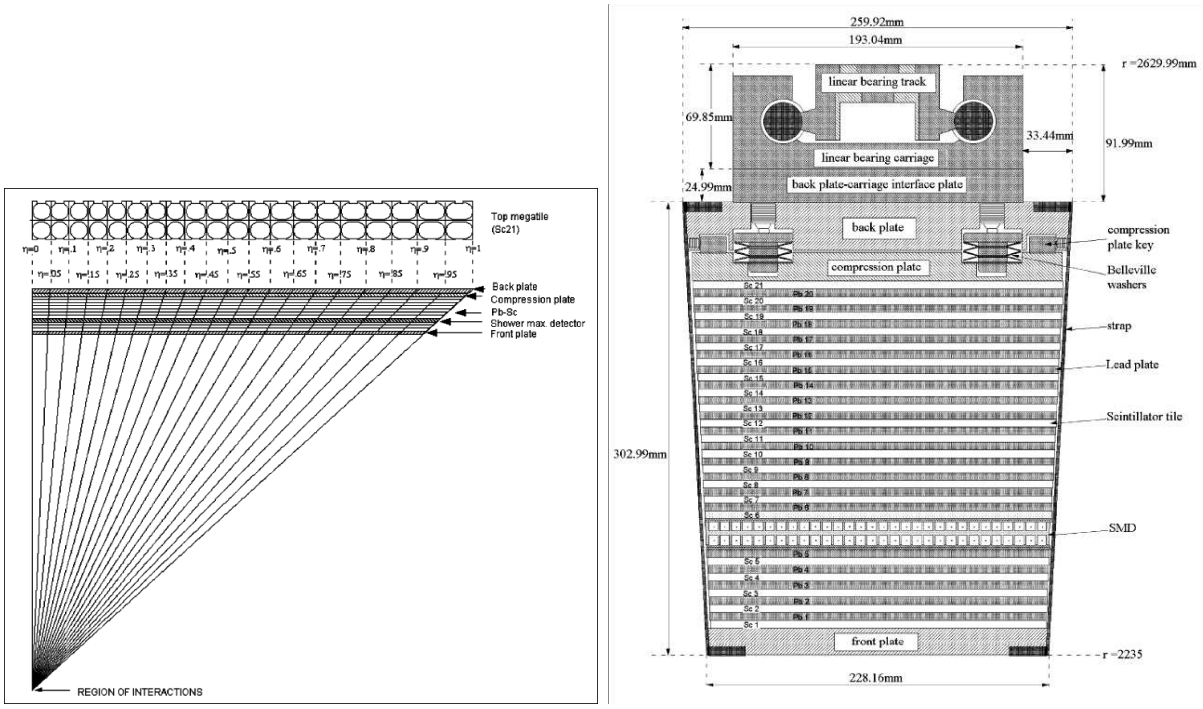

Figure 2.15: The schematic view of BEMC module. Left panel: schematic side view of a module in η direction. Right panel: side view of a module showing the mechanical assembly including the compression components and the rail mounting system. The plots are obtained from [Bed03].

CHAPTER 3

Muon Telescope Detector

3.1 Physics Motivation

A large area muon telescope detector (MTD) [Rua09] at mid-rapidity will provide excellent muon identification and trigger capabilities at mid-rapidity in the high-luminosity era at RHIC. This novel and compact detector can provide crucial measurements for many exciting physics perspectives. We can measure and separate different Upsilon states and measure J/ψ over a broad transverse momentum range through di-muon decays to study color screening features. The pure μ sample will reject the "tail" of different Upsilon states mass distribution to make the separation. The measurement of e-muon correlations can distinguish heavy flavor contributions from initial lepton pair production (Sec. 1.3). These physics perspectives make MTD as a key part of STAR upgrade project.

3.2 Multi-gap Resistive Plate Chamber

The MTD is based on the same detector and electronics technologies as the recently installed TOF system [col] in STAR – Mult-gap resistive plate chamber (MRPC). This MRPC module works in the avalanche mode with mixture gas 95% freon + 5% isobutane. The MRPC used for MTD is with long strips (87 cm) because of the low occupancy out of the STAR magnet. The R&D results of a prototype MRPC module gave 95% efficiency, 60-70 ps timing resolution and $\sim$ 1 cm spatial resolution [Rua09].

With these good performances, combined with the information from track matching with the MTD, ionization energy loss measured by TPC and time-of-flight measured by

TOF, the muon identification with a few GeV will be obtained. Fig. 3.1 is the end view of a LMRPC module for the full MTD.

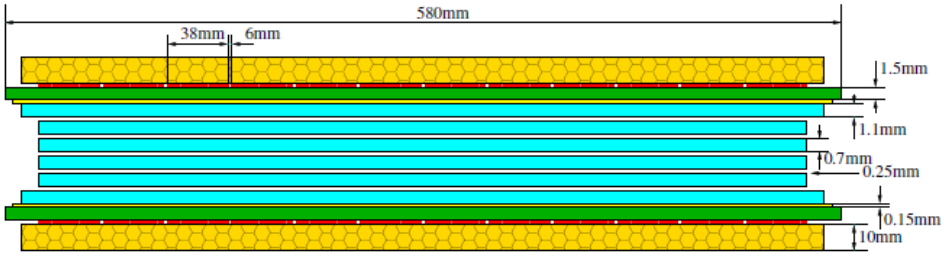

Figure 3.1: End view of a LMRP module for the full MTD.

3.3 MTD in STAR

MTD covers 45% in azimuth and $|\eta| < 0.5$ in pseudo-rapidity behind the return iron bars for the STAR magnet. As showed in Fig. 3.2, the MTD trays lie on the BEMC PMT boxes, 5 trays per backleg in the same ϕ direction and different η position. The full MTD system contains 30 backlegs. Every backleg covered 8° in ϕ direction while the gap between two backlegs is 4°.

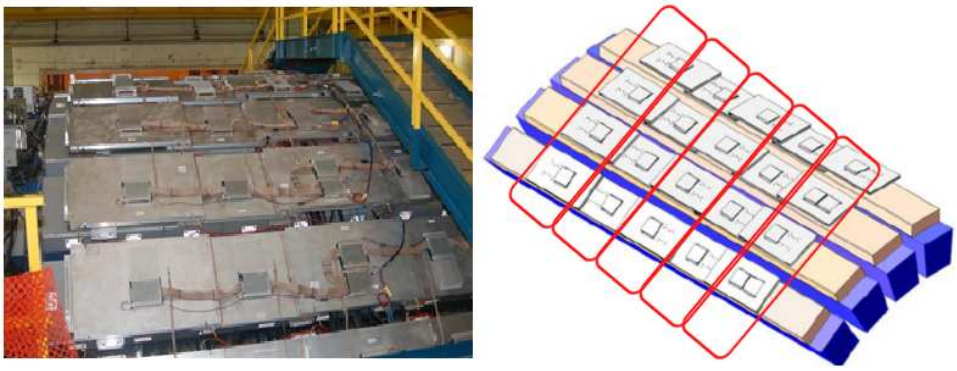

Figure 3.2: Left: View from south platform on 3rd floor. Right: Schematic view of MTD backleg. The red frame stands for the combination of the trigger signals for every 5 trays in the same η position.

3.3.1 MTD installation and testing

The construction of the MTD at STAR is finished. In 2012, about 10% of the full system has been installed in STAR while in 2013 this number is 63%. In the year 2014, the whole system has been installed which superseded the milestone (83% in 2014). On April 5th 2014, the last backleg was successfully populated by the MTD trays. 122 trays which include 1464 readout strips and 2928 readout channels in total have been installed on STAR. One tray was excluded due to the gas leaking and 25 readout strips above magnet gap were masked out to reject background. At last, 121 out of 122 trays include 1427 readout strips and 2854 readout channels were used for data taking in Run14.

Fig. 3.3 shows the schematic full MTD system. The installation work lasted several months per run. The Run13 installation took about 5 months while the time in Run14 is 4 months. The MTD system was installed backleg by backleg. Before the trays were lifted to STAR detector, the pre-installation testing need to be done first. Because of the cradle which STAR was supported by, only 3 trays can be installed as one backleg in the lower half hemisphere of STAR. All 5 (or 3) trays were assembled in the test area and tested by sending some commands to the MTD electronics. By checking the response from MTD electronics, the issues can be found if exists. After passing the pre-installation testing, the MTD trays were lifted and installed on the mechanical structures on the EMC PMT boxes. After all cable dressing (Fig. 3.4) was done, a post-installation test was necessary for double check. Until now, based on the latest data taken from Run14, all valid MTD modules worked well.

3.3.2 MTD trigger system

The primary physics goal requires triggering on di-muon events sampling full luminosity. In this case, no physics information will be dropped caused by the bias of trigger. Because the bandwidth of MTD for DAQ is limited, some additional cuts are required. To select muons and reject hadronic showers that punch through the magnet steel, a timing cut will be applied to select for good MTD signals.

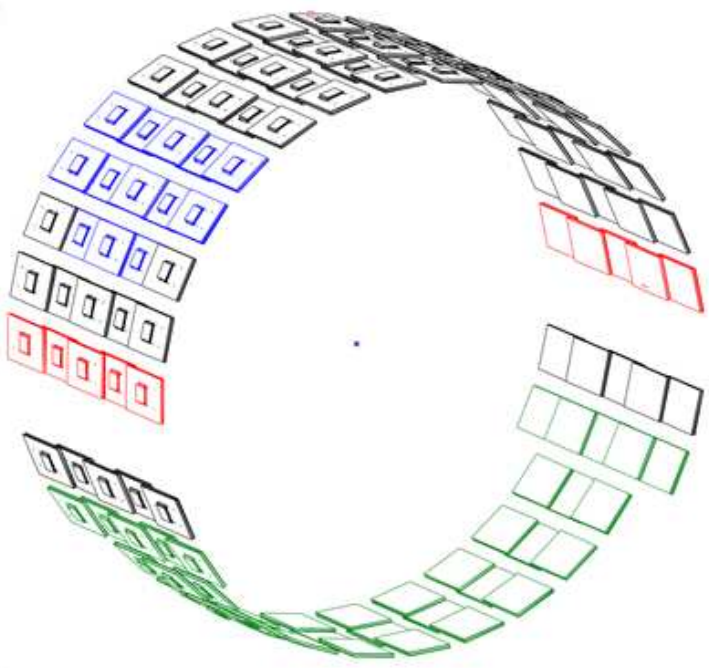

Figure 3.3: Schematic full MTD system. Blue: installed in Run12. Black: installed in Run13. Green: installed in Run14. Red: backleg 8 and 24 with few readout strips disabled.

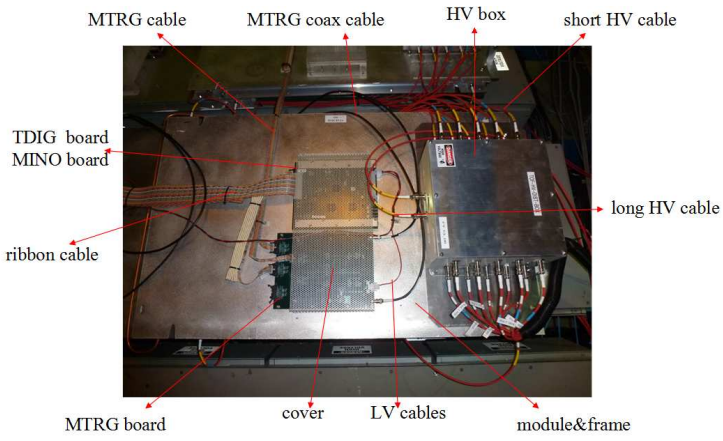

Figure 3.4: Cable dressing on a MTD tray.

Fig. 3.5 shows a timing window cut for the MTD measured signal in Run12 $p+p$ 500GeV collisions. The enhanced area is where the good events located. Since the MTD is readout from both ends and the strips are 87 cm long, the average time from both ends will be calculated and transfered to higher trigger level for the comparison to the collision time.

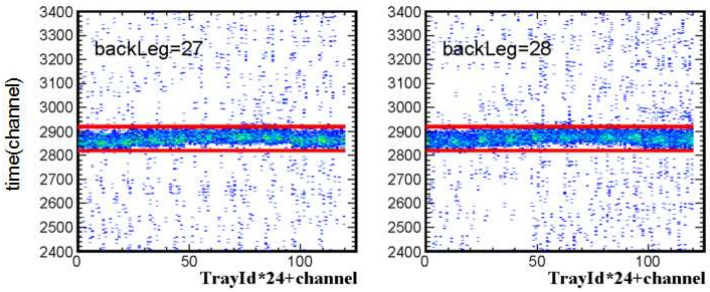

Figure 3.5: Time window cut for MTD measured signal in Run12 $p+p$ 500GeV collisions. The area between two red lines is selected.

Fig. 3.6 is a schematic for MTD readout. The signals collected from MRPC modules are sent to MINO board and then divided into two paths. One is via TDIG board to the DAQ system and the other is via MTRG board to online trigger system which can used for MTD related trigger. The occupancy in the MTD is very low. As Fig. 3.2 shows, only one east and one west signal are sent to trigger system from the 60 strips of 5 MTD trays in the same η region at 5 nearby backlegs. This allows for a correction on the arrival time in the high η region at trigger level. The correction could be larger than 1 ns in the highest η region.

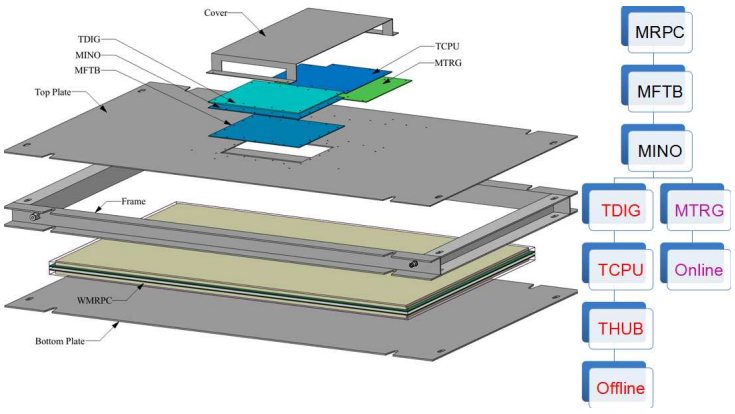

Figure 3.6: Left: Schematic of MTD tray. Right: Readout steps.

Been used as an important detector for trigger, the MTD has its own trigger algorithm to select good hits and passes them to higher trigger levels. Fig. 3.7 is a schematic view of MTD trigger system in Run13. There are several trigger levels from lower to higher level which called MT001 (MT002, MT003), MT101, TF201 and TCU. MTRG cables brought the signals to different QT boards on MT001 (MT002, MT003) in pairs where the signals were amplified and measured by ADC and TAC. The algorithm requires good ADC and TAC values from both ends and also cuts on the pair TAC sum from east and west. For trigger system, the common stop is used on TAC. The maximum of the TAC sums which stood for earliest time from MT001, MT002 and MT003 were sent to MT101 while the multiplicity was calculated. At the same time, the earliest timing information from VPD was sent to MT101. One or more good MTD TAC sum in MT101 will be directly sent to the highest level TCU bits by marking MTD cosmic bit as 1. At the same time, the maximum of these MTD TAC sums was calculated by subtracting the VPD time.

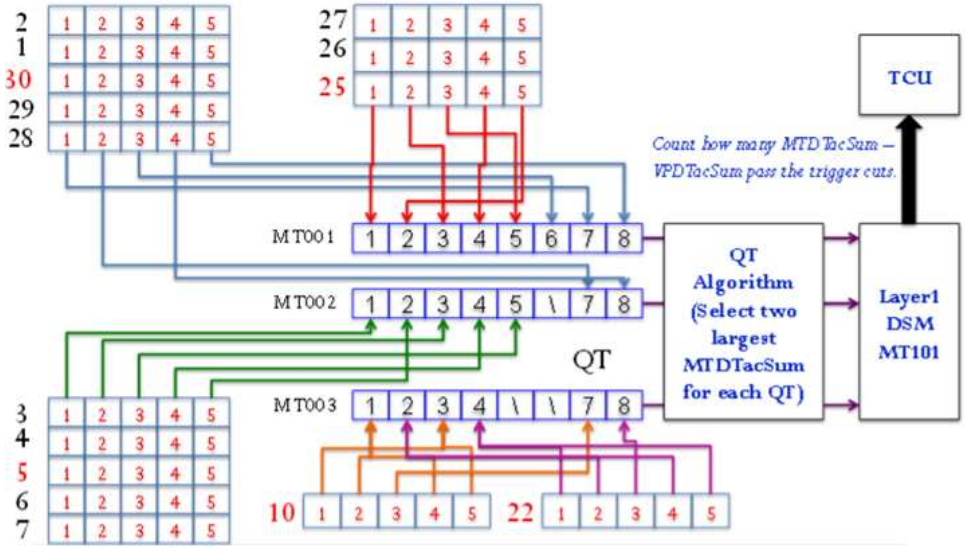

Figure 3.7: MTD trigger system in Run13.

Fig. 3.8 is the distribution of MTD maximum TAC sum - VPD TAC sum + 8192. This difference was calculated in TF201 and will be finally sent to TCU bits as a good MTD-VPD coincidence bit. All the passing work to higher level will be chosen by specific cuts. After passing all the algorithm, the TCU bits contained all the information which was needed for MTD related triggers. MTD cosmic bit – at least one good MTD hit.

MTD double hits bit – at least two good MTD hits. MTD-VPD bit – good MTD&VPD coincidence.

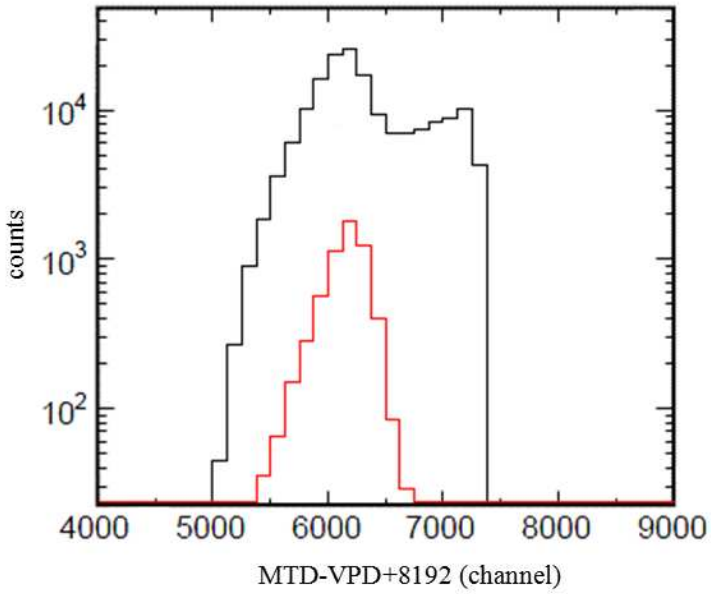

Figure 3.8: MTD&VPD TAC difference for MTD&VPD trigger (Run12 $p+p$ collisions at $\sqrt{s} = 500GeV$). Black line is the distribution for MTD&VPD triggered events. Red line is the distribution for MTD&VPD trigger events with matched tracks.

In Run12, the cut range for MTD&VPD minimum bias trigger was 5000 $\sim$ 7300. Seen from Fig. 3.8, all real events which had matched tracks were in the cut range. The cuts selected the signals we needed while reducing the trigger rate as we required. The matched track was defined as a good track in TPC which can be projected to MTD active area and had a associated MTD good hit. The track projection steps can be found in Fig. 3.9 and Tab. 3.1. It was based on the different magnetic fields and energy losses in different areas. In EMC and steel, the energy losses were taken into account step by step by dividing the track into several parts when projection. As MTD&VPD minimum bias trigger required none zero MTD-VPD bit, di-muon trigger required a none zero MTD double hits bit in TCU bits and MTD cosmic-ray trigger required a good MTD cosmic bit. To trigger on e-μ events, a coincidence between good MTD hit bit and good BHT (from EMC) hit bit was required on TCU bits.

All these triggers were implemented and worked well. Whether the events triggered by

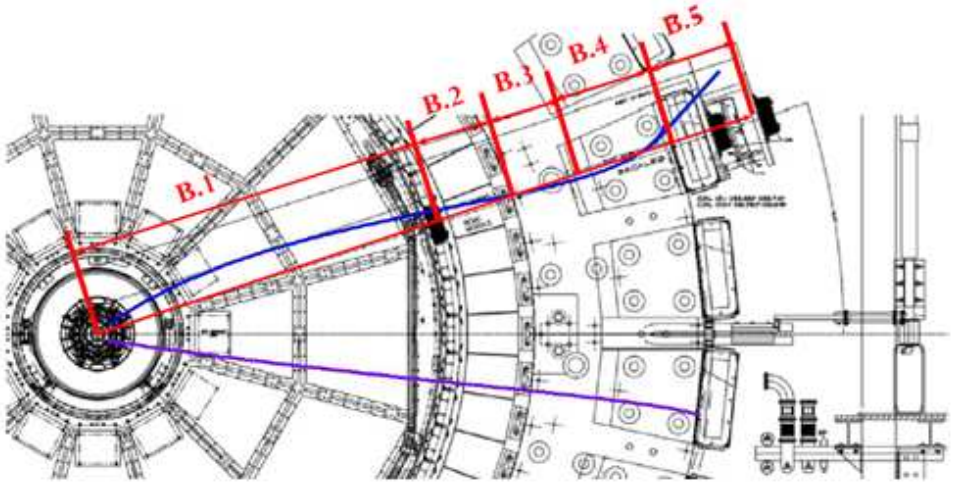

Figure 3.9: Schematic of track projection steps.

Table 3.1: Track projection steps.

	B.1(TOF)	B.2(EMC)	B.3(Inner steel)	B.4(steel)	B.5(MTD)
Radius(cm)	211	225-247	303	303-364	403
Bfield(T)	0.5	0.5	0.5	-1.26	0
Enengy loss(GeV/cm)	0	0.0075	0	0.012	0

these triggers contained the real tracks as required depended on whether these tracks can pass the track matching algorithm and other particle identification cuts. But the related trigger can definitely enhance the possibility. Fig. 3.10 is the event display with good matched tracks in Run12 and Run13. These events were triggered by di-muon trigger. Left plot is for Run12 Cu + Au collisions while right one is for Run13 $p + p$ collisions.

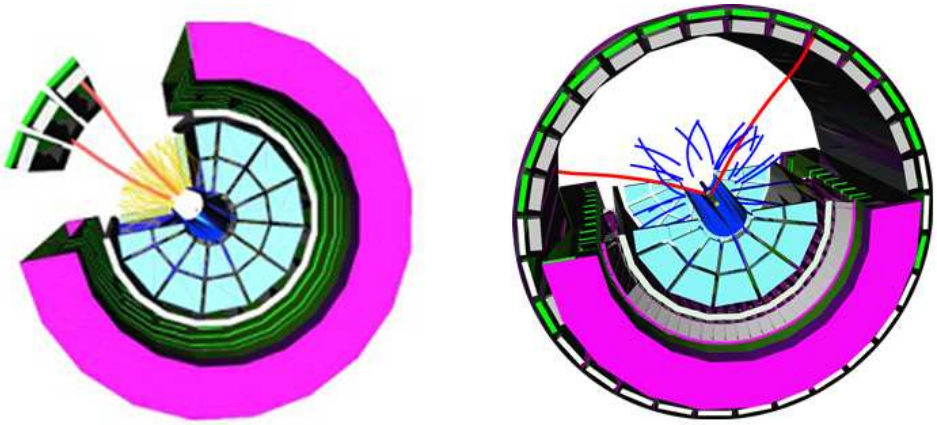

Figure 3.10: Event display for MTD triggered events. Left is the Run12 Cu+Au di-muon event and right is the Run13 $p + p$ di-muon triggered event.

3.3.3 MTD performance in Run12

In Run12, 13 trays were installed on STAR. Data from different triggers were taken smoothly. The preliminary study on MTD efficiency was done based on Run12 cosmic-ray data because the noise and background in cosmic-ray data was low. The mean p_T for cosmic-ray is 5 to 6 GeV/c. The multiple scattering effect is lower which will make the projection more precise. As showed in Fig. 3.11, with a lower threshold on MINO board, the efficiency is about 90% in average. The drop in low p_T is caused by the higher multiple scattering effect, because there was no multiple scattering effect involved in the projection work. With higher multiple scattering, the difference between MTD measured hit position (cosmic-ray real hit position) and the projected MTD hit position from TPC track becomes larger. In this efficiency calculation, the denominator is the number of tracks with geometry matching which means these tracks can be projected to MTD active area. The numerator is the number of these tracks which also have a MTD

matched hit. In this case, the stronger multiple scattering effect will make the efficiency lower. By detailed study, the value that the efficiency in low p_T drops is consistent with the multiple scattering effect in that p_T range.

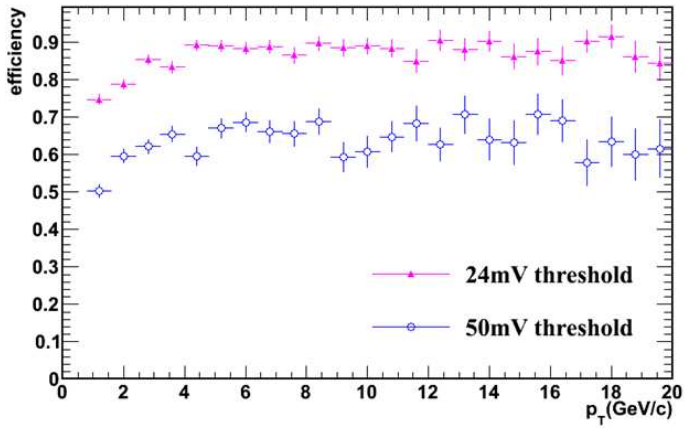

Figure 3.11: MTD efficiency for cosmic-ray data with different thresholds.

Left panel of Fig. 3.12 is the distribution of projected Z versus projected ϕ. The right is local Y versus local Z with matched track. The local means the coordinate system is built on the MTD single tray center itself. Z direction is defined as the direction along the strip and Y is perpendicular to the strip. The installed MTD trays can be seen clearly in the left plot. A dE/dx distribution can be found in Fig. 3.13 with the comparison to the expected value. Most track dE/dx is consistent with the expected μ dE/dx.

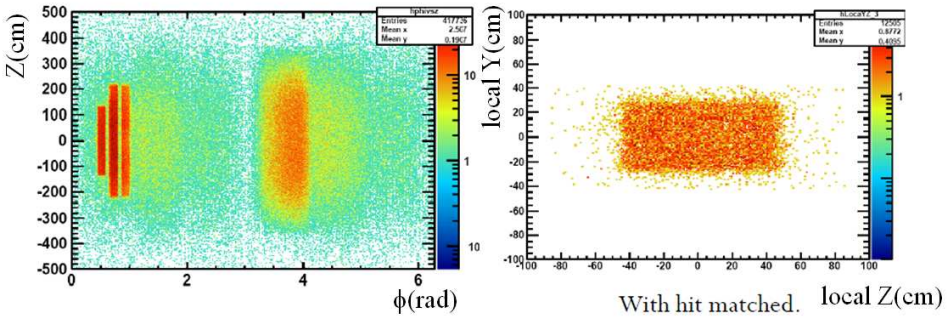

Figure 3.12: Distribution of MTD projected results. Left: projected Z vs projected ϕ. Right: local Y vs local Z.

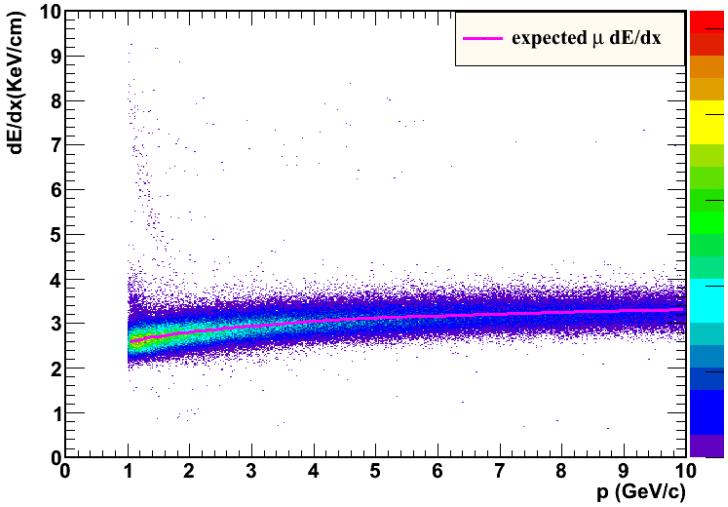

Figure 3.13: MTD matched track dE/dx compared with the expected μ dE/dx.

The spatial resolution can be obtained by fitting for the difference between track projected positions and MTD measured positions. Fig. 3.14 is the distribution of these differences. The plots on top are the two dimension version and the bottom plots are the one dimension version. A Gaussian fit is used to fit the distribution in different p_T slices to get their resolution. Because the resolution in a certain p_T range depends on the multiple scattering effect in the p_T range, a multiple scattering effect like function is used to fit the resolutions as a function of p_T. If the p_T is extended to infinite to minimize the multiple scattering effect, an intrinsic resolution can be extracted. The results can be found in Fig. 3.15. The intrinsic resolution based on cosmic-ray data is 2.6cm along the stripe and 1.9cm perpendicular to the strip.

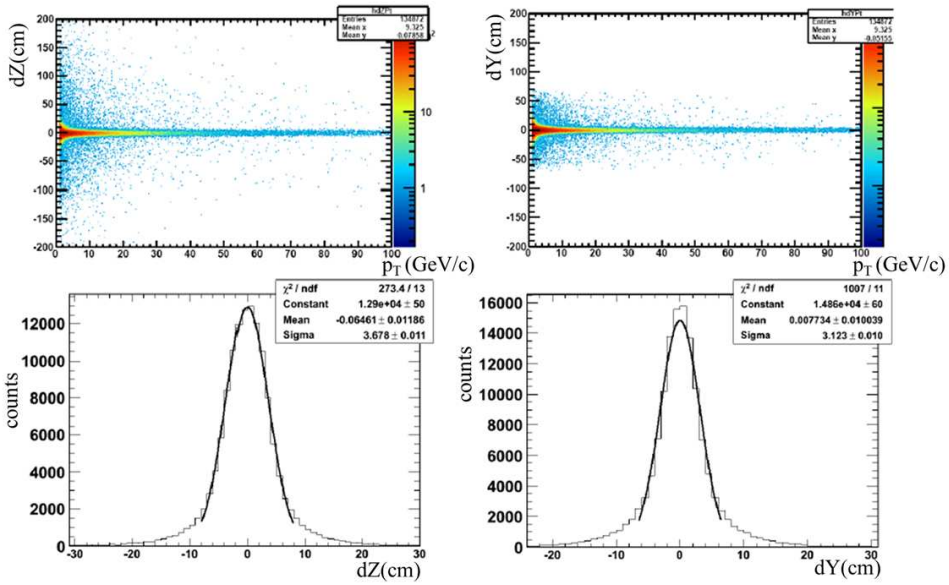

Figure 3.14: Difference of track projected positions and MTD measured positions. Upper left: Z direction difference vs p_T. Upper right: Y direction difference vs p_T. Lower left: dZ distribution. Lower right: dY distribution.

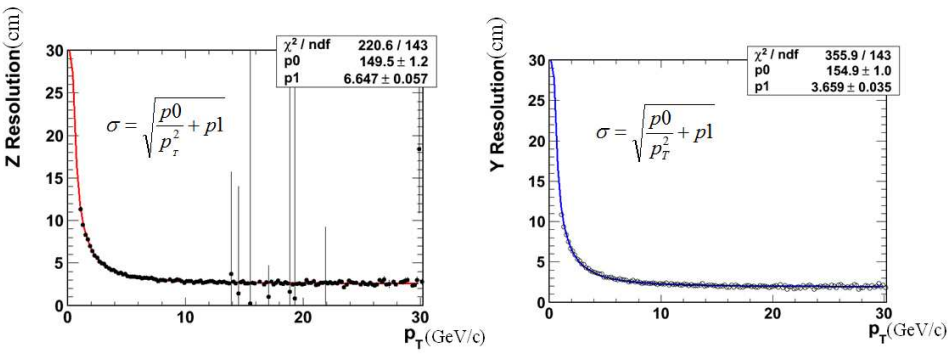

Figure 3.15: MTD spatial resolution based on Run12 cosmic-ray data. Left: Z direction. Right: Y direction.

CHAPTER 4

Direct Virtual Photon and Di-electron Production

One important physics goal of ultra-relativistic heavy-ion collisions is to study the fundamental properties of a hot, dense medium [Ada05a] created in these collisions. This medium is expected to emit thermal radiation which is in the form of direct photons and dileptons. Once produced, photons and leptons traverse the strongly interacting medium with minimal interactions (only affected by electro-magnetic interaction). So they can bring the information of the whole time evolution and dynamics of the medium.

In this chapter, the detail analysis of the direct virtual photon and di-electron production in Run10 and Run11 Au+Au collisions at $\sqrt{s_{NN}} = 200\ GeV$ will be presented. The combination of Run10 and Run11 results will be shown. The chapter includes: data set and event selection, EID, pair reconstruction, efficiency and acceptance correction, cocktail simulation, direct virtual photon production and systematic uncertainty study.

4.1 Data Set and Event Selection

In Run10 and Run11, STAR took 200 GeV Au+Au minimum bias (MB) data which were triggered by VPD and ZDC coincidence. The centrality is defined by the reference multiplicity of mid-rapidity ($|\eta| < 0.5$) measured particles. A Glauber model [MRS07] calculation is used to compare the reference multiplicity distribution. Centrality determination is obtained through the comparison. Tab. 4.1 is the centrality definition for Run10 and Run11 200 GeVAu+Au MB data.

Events in 0-80% centrality range called MB events are selected for this analysis. To improve the quality of these events, some event selection cuts in Tab. 4.2 are applied in

Table 4.1: Centrality definition on Run10 and Run11 200 GeV Au+Au collisions.

centrality	Run10	Run11
0 - 10%	> 379	> 396
10 - 20%	> 269	> 281
20 - 30%	> 184	> 193
30 - 40%	> 119	> 125
40 - 50%	> 73	> 76
50 - 60%	> 41	> 43
60 - 70%	> 21	> 22
70 - 80%	> 10	> 10

Table 4.2: Event selection cuts.

Item	Cut
$\|Vz\|$	$\leq 30cm$
$\|Vz - VpdVz\|$	$\leq 3cm$
$\|Vr\|$	$\leq 2cm$
$\|Vx\|$	$\geq$ 1e-5 cm
$\|Vy\|$	$\geq$ 1e-5 cm
$\|Vz\|$	$\geq$ 1e-5 cm

the analysis. To ensure that the events are measured in a uniform acceptance range, 30 cm cut on vertex Z is applied. The cut on $|Vz - VpdVz|$ and Vr is to reject the pile up events caused by the high interaction rate. Vz is the Z position of the vertex measured by the TPC tracking information (Sec. 2.2.2) while $VpdVz$ is the Z position of VPD measured vertex (Sec. 2.2.1). The correlation of Vz and VpdVz and the distribution of VpdVz - Vz have been discussed in Sec. 2.2.1. After all event selection cuts and bad run rejection, there are 258M and 488M events left for Run10 and Run11, respectively.

4.2 Electron Identification

To identify electrons from hadrons, a combination of TPC and TOF information is required. With the cut of the velocity of particles very close to speed of light, the energy loss dE/dx can be used to identify the electrons. The dE/dx of charged particles passing

material can be described by the Bethe-Bloch formula. These expected dE/dx distribution can be found in Fig. 2.10 as solid lines. A factor $n\sigma_P$ (Eq. 4.1) is defined in the data production and used in the analysis to identify the particles by the difference between their measured dE/dx and expected values more conveniently. The P in the equation stands for a specific particle. $(dE/dx)_{Measured}$ is the TPC measured energy loss while $(dE/dx)_{PBichsel}$ is the expected dE/dx value of Bichsel function [Bic06]. R is the resolution of TPC dE/dx [Sha06b]. The logarithm is to make the distribution more Gaussian.

$$n\sigma_P = \log[\frac{(dE/dx)_{Measured}}{(dE/dx)_{PBichsel}}]/R \tag{4.1}$$

To improve the quality of tracks, some track quality cuts shown in Tab. 4.3 are applied. The detail effects of these track cuts are :

1. p_T cut: Minimum p_T that a track can pass TPC.

2. η cut: Coverage of TPC.

3. *Global dca*: To reject tracks from secondary vertex decay.

4. $nHitsFit$: More points for track reconstruction, improve the track reconstruction precision.

5. $nHitsDedx$: More points in dE/dx measurement, improve dE/dx precision.

6. $nHitsFit/nHitsMax$: To reject double counting when reconstructing tracks.

7. $|ylocal|$: The relative Y direction position of TOF hit to the center of the readout pad, improve β precision.

The β and $n\sigma_e$ related cuts in the table are the key EID cuts. Seen from Fig. 4.1 panel *a*) which shows the $n\sigma_e$ distribution of Run11 data, the electron band is overlapped with other charged hadrons. Panel *b*) is the distribution of $1/\beta$. With a $1/\beta$ cut applied, the $n\sigma_e$ distribution will be convert to as shown in Fig. 4.2. The slow hadrons have been rejected. The electron band is clearly shown while there are still some contaminations from hadrons. That is caused by mismatching of time-of-flight and TPC tracking information. In Au+Au collisions, the occupancy of TOF is high because of the large multiplicity.

Table 4.3: Track quality cuts.

Item	Cut
p_T	$\geq 0.2\&\& \leq 50\text{GeV}/c$
$\|\eta\|$	≤ 1
$Global\ dca$	$\leq 1cm$
$nHitsFit$	≥ 20
$nHitsDedx$	≥ 16
$nHitsFit/nHitsMax$	≥ 0.52
$\|ylocal\|$	$\leq 1.8cm$
$PairY$	≤ 1
$\|1/\beta - 1/\beta_{fitmean}\|$	$\leq 0.03(1/\beta_{fitmean}\|_{p>2} = 1/\beta_{fitmean}\|_{p=2})$
$n\sigma_e$	$\leq 2.0\&\& \geq f(p)$ (Run10)
$n\sigma_e$	$\leq (2.0-0.4)\&\& \geq (f(p)-0.4)$ (Run11)
f(p) = -2.3 + 1.5p	

When there are two or more tracks hit the same TOF cell but the fastest track (such as photon which is converted into electrons in the material between TPC and TOF) is not reconstructed by TPC, the time-of-flight information will be matched to another track. This may make a fast hadron (a track with hadron dE/dx and photon time-of-flight) pass the $1/\beta$ cut. An $n\sigma_e$ cut shown as red lines is applied. The tracks between red lines are selected as electron candidates. For TPC calibration reason, the mean value of $n\sigma_e$ shifts about -0.4 in Run11. The $n\sigma_e$ cuts for Run10 and Run11 are different in order to select more good candidates. The efficiencies of these EID cuts will be discussed in Sec. 4.4.1.

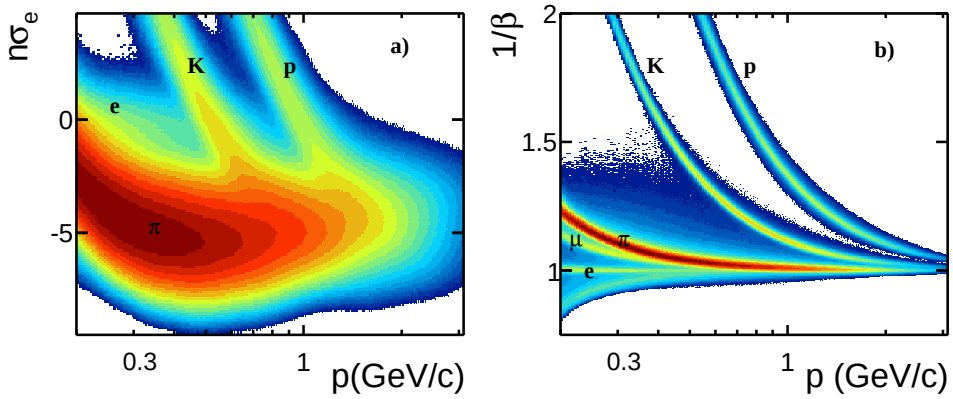

Figure 4.1: The distribution of $n\sigma_e$ and $1/\beta$ as a function of momentum. Panel a): $n\sigma_e$ vs. p. Panel b): $1/\beta$ vs. p. The bands from different particles species are marked in the plots.

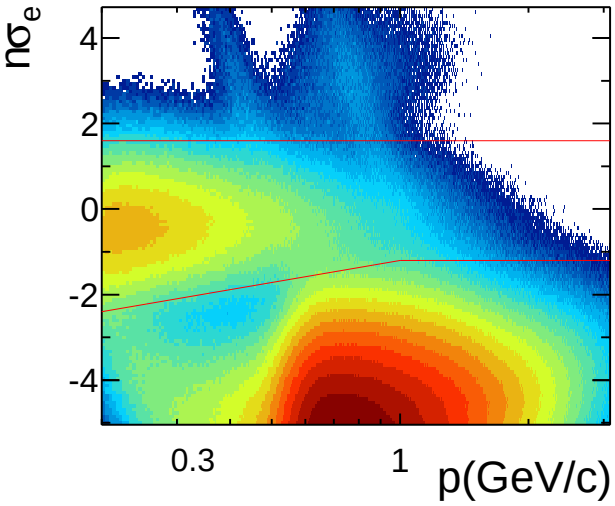

Figure 4.2: The $n\sigma_e$ as a function of momentum distribution after $1/\beta$ cut. The range between red lines is selected.

To calculate the electron purity, two Gaussian fits are used to fit the $n\sigma_e$ distribution after EID cuts. As shown in the left panel of Fig. 4.3, the red curve shows the electron distribution while the blue curve is the contamination from hadron. The ratio of the electron counts represented by the red curve versus the overall value in the same $n\sigma_e$ cut range is defined as the purity. The right panel of the plot shows the purity as a function of momentum.

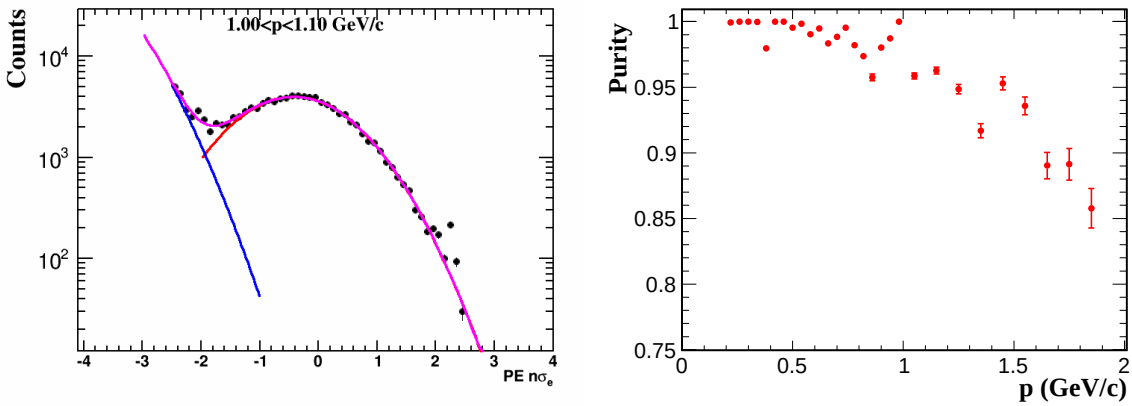

Figure 4.3: Electron purity from Run11 data. Left panel: fitting on $n\sigma_e$ distribution. The red curve is the electron contribution while the blue one comes from contamination. The pink curve is the overall fit function. Right panel: electron purity as a function of momentum.

4.3 Pair Reconstruction

To reconstruct the invariant mass (M_{ee}) distribution, a unlike-sign method is used. With this method, two electrons with different charges are combined randomly in a same event. Eq. 4.2 is the equation of M_{ee}. These electrons pairs are called unlike-sign pairs (N_{+-}) which contain both di-electron signal and background. The signal is the di-electron generated from light flavor hadron decay, heavy flavor hadron decay, Drell-Yan and thermal radiation. Fig. 4.4 is the unlike-sign M_{ee} distribution as a function of p_T. The band at about 3.1 GeV/c^2 is the signal from J/ψ. Signals from ω and ϕ which have e^+e^- decay channel is overwhelmed by the background due to the low signal/background (S/B) ratio (Fig. 4.14). The 3 bands which extend to high p_T in the very low mass region (0-0.2 GeV/c^2) are the gamma conversion contamination which will be discussed in Sec. 4.3.1.3.

$$M^2_{e^+e^-} = (E_+ + E_-)^2 - (\overrightarrow{p}_+ + \overrightarrow{p}_-)^2 \tag{4.2}$$

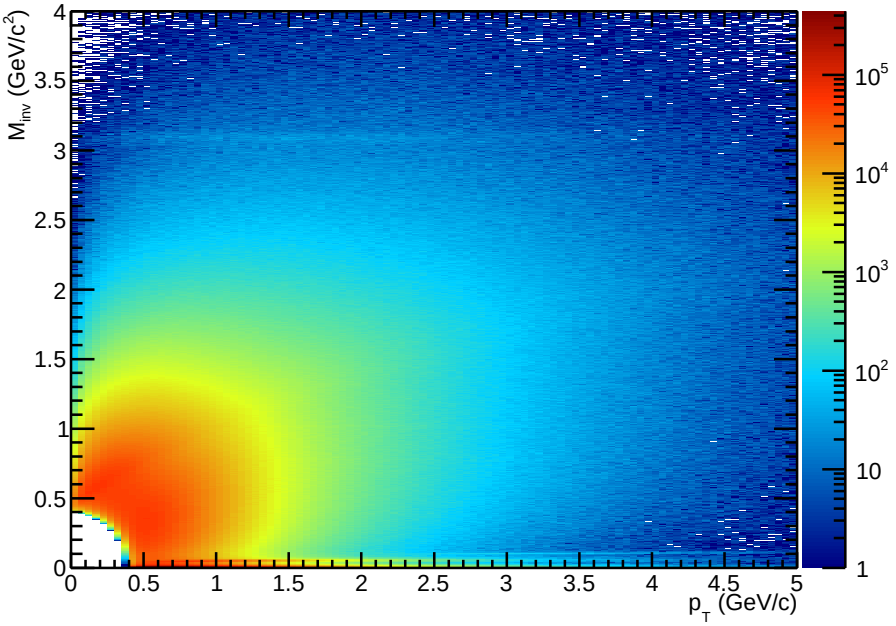

Figure 4.4: Invariant mass (M_{ee}) distribution of random combination on e^+e^- pair in same event as a function of p_T with Run11 data.

4.3.1 Background study

To get the di-electron signal, some methods for background reconstruction are studied. With the reconstructed background subtracted from unlike-sign pair, the real signal can be generated.

4.3.1.1 Like-sign method

This like-sign method is to combine the like-sign ee pair (N_{++} and N_{--}) in the same event. The only expected M_{ee} distribution difference between this like-sign ee pair and the background came from unlike-sign e^+e^- pair is the acceptance difference. This will be discussed in Sec. 4.4.3. With this acceptance difference corrected for, the signal can be generated by just subtracting the like-sign background from unlike-sign pairs. Eq. 4.3 is the formula for di-electron signal with like-sign method. $F_{acc}(M_{ee}, p_T)$ is calculated by Eq. 4.4. A geometrical mean of (N_{++} and N_{--}) is used to get the average value of like-sign pairs. In high p_T, for some bins having a zero N_{++} or N_{--}, the average of N_{++} and N_{--} is more close to the real value. Fig. 4.5 is the signal with this like-sign method. A ϕ_V cut (Sec. 4.3.1.3) is applied to reject gamma conversion background. The advantages of the like-sign method is: 1) good description on background, low residual background after background subtraction. 2) can describe correlated background. The correlated background in unlike-sign pair came from the combination of e^+e^- which are not from the same parent (not a signal) but have correlation. For example, many correlated background came from this case: one $e^{\pm}$ came from π^0 Dalitz decay ($\pi^0 \to \gamma + e^+ + e^-$) and the other $e^{\mp}$ came from the gamma conversion e^+e^- pair while the conversion gamma is from that Dalitz decay. This e^+e^- pair is not a signal but has correlation.

$$Signal(M_{ee}, p_T) = N_{+-}(M_{ee}, p_T) - F_{acc}(M_{ee}, p_T) \times 2\sqrt{N_{++}(M_{ee}, p_T) N_{--}(M_{ee}, p_T)} \quad (4.3)$$

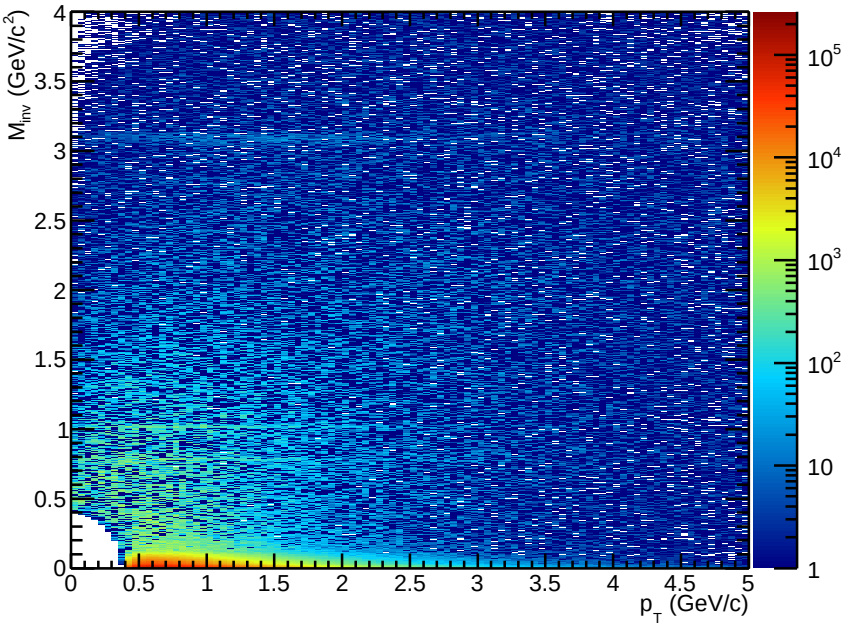

Figure 4.5: Di-electron signals (M_{ee} *vs* p_T) with like-sign background reconstruction method for Run11 data.

4.3.1.2 Mixed-event method

The mixed-event method is another way to reconstruct the background. Different events with same or similar properties are put in the same event buffer. This method is to combine e^+e^- pair from choosing the electron candidates from different events (B_{+-}). There is absolutely no correlation between two electron candidates in a pair. The same or similar properties of these mixed events can make this combination describe the unlike-sign background in the same event more precisely. In this analysis, 2 magnetic field bins, 10 vertex Z bins, 9 centrality bins, 12 event plane bins are used to selected events for mixing. Only the events in the same magnetic field, vz, centrality and event plane bin can be used to mix with each other. The event pool size is set to 300 and the number of event pools is $2\times10\times9\times12$. 50 M events are combined together for a individual job process to make sure that the average mixed times for a event is larger than 299. The like-sign mixed pairs (B_{++} and B_{--}) are also generated for acceptance correction purpose. The large event pool size is to improve the statistics of mixed pair for acceptance correction

in high p_T in order to reduce the uncertainty. The advantages of this method is: 1) low statistical errors. 2) can be used to describe the acceptance difference between unlike-sign and like-sign ee pair (Eq. 4.4, Sec. 4.4.3). But this method can not reconstruct the correlated background. Fig. 4.6 is the signal with this mixed-event method. To subtract correlated background and improve the statistical errors, a mixture of like-sign signal and mixed-event signal is generated. The combined signal is like-sign signal ($M_{ee} < 0.7$ GeV/c^2) plus mixed-event signal ($M_{ee} \geq 0.7$ GeV/c^2).

$$F_{acc}(M_{ee}, p_T) = \frac{B_{+-}(M_{ee}, p_T)}{2\sqrt{B_{++}(M_{ee}, p_T)B_{--}(M_{ee}, p_T)}} \tag{4.4}$$

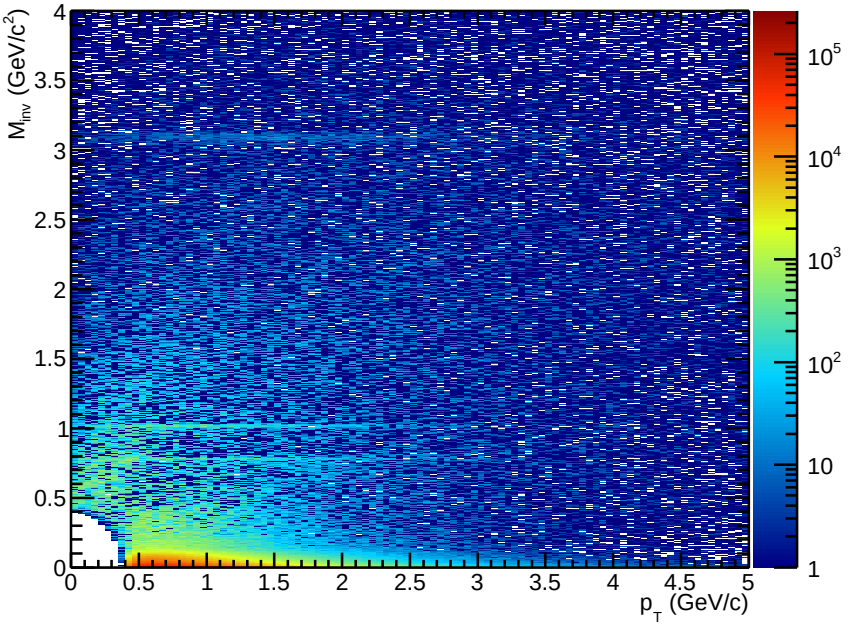

Figure 4.6: Di-electron signals (M_{ee} *vs* p_T) with mixed-event method with Run11 data.

4.3.1.3 Gamma conversion rejection

Some e^+e^-pairs are from the gamma conversion caused by the interaction between γ and the detector material. These pairs need to be rejected but can not be reconstructed by neither like-sign method nor mixed-event method. The 3 bands in Fig. 4.4 which

extend to high p_T in the very low mass region (0-0.2 GeV/c^2) is due to this conversion process. To reject these background, a ϕ_V cut is applied. The angle ϕ_V is defined as Eq. 4.3.1.3. The opening angle of the conversion e^+e^- pair should be very close to 0. This angle is the angle of two global tracks from a conversion vertex. After these global tracks are reconstructed to primary vertex as primary tracks, this opening angle should still be small. Fig. 4.7 is a simulation result for ϕ_V distribution of gamma conversion. There are 3 bumps from low to high mass corresponding to 3 material layers. These material layers are beam pipe ($r \sim 4cm$), inner cone supporting structure ($r \sim 20cm$) and TPC inner field cage($r \sim 46cm$). The position of these bumps are consistent with the observation from data (Fig. 4.4). The position and relative amplitude of these gamma conversion bumps have some p_T dependence. Seen from Fig. 4.7, with the increasing p_T, the "height" of third bump around 0.11 GeV/c^2 increases and the mass shifts a little bit higher. The red line in the plot is the applied ϕ_V cut. The e^+e^- pairs with ϕ_V below the line are dropped. This cut is applied to all ee pairs of different methods. The overall gamma conversion rejection rate calculated from simulation is about 99%. From the simulated ϕ_V distribution from π^0 decayed e^+e^- pairs, the ϕ_V cut efficiency can be generated. Since there is no significant p_T dependence for π^0 decayed e^+e^- pairs' ϕ_V distribution, the cut efficiency for all p_T range is applied to every single p_T slice when correct di-electron pair detection efficiency. Fig. 4.8 shows the ϕ_V cut efficiency and the fit function used for efficiency correction.

$$\hat{u} = \frac{\overrightarrow{p}_+ + \overrightarrow{p}_-}{|\overrightarrow{p}_+ + \overrightarrow{p}_-|}, \quad \hat{v} = \frac{\overrightarrow{p}_+ \times \overrightarrow{p}_-}{|\overrightarrow{p}_+ \times \overrightarrow{p}_-|} \tag{4.5}$$

$$\hat{w} = \hat{u} \times \hat{v}, \hat{w_z} = \hat{u} \times \hat{z} \tag{4.6}$$

$$cos\phi_V = \hat{w} \bullet \hat{w_z} \tag{4.7}$$

Another possible way is to use global tracks to reconstruct M_{ee}. The two gamma conversion electron tracks have nearly same momentum direction at the conversion vertex.

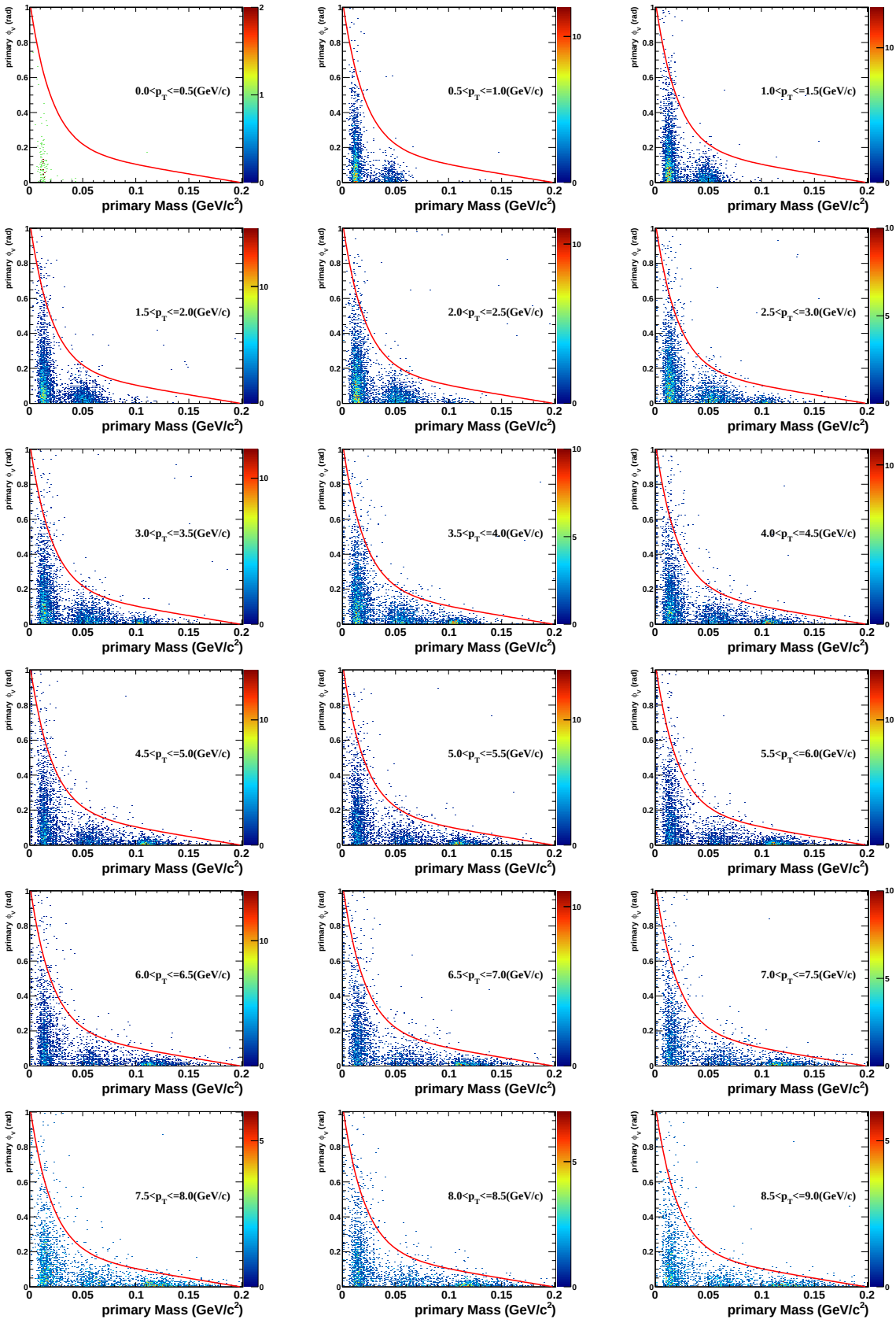

Figure 4.7: Simulation on ϕ_V distribution of gamma conversion in different p_T slices.

With reconstructing M_{ee} by their global momentum at the conversion vertex (the point where two global tracks are closet to each other), the 3 gamma conversion bumps should be moved to 0 GeV/c^2. Fig. 4.9 is the distribution of M_{ee} difference between global tracks and primary tracks as a function of global mass. There are still some gamma conversion bands crossing zero with a nonzero global mass. This is caused by the worse momentum resolution of global tracks compared to primary tracks, and the reconstructed global M_{ee} can not be moved to perfect around 0 for gamma conversion e^+e^- pair. Due to this, the global mass method is not suitable to reject the gamma conversion background.

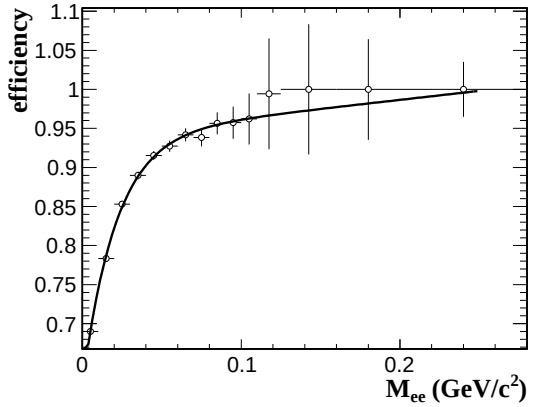

Figure 4.8: ϕ_V cut efficiency based on the simulation results.

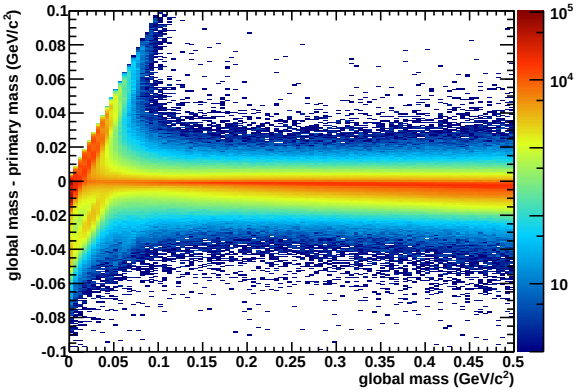

Figure 4.9: The distribution of M_{ee} difference (global mass - primary mass) as a function of global mass.

4.3.2 Raw signal

Fig. 4.10 and Fig. 4.11 shows the M_{ee} distribution for different ee pairs. The right panel is a zoom in view of different backgrounds. In the low mass region, the mixed-event background is systematically lower than the like-sign background due to the correlated background mentioned in Sec. 4.3.1.1. With the like-sign background and mixed-event background subtracted, the raw signal without efficiency correction can be generated. Fig. 4.12 and Fig. 4.13 show the raw signal with like-sign method and mixed-event method of Run10 and Run11 data, respectively. The left panels for both figures are zoom in views in low mass region without number of events and histogram bin width normalizing. The right panels are the raw signals corrected by number of events and histogram bin width. The e^+e^- pair p_T range is 0 - 10 GeV/c for all these plots.

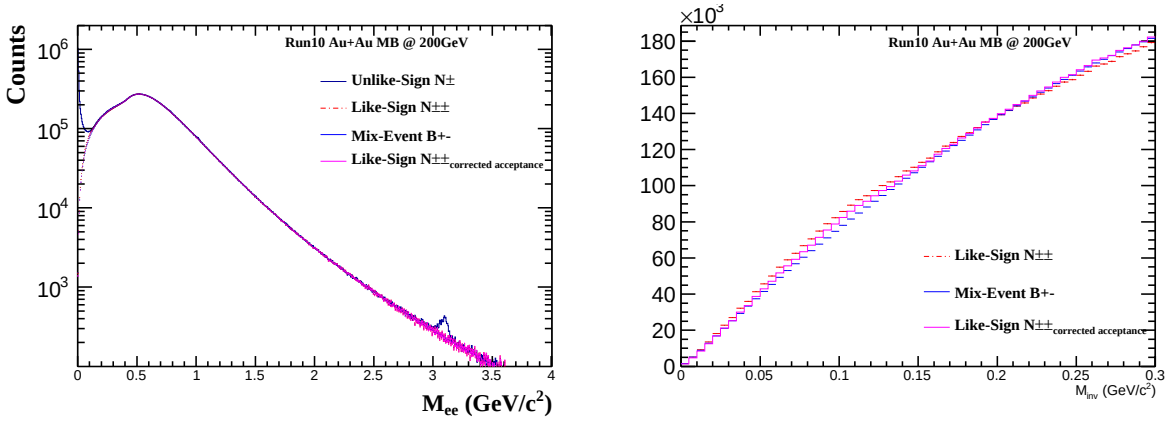

Figure 4.10: The distribution of M_{ee} with different reconstruction methods for Run10 data.

The lower mixed-event background in low mass region compared to like-sign method will give a higher raw signal. This can be seen in the left panels of Fig. 4.12 and Fig. 4.13.

Fig. 4.14 shows the signal over background ratio with like-sign method. Seen from the plots, this analysis is studied in very low signal to background ratio. All backgrounds and efficiencies need to be reconstructed with high precision.

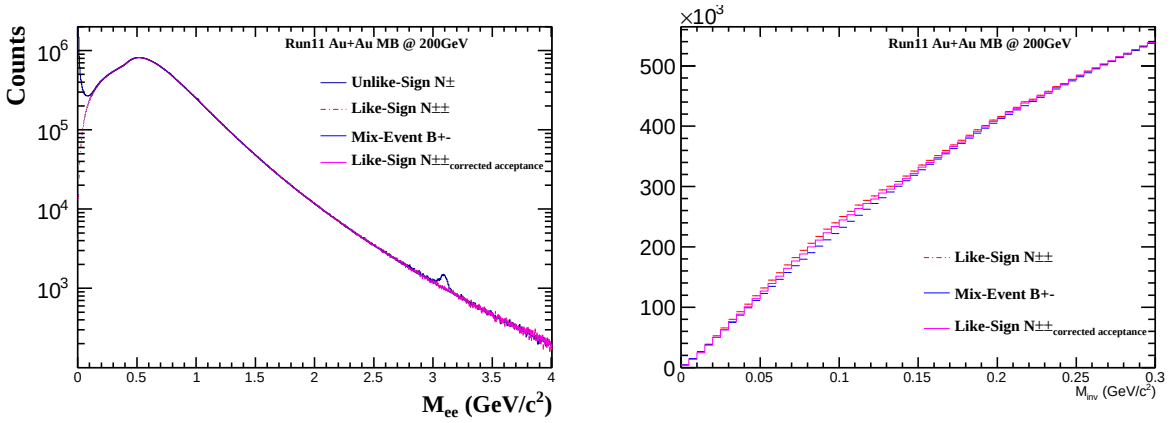

Figure 4.11: The distribution of M_{ee} with different reconstruction methods for Run11 data.

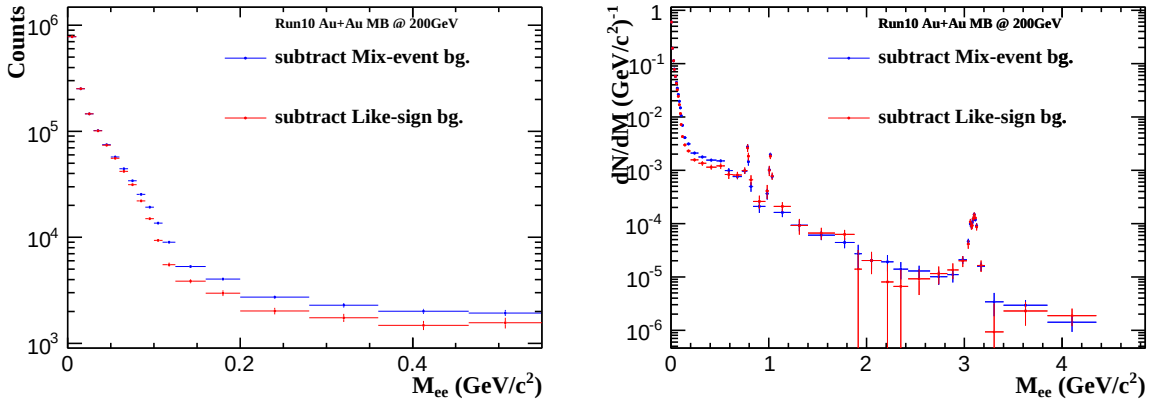

Figure 4.12: The di-electron raw signal for Run10 data. Left panel: in low mass region w/o number of events and bin width correction. Right panel: w/ number of events and bin width correction.

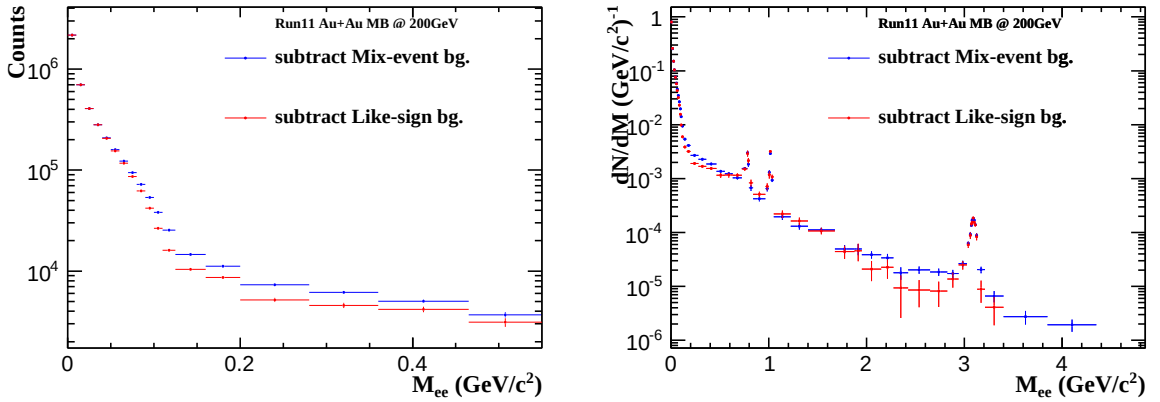

Figure 4.13: The di-electron raw signal for Run11 data. Left panel: in low mass region w/o number of events and bin width correction. Right panel: w/ number of events and bin width correction.

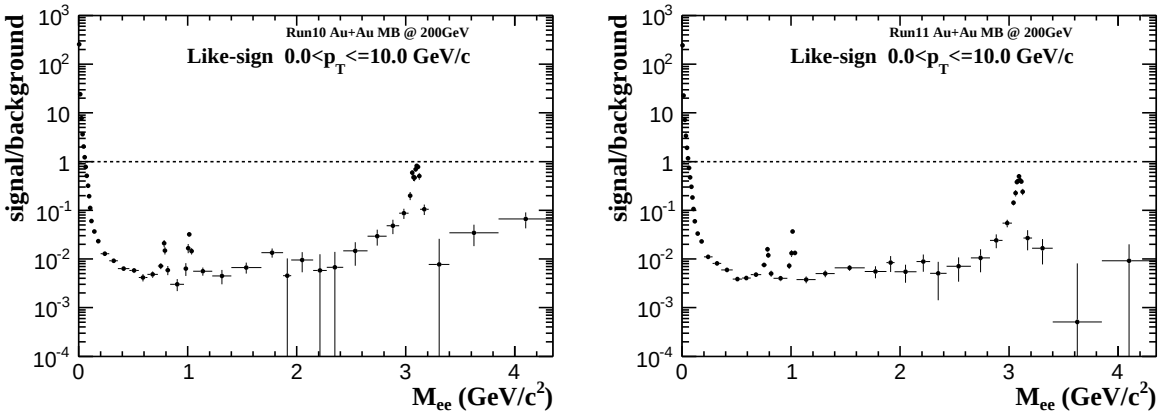

Figure 4.14: Signal over background ratio with likesign method. Left panel: Run10 data. Right panel: Run11 data.

4.4 Efficiency and Acceptance

STAR is not an ideal detector with full coverage and 100% efficiency. The whole system has its unique acceptance and every subsystem has its own acceptance and detection efficiency. Also the EID cuts have their cut efficiencies, respectively. To restore the original information generated by the collisions, all the related efficiencies need to be considered and corrected. In this analysis, the main used detectors are TPC and TOF. The TPC tracking efficiency which stands for the possibility that a real track can be reconstructed by TPC information and TOF matching efficiency which stands for the possibility that a track passed TOF can leave a hit information will be used for efficiency correction while the acceptance caused by TPC and TOF detailed geometry should be included in. Other cut efficiencies including $nHitsDedx$ cut efficiency, $n\sigma_e$ cut efficiency and $1/\beta$ cut efficiency will be taken into account.

4.4.1 Single track efficiency

In Sec. 2.2.2, the method of TPC tracking reconstruction is mentioned. To obtain the TPC tracking efficiency, some electrons are embedded in a real event ([Ago03, All06]). This simulated event passes the TPC tracking reconstruction steps again to get the reconstructed information for those embedded electron tracks. With the comparison between

the embedding electron and corresponding reconstructed tracks (number of reconstructed embedded tracks / number of input embedded tracks), the TPC tracking efficiency can be generated. For the acceptance of TPC have η and ϕ dependence, a three dimension (p_T, η, ϕ) efficiency is generated for further pair efficiency correction. Fig. 4.15 shows the ϕ dependence of the TPC tracking efficiency. In Run10, there is a dead TPC sector. This can be seen clearly in these plots. The drop of the efficiency is caused by the edges and gaps of the TPC sectors. The effect of the dead sector in Run10 can be clearly seen from the upper plots. In this analysis, 20 η bins and 36 ϕ bins (12 *sectors per side* $\times$ 3) are used to divide the TPC tracking efficiency. The efficiency for *Global dca*, $nHitsFit, nHitsFit/nHitsMax$ cuts are all included in this efficiency calculation. Fig. 4.16 is the TPC tracking efficiency as a function of p_T for Run10 and Run11.

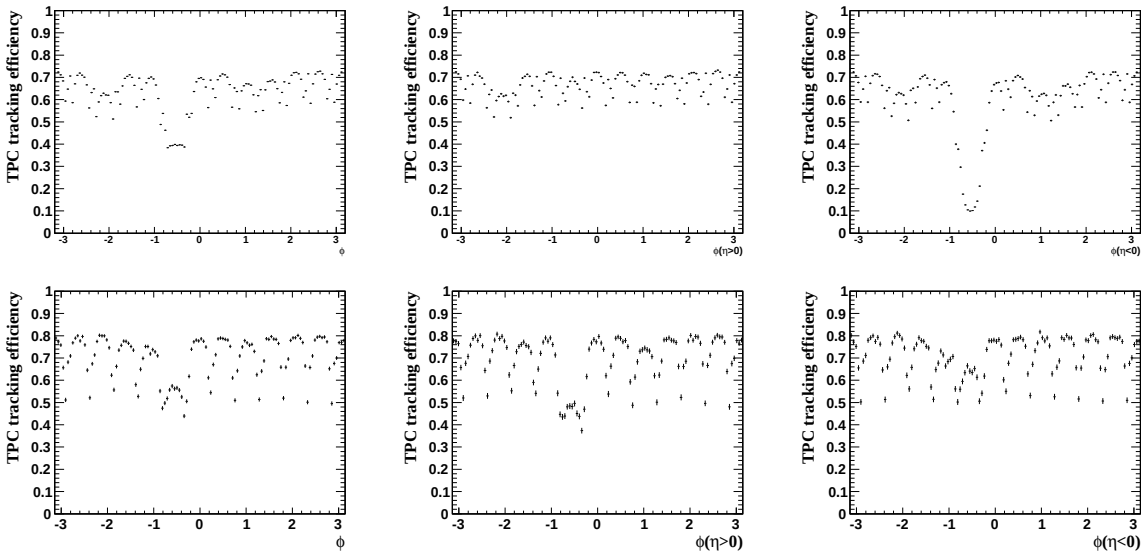

Figure 4.15: ϕ dependence of TPC tracking efficiency. Upper panels: Run10. Lower panels: Run11.

For $nHitsDedx$ cut efficiency, the distribution from embedding does not describe the real data $nHitsDedx$ distribution very well. So this efficiency is studied individually with the real data. The efficiency definition is shown in Eq. 4.8. Fig. 4.17 shows the $nHitsDedx$ cut efficiency.

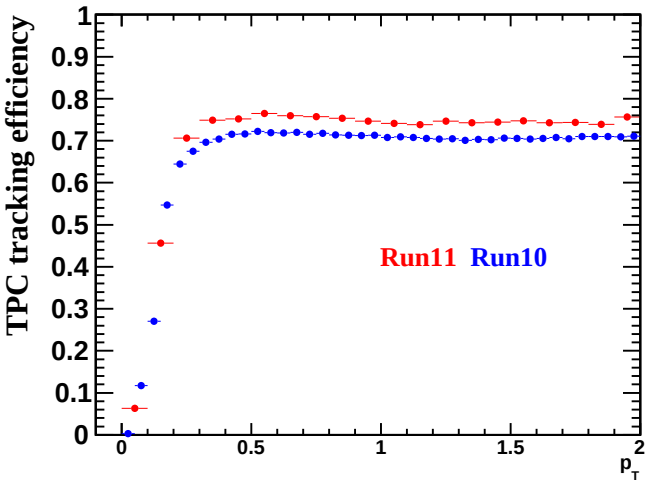

Figure 4.16: TPC tracking efficiency for Run10 and Run11. Blue: Run10. Red: Run11.

$$\varepsilon_{nHitsDedx} = \frac{N_{pass\ other\ track\ quality\ cuts+nHitsDedx\ cut}}{N_{pass\ other\ track\ quality\ cuts}} \tag{4.8}$$

For TOF related efficiencies, the TOF matching efficiency is defined as a ratio in which the denominator is the number of electron tracks which pass the TPC track quality cuts while the numerator is the number of electron tracks which pass the TPC track quality cuts and have TOF matching. Similar to TPC tracking efficiency, for acceptance reason, the TOF matching efficiency is divided into 20 η bins and 60 ϕ bins (60 *trays per side*). This η and ϕ dependence can be seen in Fig. 4.18. The TOF matching efficiency is calculated by using pure electron sample. The photonic electron which comes from the gamma conversion (Sec. 4.3.1.3) is chosen as this pure sample. By cutting on the opening angle of global momentum ($< 0.1\pi$), the invariant mass (< 0.005 GeV/c^2) and the dca ($< 1cm$) of a e^+e^- pair, the photonic electron sample are selected. Fig. 4.19 is the TOF matching efficiencies for different particles of Run10 and Run11, respectively. Due to the limit on statistics, the efficiency of π is used as the electron efficiency by correcting the overall difference between them. This sample is also used to generate $1/\beta$ and $n\sigma$ cut efficiencies. A Gaussian fit is applied to the $1/\beta$ distribution in different momentum slices (Fig. 4.21 left panel). The $1/\beta$ cut is cutting on the difference between $1/\beta$ and these $1/\beta$

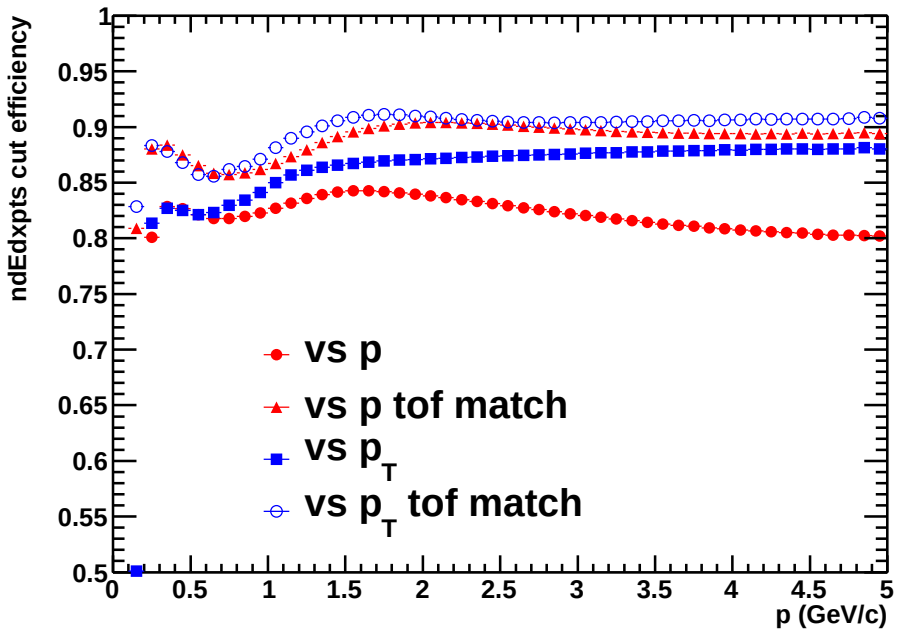

Figure 4.17: $nHitsDedx$ cut efficiency for Run11.

Gaussian fit mean values. Fig. 4.20 is the photonic electron $1/\beta$ distribution for Run11 data. The red markers are the Gaussian fit mean values while the red lines are the upper and lower cut edges. The blue line is the fitting results on these Gaussian fit means for Run10 data. Fig. 4.21 shows the $1/\beta$ cut efficiency for Run10 and Run11. Seen from the plots, the $1/\beta$ cut efficiency is close to 100%.

For the $n\sigma_e$ cut efficiency calculation, a Gaussian function is used to fit the electron $n\sigma_e$ distribution to constrain the electron $n\sigma_e$ distribution. By taking the ratio of the integral of this Gaussian function in cut range over the overall value, the $n\sigma_e$ cut efficiency can be obtained. Fig. 4.22 shows the $n\sigma_e$ cut efficiency based on the cut shown in Tab. 4.3. The efficiencies for two other different cuts with loose (primary lower limit - 0.2) and tight (primary lower limit + 0.2) lower cut limits are also calculated for comparison. The mean values of $n\sigma_e$ shown in the right panels explain the shift of the cuts between Run10 and Run11.

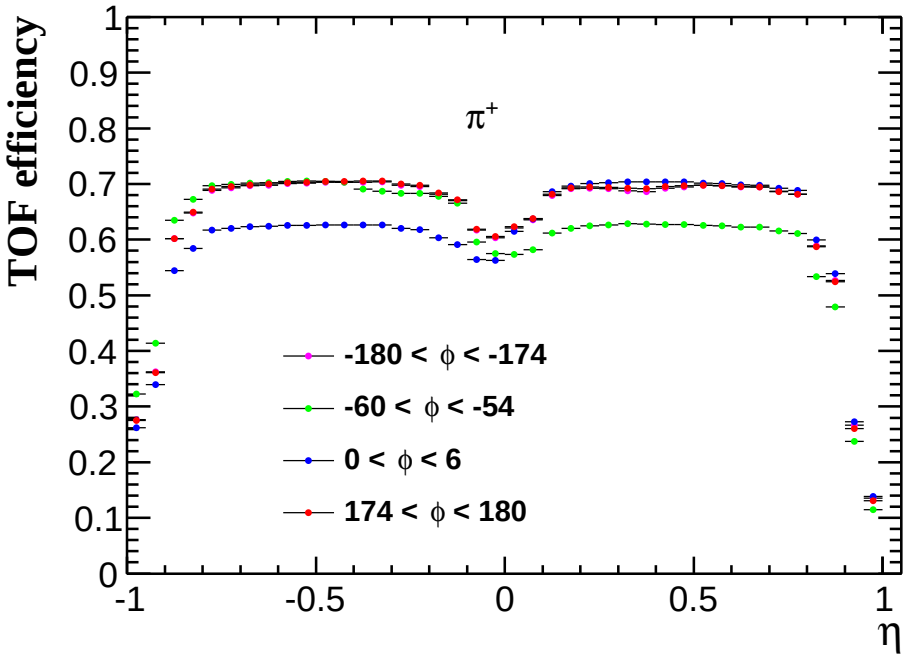

Figure 4.18: η and ϕ dependence of TOF matching efficiency for Run11 π^+

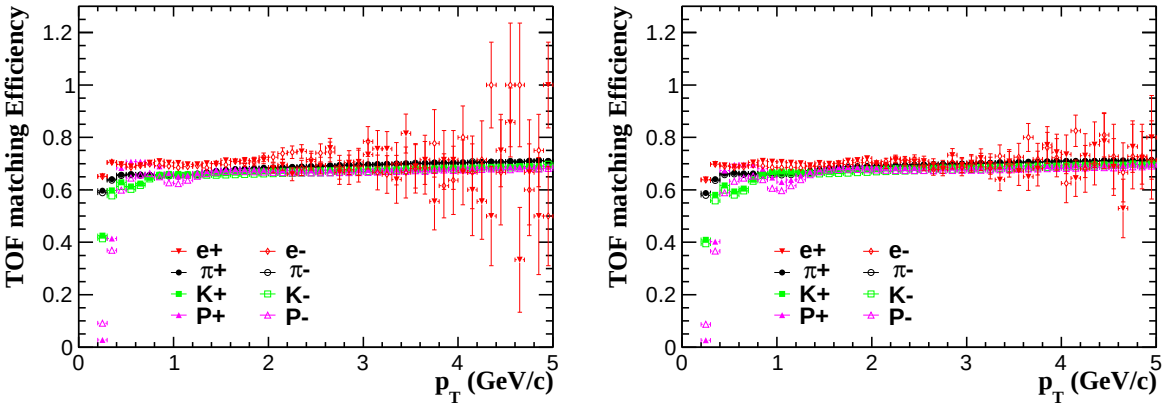

Figure 4.19: TOF matching efficiencies of different particle species for Run10 and Run11. Left panel: Run10. Right panel: Run11.

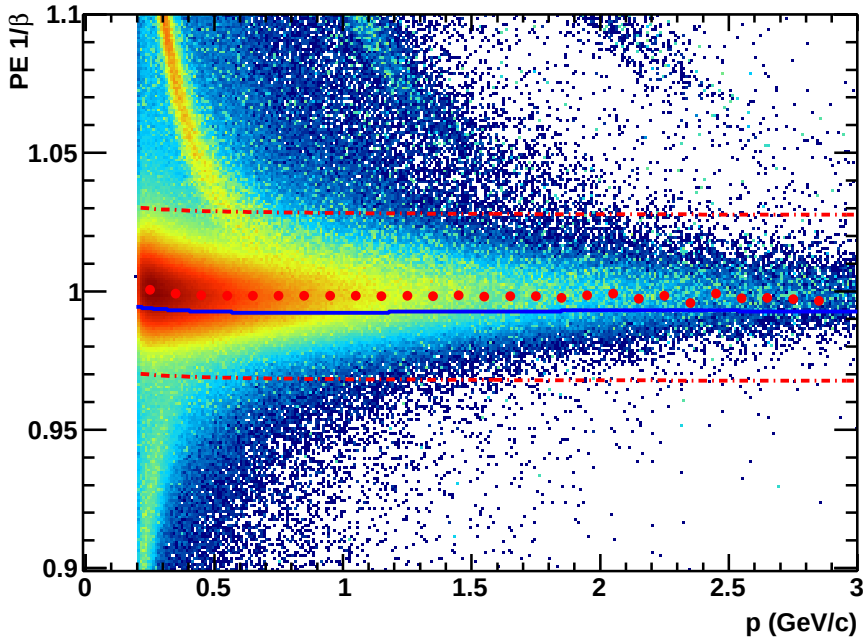

Figure 4.20: Electron $1/\beta$ distribution for Run11 data. The red lines are the upper and lower cut edges. The red markers are the Gaussian fit means in different momentum slices. The blue line is the fitting result on these fit means for Run10 data.

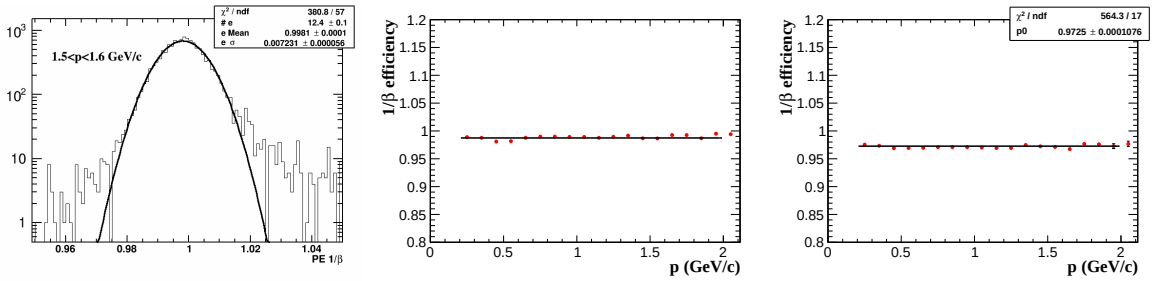

Figure 4.21: Left panel: Gaussian fit on $1/\beta$ distribution in a momentum slice for Run11. Middle panel: Run11 $1/\beta$ cut efficiency. Right panel: Run10 $1/\beta$ cut efficiency.

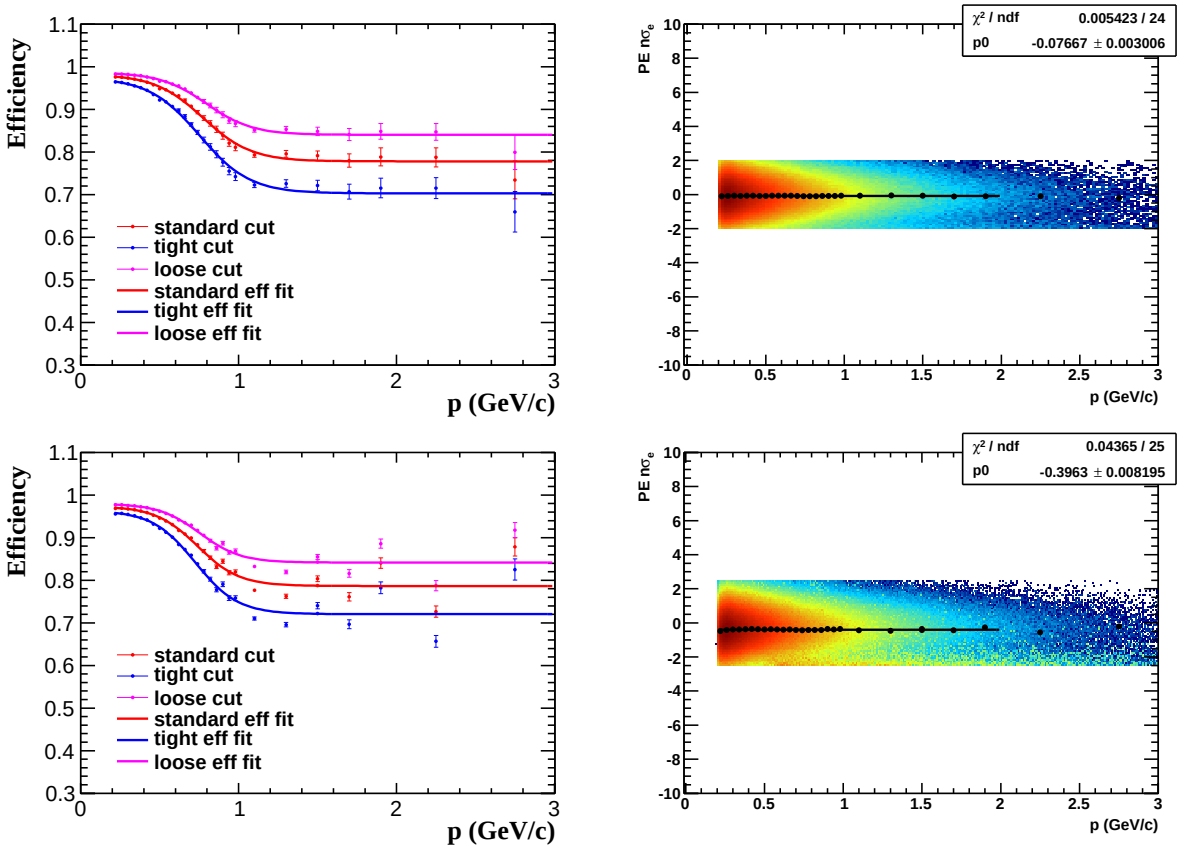

Figure 4.22: $n\sigma_e$ cut efficiencies for Run10 and Run11. Upper panels: Run10. Lower panels: Run11. Left panels: $n\sigma_e$ cut efficiency. Right panels: $n\sigma_e$ distribution of the photonic electron sample.

4.4.2 Pair efficiency

With the results of all single track efficiencies, a pair efficiency can be generated by combining the simulations of different di-electron sources. This simulation folding method is to use the decay kinematics of different di-electron sources with a flat η and ϕ input. The input p_T distribution for these sources is the measured value. The meson momentum spectra are collected from previous publications at RHIC energy. For heavy flavor components, the non-photonic electron p_T spectra and PYTHIA [SMS06] were used for sampling. The details of the cocktail related simulation will be discussed in Sec. 4.5.

To get the overall single track efficiency, the product of different single track efficiencies which is generated by evaluating the specific p_T or momentum of the track is used. The product of the positron and electron overall single track efficiencies stands for the pair efficiency of this e^+e^- pair. To determine the efficiency bias caused by different kinematics, two cocktails are generated by the method shown in Sec. 4.5. One cocktail (*cocktail acc*) used as the denominator is the cocktail within the STAR acceptance ($p_T(e) > 0.2\ GeV/c$, $|y_{e^+e^-}| < 1\ and\ |\eta_e| < 1$). Weighted by the positron and electron single track efficiency respectively, the cocktail (*cocktail eff*) can be generated accordingly. These cocktails can be found in Fig. 4.27. Multiplied by the ϕ_V cut efficiency, the ratio (*cocktail eff / cocktail acc*) is the pair detection efficiency within STAR acceptance. Fig. 4.23 shows the di-electron pair detection efficiency without ϕ_V cut efficiency in different p_T slices.

4.4.3 Acceptance

All of the analysis results based on STAR data is within the STAR acceptance which is $p_T(e) > 0.2\ GeV/c\ and\ |\eta_e| < 1$. For the di-electron measurement, the measurement is in $|y_{e^+e^-}| < 1$. $p_T(e) > 0.2\ GeV/c$ gives a low limit that the particle can pass TPC. $|\eta_e| < 1$ will make the track pass to TPC outer field cage. A simulated results which include the cocktail pass STAR acceptance (*cocktail acc*) and the cocktail without acceptance cuts (*cocktail mc*) (Fig. 4.27) can be generated to quantify this acceptance

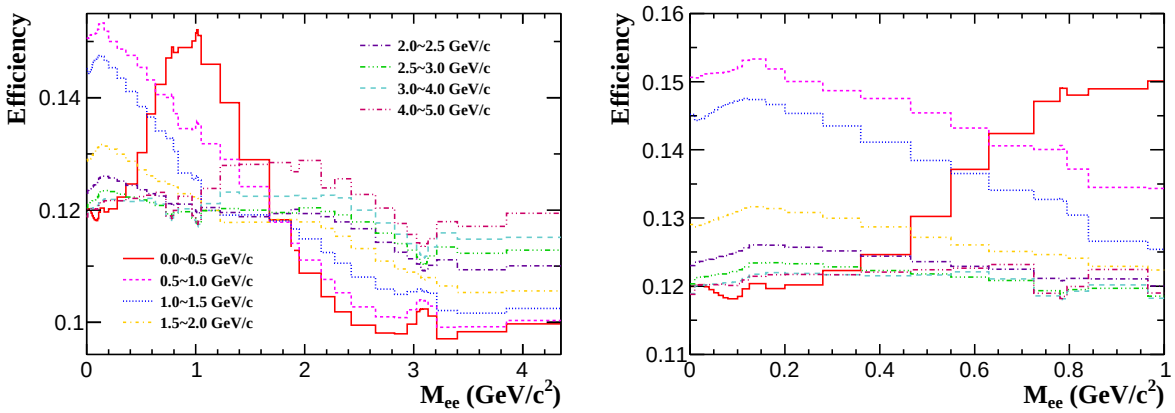

Figure 4.23: Di-electron pair detection efficiencies without ϕ_V cut efficiency in different p_T slices from Run11 Au+Au at 200 GeV.

effect (*cocktail acc / cocktail mc*). Fig. 4.24 shows the STAR acceptance effect for di-electron detection.

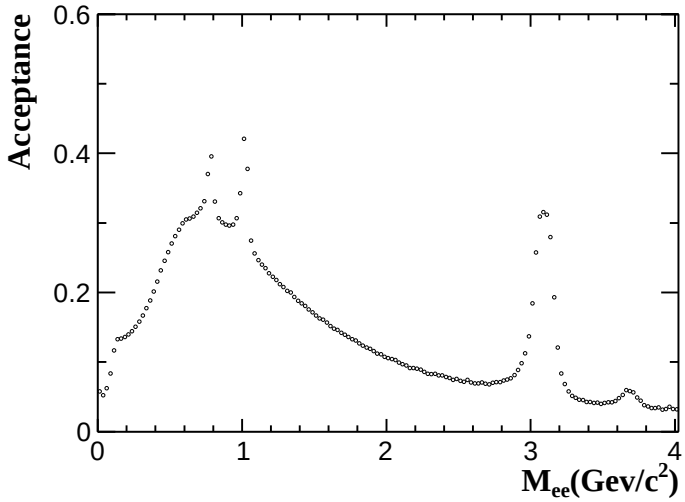

Figure 4.24: STAR acceptance in mid-rapidity for di-electron detection based on cocktail simulation (*cocktail acc / cocktail mc*).

For TPC actually does not cover the fully ϕ range, the dead area between different sectors will effect the TPC tracking efficiency. TOF also has this acceptance bias. So the efficiencies for TPC and TOF are divided into several η and ϕ bins to point this acceptance effect out. This η and ϕ dependence can be found in Fig. 4.15 and Fig. 4.18. This detailed geometry bias of TPC will also effect the acceptance difference between unlike-sign ee pair and like-sign ee pair in the magnetic field. This acceptance difference

is mentioned in Sec. 4.3.1.2 and calculated by Eq. 4.4. Fig. 4.25 shows this acceptance for Run10 and Run11 calculated by Eq. 4.4. The significant difference of the two data sets is caused by the dead TPC sector in Run10 and gives a more profound explanation that this acceptance is caused by the TPC geometry.

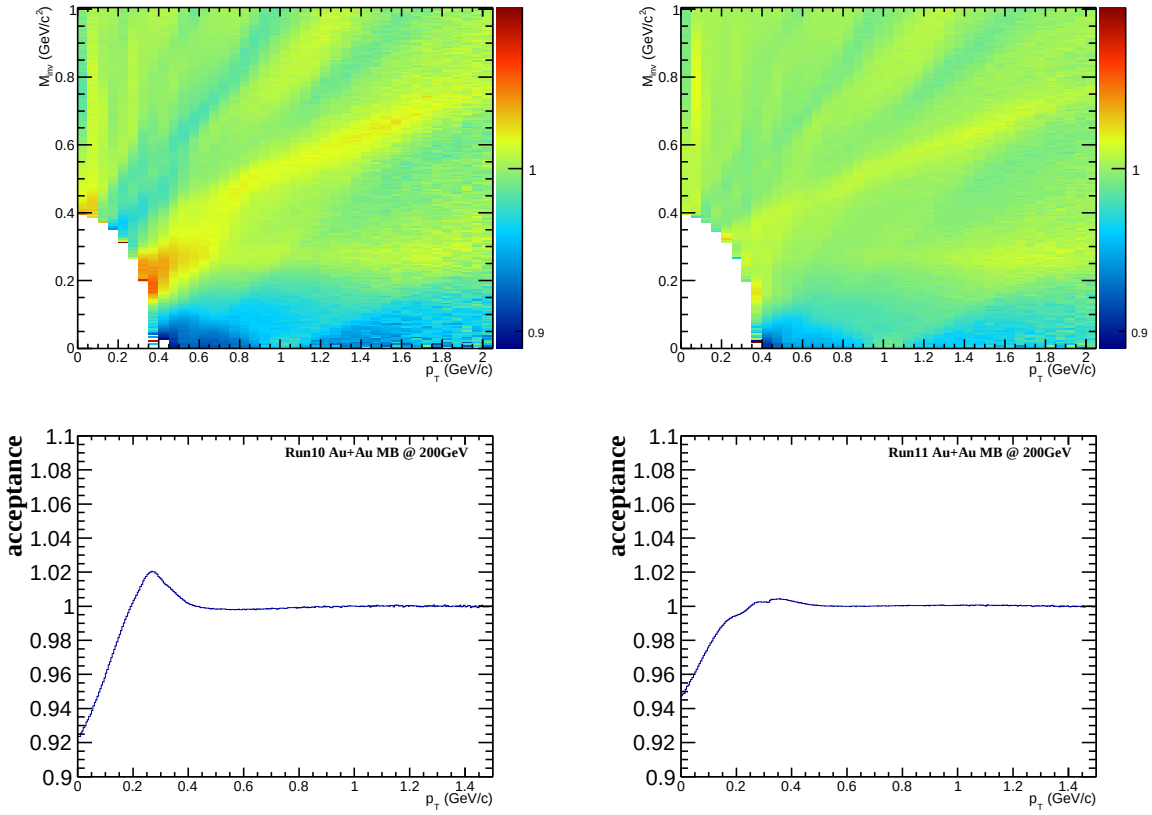

Figure 4.25: The distribution (M_{ee} *vs* p_T, *vs* p_T) of acceptance difference between unlike-sign and like-sign ee pair for Run10 and Run11. Left panels: Run10. Right panels: Run11.

In general, the STAR acceptance on di-electron detection is the acceptance of this analysis. The acceptance effects caused by TPC and TOF detailed geometry on both efficiency calculation and ee pair background reconstruction are considered and corrected.

4.5 Cocktail Simulation

The e^+e^- pairs in di-electron continuum come from the medium revolution process. The main contribution is from the decays of hadron with longer life time after the hadronic

step of the medium. The combination of all of these hadron contribution is called "cocktail" which can be studied by simulation. With the comparison between the cocktail and di-electron continuum, the physics of this analysis can be studied.

4.5.1 Light flavor meson contribution

A Monte-Carlo (MC) simulation is used to study the meson contribution. The parent particles which can contribute to di-electron are generated with flat rapidity and flat azimuthal angle distribution. The input yields of these parent particles are based on a core-corona based Tsallis Blast-Wave (TBW) model fitting [Tan09] to the published results. The references of these published results can be found in Tab. 4.4. As shown in Fig. 4.26, the TBW model can describe the meson production in a wide p_T range. With the input p_T distribution described by the TBW model, electron pairs can be generated as the daughters after the mother particles pass the decay process with the expected dynamics. For two body decays, the mass width of the mother particles are very small compared to the mass smearing due to the detector momentum resolution. These mass widths are from PDG [Ams08]. For Dalitz decays, the Kroll-Wada expression [KW55] is used for the π^0, η, $\eta' \to \gamma ee$, and $\omega \to \pi^0 ee$, $\phi \to \eta ee$ Dalitz decay calculation. In this calculation, a electromagnetic transition form factor in vacuum is considered. Eq. 4.9 shows the formula used for π^0 Dalitz decay:

$$\frac{dN}{dm_{ee}} \propto \sqrt{1-\frac{4m_e^2}{m_{ee}^2}}(1+\frac{2m_e^2}{m_{ee}^2})\frac{1}{m_{ee}}(1-\frac{m_{ee}^2}{M_h^2})^3|F(m_{ee}^2)|^2 \tag{4.9}$$

where m_e is the electron mass, m_{ee} is the e^+e^- pair mass, M_h is the mass of the hadron which decays into di-electrons. F is the electro-magnetic transition form factor.

Every meson source from a certain decay channel is weighted by its branch ratio and rapidity density (dN/dy). The sum of these meson sources is the meson contribution part in the cocktail. Adding by the contribution from heavy flavor sources, a cocktail without acceptance correction (*cocktail mc*) can be obtained. A cocktail within STAR acceptance (*cocktail acc*) which is mentioned in Sec. 4.4.3 and a cocktail weighted by

efficiency ($cocktail\ eff$) which is mentioned in Sec. 4.4.2 can be generated accordingly. These cocktails are shown in Fig. 4.27.

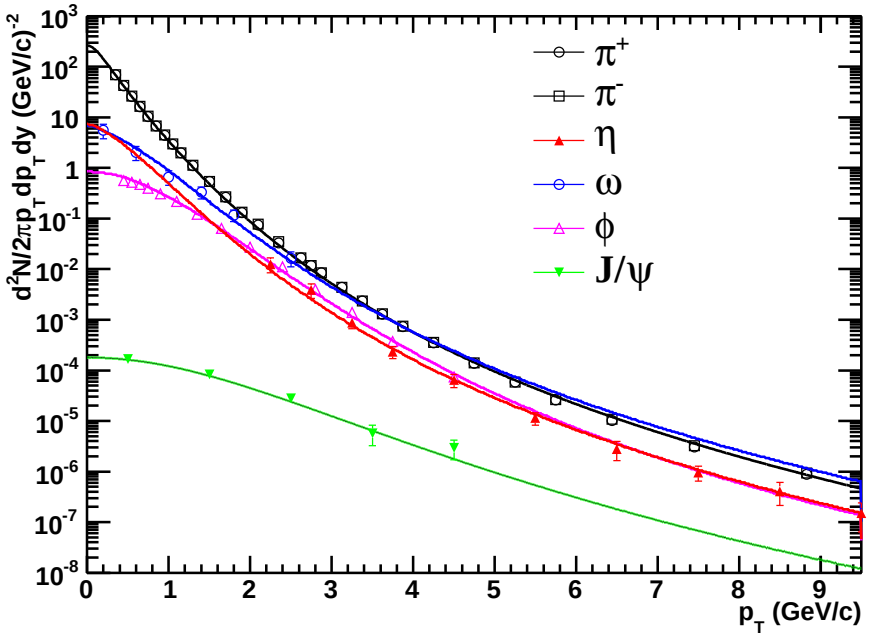

Figure 4.26: The Tsallis Blast-Wave model fitting for meson sources which are involved in cocktail simulation. The meson production are from published results in Au+Au at 200 GeV.

Tab. 4.4 list the branch ratio and dN/dy for different meson sources. The references and uncertainties are also given in the table. The uncertainty of the dN/dy input especially for π^0 and η will affect the direct virtual photon analysis results significantly. This is considered as the systematic uncertainty and will be discussed in Sec. 4.8.

4.5.2 Heavy flavor contribution

For heavy flavor source, PYTHIA [SMS06] is used as the generator to calculated these processes in $p+p$ collisions. The cross sections and branch ratios of these heavy flavor sources are listed in Tab. 4.4. For charm contribution, the branch ratios are considered respectively according to the mother particles (D mesons) of the final e^+e^- pair in PYTHIA simulation. For bottom contribution, these branch ratios are also applied individually based on the final e^+e^- pairs' mother particles (B mesons). In Au+Au collisions,

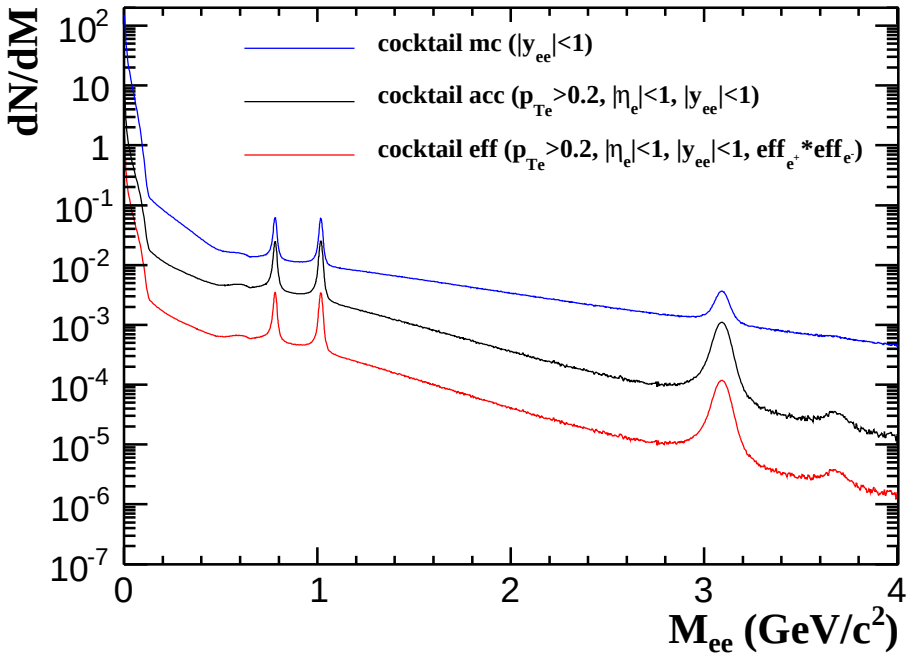

Figure 4.27: Cocktails for different acceptance settings and Run11 efficiency weighting.

Table 4.4: Branch ratio and rapidity densities (dN/dy) for different sources in the cocktail simulation.

Source	Branch ratio	dN/dy or σ	Uncertainty
$\pi^0 \rightarrow \gamma ee$	1.174×10^{-2}	98.5	8% [Ada04, Abe06]
$\eta \rightarrow \gamma ee$	7×10^{-3}	7.86	30% [Ada10a]
$\eta' \rightarrow \gamma ee$	4.7×10^{-4}	2.31	30% [Ada10a]
$\omega \rightarrow \pi^0 ee$	7.7×10^{-4}	9.87	33% [STA]
$\omega \rightarrow ee$	7.28×10^{-5}		
$\phi \rightarrow \eta ee$	1.15×10^{-4}	2.43	10% [Ada05b]
$\phi \rightarrow ee$	2.954×10^{-4}		
$J/\psi \rightarrow ee$	5.94×10^{-2}	2.33×10^{-3}	15% [Ada07]
$\psi' \rightarrow ee$	7.72×10^{-3}	3.38×10^{-4}	27% [GKS95, Sil09]
$c\bar{c} \rightarrow ee$		$\delta_{pp}^{c\bar{c}} = 0.8mb$	45% [Ada12]
$b\bar{b} \rightarrow ee$		$\delta_{pp}^{b\bar{b}} = 3.7\mu b$	30% [SMS06]
$DY \rightarrow ee$	3.36×10^{-2}	$\delta_{pp}^{c\bar{c}} = 42nb$	30% [SMS06]

these cross sections follow the number of binary (N_{bin}) scaling, so the cross sections from $p+p$ are scaled by the number of binary collisions for MB data to match with data. Fig. 4.28 shows the cocktail within STAR acceptance in Au+Au at 200GeV and different contributed sources are shown in the same plot.

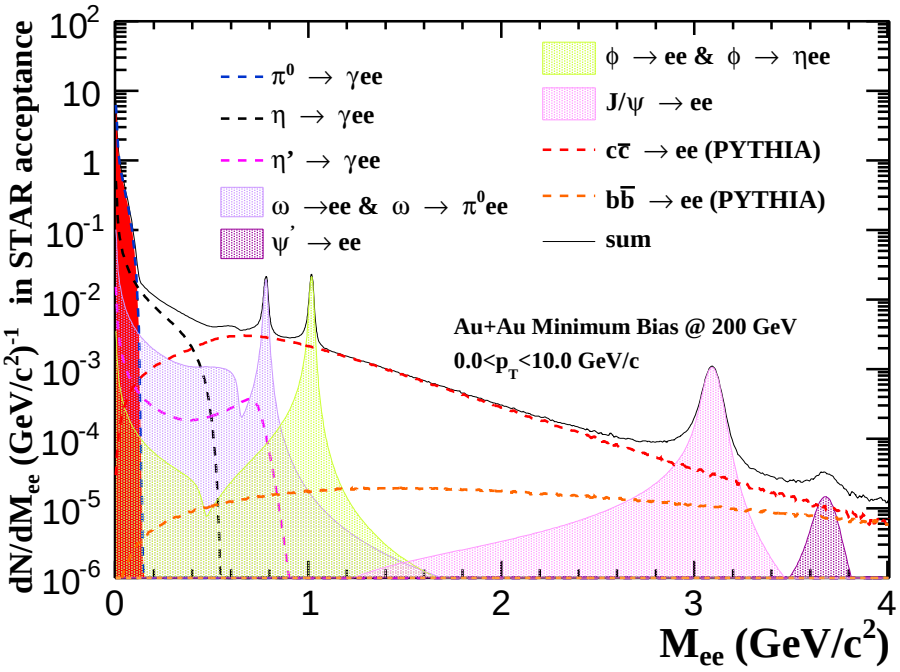

Figure 4.28: The cocktail within STAR acceptance in Au+Au at 200GeV.

4.6 Di-electron Signal

Corrected by the pair detection efficiency, the di-electron signal can be generated from the raw signal. Fig. 4.29 shows the efficiency corrected di-electron signals for Run10 and Run11 with statistical errors only. The cocktail is also shown in the same plot. Fig. 4.30 is the ratio of Run11 signals over Run10 signals. Seen from the plot, in the region with good statistics, the difference between Run10 and Run11 signals is lower than 5%. Considering the systematic uncertainty, they are consistent with each other.

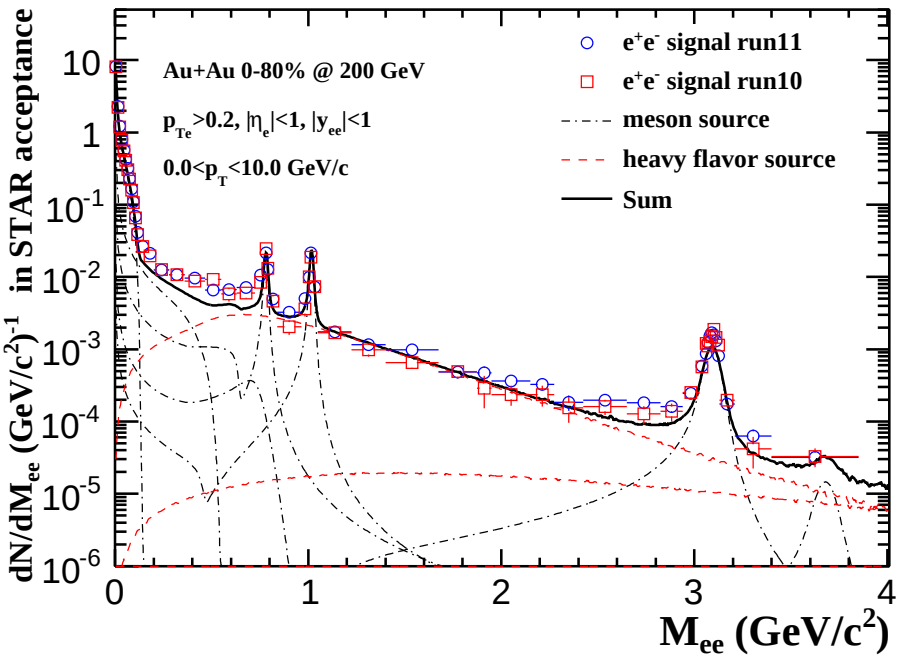

Figure 4.29: The di-electron signals from Run10 and Run11.

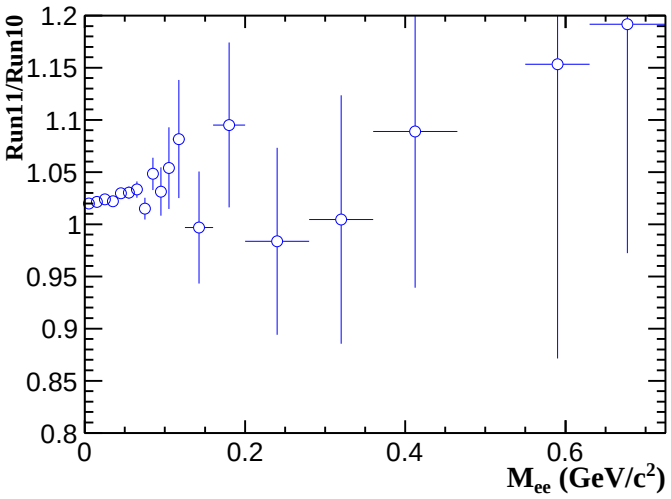

Figure 4.30: The ratio of Run11 signals over Run10 signals.

4.6.1 Run10 and Run11 combination

To combine the Run10 and Run11 di-electron continuum, they are treated as unequal precision measurements and are combined by their relative statistical errors bin by bin. The combined di-electron continuum can be found in Fig. 4.31 in different p_T slices. For the study on direct virtual photon, two methods are used to get the combined results. One is to get the results directly from the combined di-electron continuum. The other method is using the combination of Run10 and Run11 direct virtual photon results. The detail will be discussed in Sec. 4.7. Only statistical errors are shown in the plot while the systematic uncertainty will be discussed in Sec. 4.8.

4.6.2 Di-electron continuum in high p_T

The statistics for Run10 and Run11 MB data is not enough for the high p_T study. To extend this analysis to high p_T, the BEMC (Sec. 2.2.4) triggered events are used. The track quality cuts are listed in Tab. 4.5. A "TPC + TOF" track and a "TPC + EMC" track are combined as a pair which includes at least an electron track with high p_T. The data are from Run11 200GeV "NPE18" （energy threshold 4.3GeV） triggered events. The total events number is 101.16M. 38.7M out of 88.5M pass the event selection cuts after reject bad runs. This number is equal to 5389M MB data.

Fig. 4.32 shows the ee pair distribution in low mass region in different p_T slices. The efficiency for single electron which is selected by TPC+EMC is shown in the left panel in Fig. 4.33 while the right panel shows the pair detection efficiency. A efficiency corrected di-electron continuum in 4-10 GeV/c can be found in Fig. 4.34. The statistical in the low mass region is enough for the further study on direct virtual photon production.

4.7 Direct Virtual Photon Production

The behavior of low-mass excess ($M_{ee} < 0.3GeV/c$) of di-electron continuum in Au+Au collisions is shown in Fig. 4.31. A contribution from internal conversion of di-

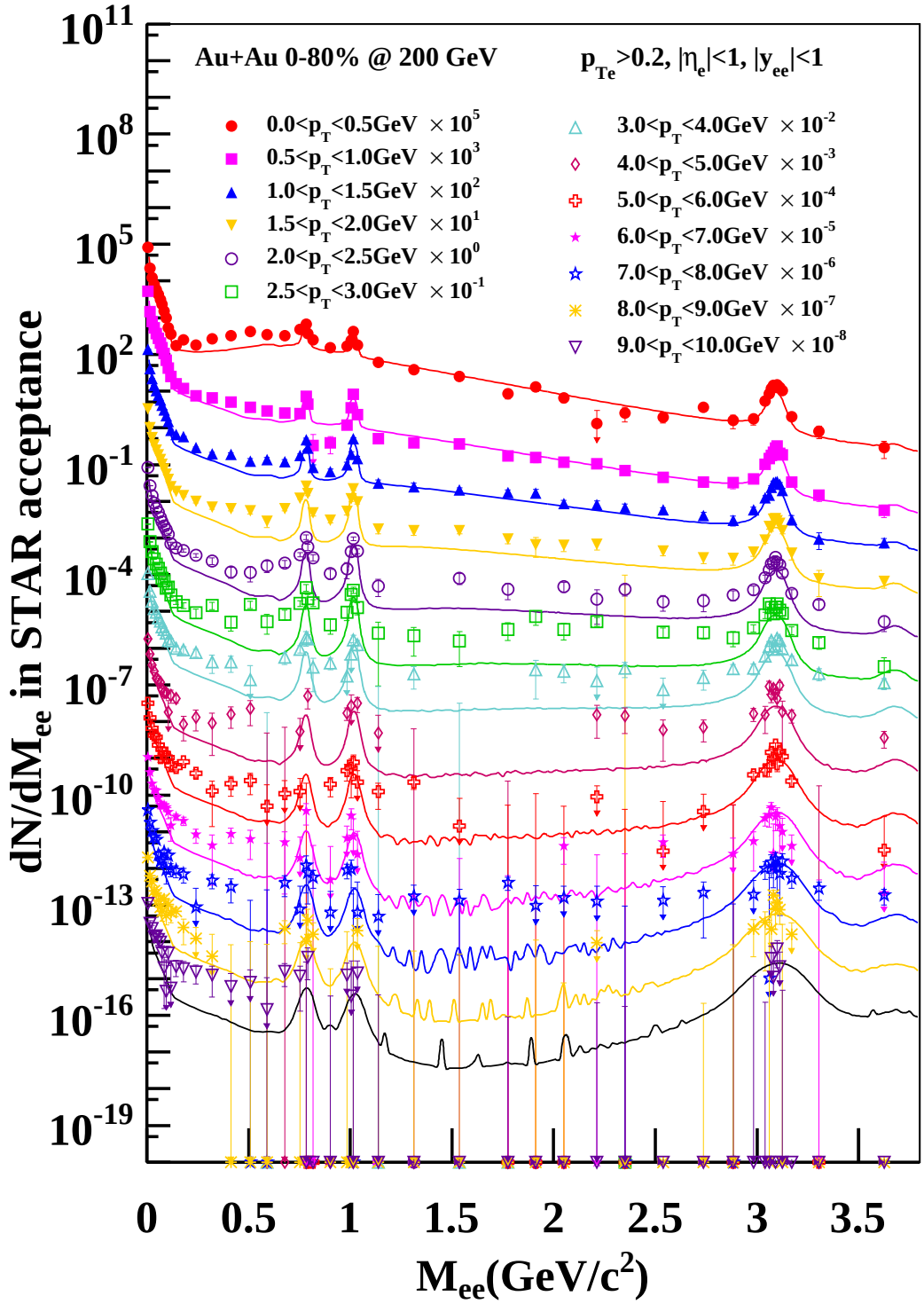

Figure 4.31: The di-electron continuum compared with cocktail. For $p_T < 5$ GeV/c, the di-electron continuums are from the combination of the Run10 and Run11 AuAu 200GeV Min.Bias data. For $5 < p_T < 10$ GeV/c, the di-electron continuums are from Run11 Au+Au 200 GeV EMC triggered data.

Table 4.5: Track quality cuts for EMC triggered data.

Item	TPC+TOF track cut	TPC+EMC track cut
p_T	$0.2 < p_T < 30GeV/c$	$p_T > 3.5GeV/c$
p	$0.2 < p < 30GeV/c$	
$\|\eta\|$	< 1	< 1
$Global\ dca$	$< 1cm$	$< 1cm$
$nHitsFit$	≥ 25	≥ 25
$nHitsDedx$	≥ 15	≥ 15
$PairY$	≤ 1	≤ 1
$\|1/\beta - 1\|$	≤ 0.03	
$n\sigma_e$	$\leq 1.6 \&\& \geq -2.7 + 1.5p$	$\leq 1.6 \&\& \geq -1.2$
p/E		$\geq 0.3 \&\& \leq 1.5$
$adc0$		> 300

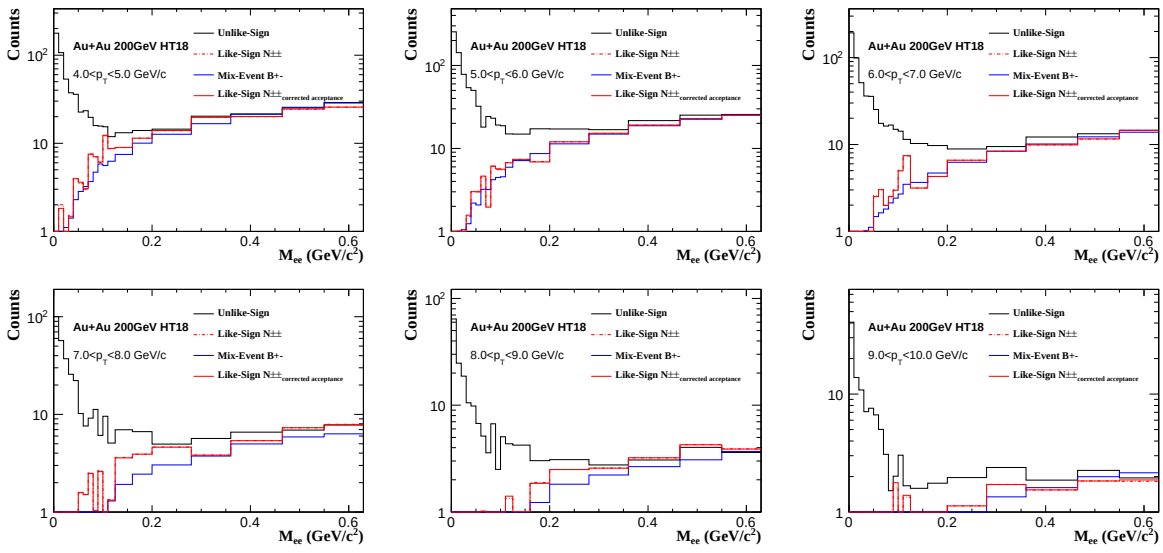

Figure 4.32: The ee pair distributions for different reconstruction methods in p_T slices.

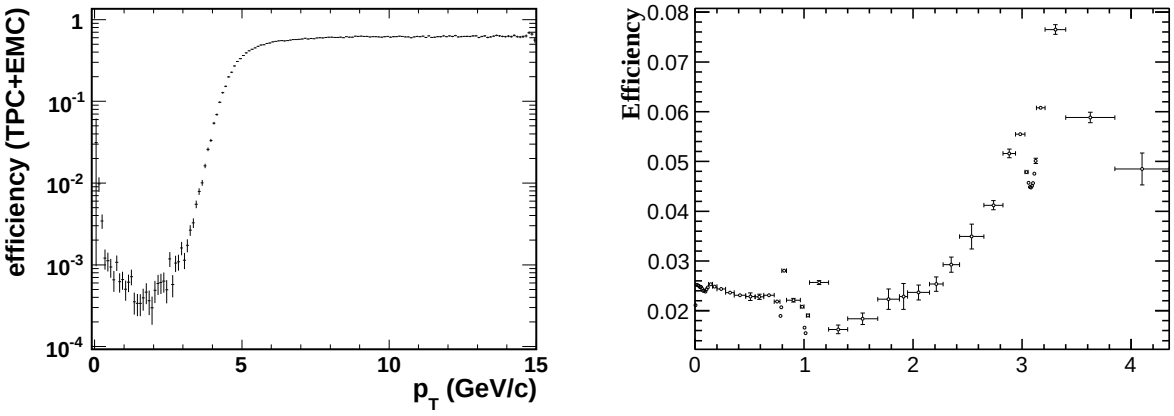

Figure 4.33: Left panel: Single electron efficiency TPC+EMC. Right panel: Pair detection efficiency in high p_T range $(5 - 10 GeV/c)$.

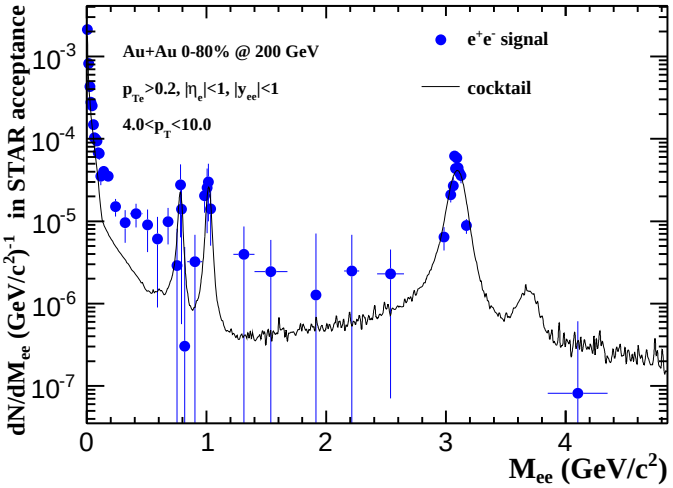

Figure 4.34: Di-electron continuum corrected for efficiency in 4-10GeV/c from Run11 200GeV EMC triggered events.

rect photons is expected. In general, any source of high energy photons will emit virtual photons which convert to low-mass e^+e^- pairs. A process which generated a high energy photon ($Q^2 = 0$) also have a analogous process with a virtual photon ($Q^2 = m_{\gamma^*}$). If $m_{\gamma^*} > 2m_e$, this virtual photon will materialize into e^+e^- pair. This e^+e^- pair production process is a QED correction to the real photon production process and is called internal conversion. In this analysis, the measurement of low-mass di-electron continuum is used to deduce the production of direct virtual photons [Ada10a, Ada10b].

4.7.1 Direct virtual photon and the associated e^+e^- pairs

The relation between virtual photon and the associated e^+e^- pair production can be described as Eq. 4.10 [Lic95, Lan85].

$$\frac{d^2N_{ee}}{dM^2} = \frac{\alpha}{3\pi}\frac{L(M)}{M^2}dN_{\gamma^*} \tag{4.10}$$

$$L(M) = \sqrt{1 - \frac{4m_e^2}{M^2}}(1 + \frac{2m_e^2}{M^2}) \tag{4.11}$$

In Eq. 4.10, M is the mass of the virtual photon or the e^+e^- pair mass ($M = m_{\gamma^*} = M_{ee}$). α is the fine structure constant ($\simeq 1/137$). This equation is the QED description on virtual photon to e^+e^- pair process based on the first order calculation in the electromagnetic coupling α. It is very similar to Eq. 4.9 as $M_h = m_{ee}$. If a factor S(M,q) can describe the difference between real photon process and virtual photon process, Eq. 4.10 can be written as Eq. 4.12. q is the three-momentum of the virtual photon. S(M,q) is a process dependent factor and be affected by such as form factors, phase space and spectral functions. As $M \to 0, q \gg M$, S(M,q) is very close to unity. In this analysis, this factor S(M,q) is assumed to 1 in the range $M_{ee} < 0.3\ GeV/c^2$, $p_T > 1\ GeV/c$. The direct photon based on this assumption is called direct virtual photon. With this assumption, Eq. 4.12 can be written as Eq. 4.13. Based on this relationship, the measurement of di-electron continuum in low-mass region will deduce the production of the direct virtual

photon.

$$\frac{d^2N_{ee}}{dM^2} = \frac{\alpha}{3\pi}\frac{L(M)}{M^2}S(M,q)dN_\gamma \tag{4.12}$$

$$\frac{d^2N_{ee}}{dM} = \frac{2\alpha}{3\pi}\frac{L(M)}{M}dN_\gamma \tag{4.13}$$

4.7.2 Excess in low-mass region

Fig. 4.31 shows the di-electron continuum compared to cocktail (Sec. 4.5) in p_T slices. The behavior of the excess is consistent with the expected contribution of the internal conversion of virtual photon. In this range, $M_{ee} \gg m_e, p_T \gg M_{ee}$ and $L(M_{ee}) \approx 1$. From Eq. 4.13, if there is real direct photon production in a given p_T bin, the corresponding e^+e^- pairs' mass distribution will follow a $1/M_{ee}$ shape in the same p_T bin. This allows the measurement on this real direct photon production via the yield of the excess.

4.7.3 Fraction of the direct virtual photon

A limit of this study is set to $0.1 < M_{ee} < 0.3GeV/c^2$, $p_T > 1GeV/c$ to meet the requirements:

1. $p_T \gg M_{ee}$ for the lowest p_T bin $1 \sim 1.5GeV/c$
2. minimize the contribution from $c\bar{c} \rightarrow ee$
3. making S(M,q) very close to unity
4. corresponding to the π^0 Dalitz decay cutoff caused by the decay kinematic

A two-components fitting is applied to this mass region. One component is the hadron cocktail came from simulation while the other is the $1/M_{ee}$ like function which stands for the contribution from internal conversion. The total function is written as Eq. 4.14.

$$f(M_{ee}, r) = (1-r)f_c(M_{ee}) + rf_{dir}(M_{ee}) \tag{4.14}$$

In this equation, r is the fraction of the direct virtual photon and stands for the ratio of *direct virtual photon / inclusive photon*. $f_c(M_{ee})$ is the cocktail shown in Fig. 4.31 normalized to very low mass region ($M_{ee} < 0.03GeV/c^2$). And $f_{dir}(M_{ee})$ is the expected $1/M_{ee}$ like shape corresponding to internal conversion filtered through STAR acceptance and normalized to the same mass region. In this mass region, $S(M_{ee})$ (corresponding to the form factor in Eq. 4.9) of π^0 Dalitz decays which is the dominate source in the cocktail is very close to 1. Thus the functional shapes of $f_c(M_{ee})$ and $f_{dir}(M_{ee})$ are essentially identical and equal to $L(M_{ee})/M_{ee}$ smeared by the detector effects. The fitting function (Eq. 4.14) in this range is independent to the only parameter r. The STAR acceptance for e^+e^- pair correspond to internal conversion is generated as a similar method discussed in Sec. 4.4.3 with PHENIX published direct photon p_T shape [Ada10b] as an input. Fig. 4.35 shows the $L(M_{ee})/M_{ee}$ shapes smeared by the STAR acceptance for virtual photon decayed e^+e^- pair in different p_T slices. The p_T dependence is obvious in low p_T range. With this acceptance correction and the normalization to $M_{ee} < 0.03GeV/c^2$, $f_{dir}(M_{ee})$ can be written as Eq. 4.15. F is the normalization factor.

$$f_{dir}(M_{ee}) = F * (\frac{L(M_{ee})}{M_{ee}})|_{STARacceptance} \tag{4.15}$$

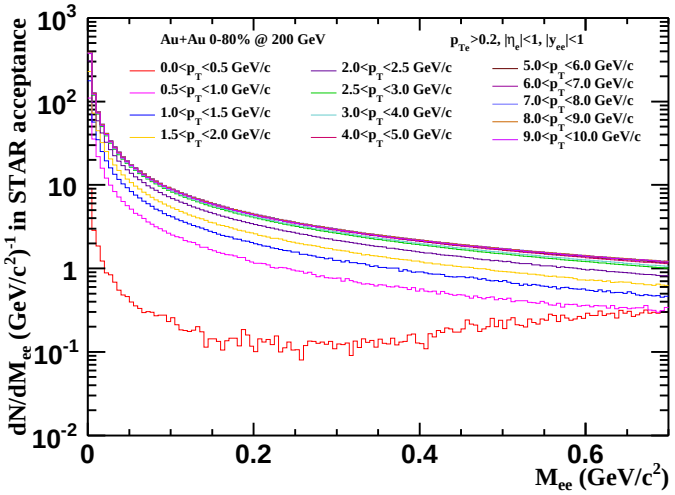

Figure 4.35: The $L(M_{ee})/M_{ee}$ shapes smeared by the STAR acceptance. The p_T dependence of STAR acceptance can be observed in low p_T.

Fig. 4.36 shows the two components ($f_c(M_{ee})$ and $f_{dir}(M_{ee})$) together with a fit result for Run10 and Run11. The error bars in the plots are the combination of the statistical errors and the systematic errors for the di-electron continuum. This systematic error will be discussed in Sec. 4.8. The dashed (black) curve at greater M_{ee} shows the fit function outside of the fit range in both figures.

For high p_T, the results from EMC triggered events can be found in Fig. 4.37. The large fitting error in 4-5 GeV/c is caused by the large systematic uncertainty in low TPC+EMC efficiency range (Fig. 4.33).

The fitting results getting from Fig. 4.36 are set as the default value for further systematic uncertainty study. Fig. 4.38 left panel shows the r value for Run10 and Run11. The p_T bin centers are shifted a bit for comparison. For the combination on Run10 and Run11 data, there are two methods to generate the combined results. The right panel of Fig. 4.38 shows the combined results. "method 1" is to generate the results by fitting the Run10 and Run11 combined di-electron continuum and get the systematic uncertainty from the combined data. In this method, the combined di-electron continuum is analyzed by the similar steps as an individual run. "method 2" is to directly combine the Run10 and Run11 fraction by their relative statistical errors and the systematic uncertainty is set as the average of Run10 and Run11. Seen from the plot, the Run10 and Run11 results are consistent with each other within errors and both combination methods give consistent results. The results from "method 1" is set as the default value for further study and discussion.

4.7.4 Direct virtual photon invariant yield

From Eq. 4.13 and Eq. 4.15, the direct virtual photon contribution used for fitting can be written as Eq. 4.16. Based on this equation, the direct virtual photon invariant yield can be calculated as Eq. 4.17. A results with mix-event background subtraction is generated for comparison.

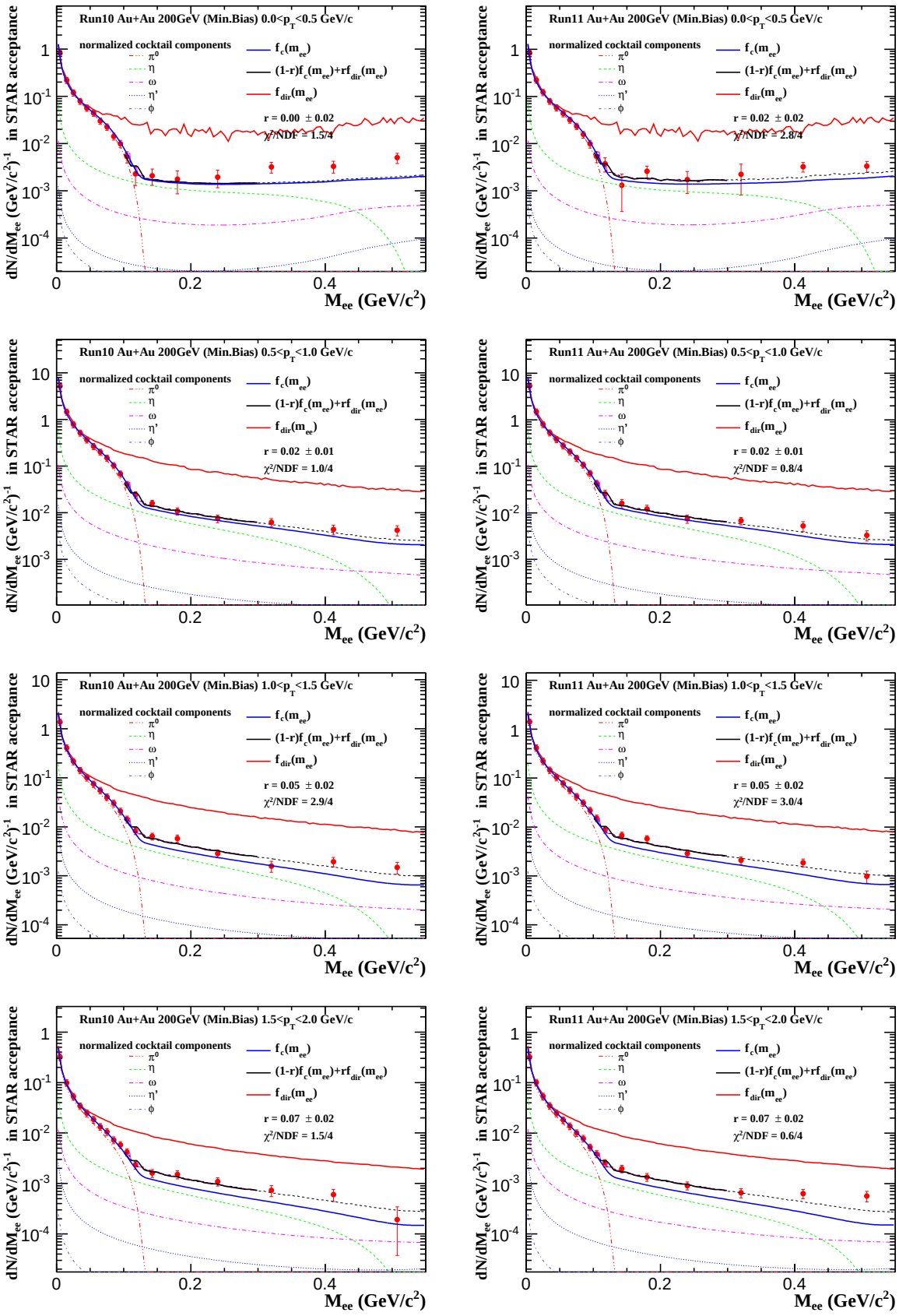
Run10 Au+Au 200GeV (Min.Bias) 0.0<p_T<0.5 GeV/c
Run11 Au+Au 200GeV (Min.Bias) 0.0<p_T<0.5 GeV/c
Run10 Au+Au 200GeV (Min.Bias) 0.5<p_T<1.0 GeV/c
Run11 Au+Au 200GeV (Min.Bias) 0.5<p_T<1.0 GeV/c
Run10 Au+Au 200GeV (Min.Bias) 1.0<p_T<1.5 GeV/c
Run11 Au+Au 200GeV (Min.Bias) 1.0<p_T<1.5 GeV/c
Run10 Au+Au 200GeV (Min.Bias) 1.5<p_T<2.0 GeV/c
Run11 Au+Au 200GeV (Min.Bias) 1.5<p_T<2.0 GeV/c
normalized cocktail components
π0
η
ω
η'
φ
f_c(m_ee)
(1-r)f_c(m_ee)+rf_dir(m_ee)
f_dir(m_ee)
r = 0.00 ± 0.02
χ²/NDF = 1.5/4
r = 0.02 ± 0.02
χ²/NDF = 2.8/4
r = 0.02 ± 0.01
χ²/NDF = 1.0/4
r = 0.02 ± 0.01
χ²/NDF = 0.8/4
r = 0.05 ± 0.02
χ²/NDF = 2.9/4
r = 0.05 ± 0.02
χ²/NDF = 3.0/4
r = 0.07 ± 0.02
χ²/NDF = 1.5/4
r = 0.07 ± 0.02
χ²/NDF = 0.6/4
dN/dM_ee (GeV/c²)⁻¹ in STAR acceptance
M_ee (GeV/c²)

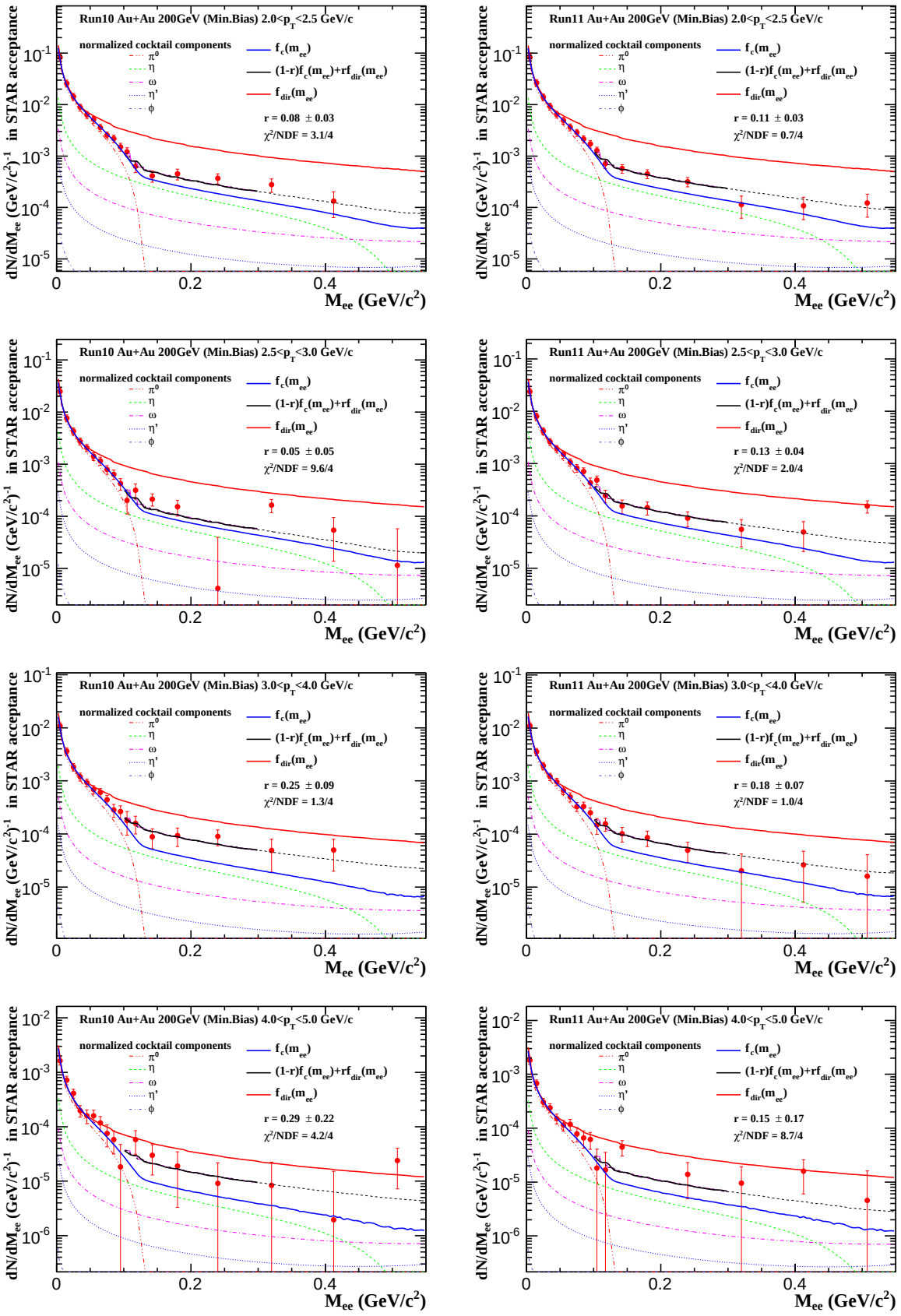

Figure 4.36: The two component function fit on Run10 and Run11 Au+Au di-electron continuum in 0.1 $< M_{ee} <$ 0.3 GeV/c^2 at 200GeV.

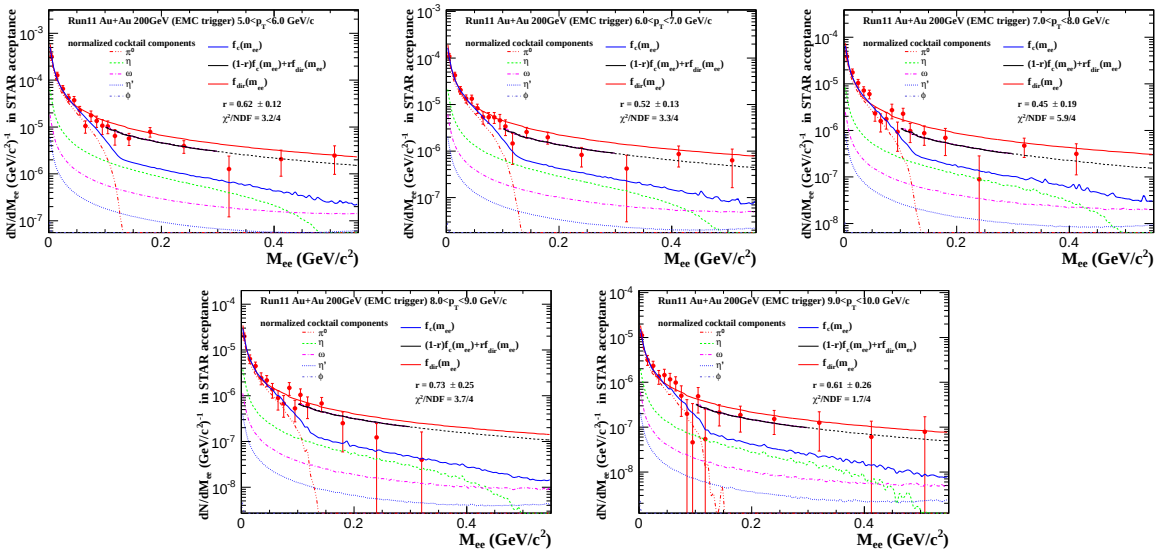

Figure 4.37: The two component function fit on Run11 Au+Au di-electron continuum in $0.1 < M_{ee} < 0.3\ GeV/c^2$ at 200GeV with EMC triggered events in high p_T. Only statistical errors are included.

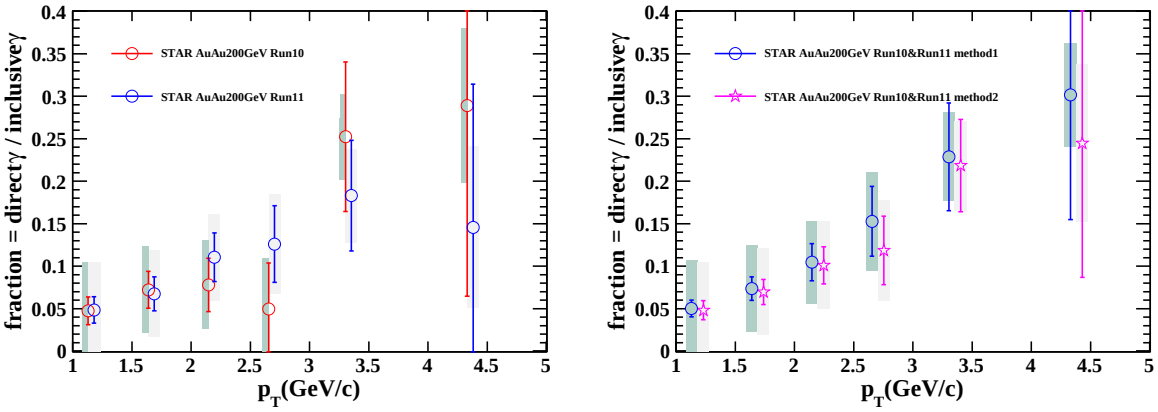

Figure 4.38: The fraction of the direct virtual photon component as a function of p_T. Left panel: results for Run10 and Run11. Right panel: results for combined di-electron continuum with different combination methods. The error bars and the error bands represent the statistical and systematic uncertainties, respectively.

$$r \times F \times (\frac{L(M)}{M}) = \frac{d^2N_{ee}}{dM} = \frac{2\alpha}{3\pi}\frac{L(M)}{M}dN_\gamma \tag{4.16}$$

$$\frac{d^2N_\gamma}{2\pi\ p_T\ dp_T\ dy} = \frac{r \times F/(\frac{2\alpha}{3\pi})}{2\pi\ p_T\ dp_T\ dy} \tag{4.17}$$

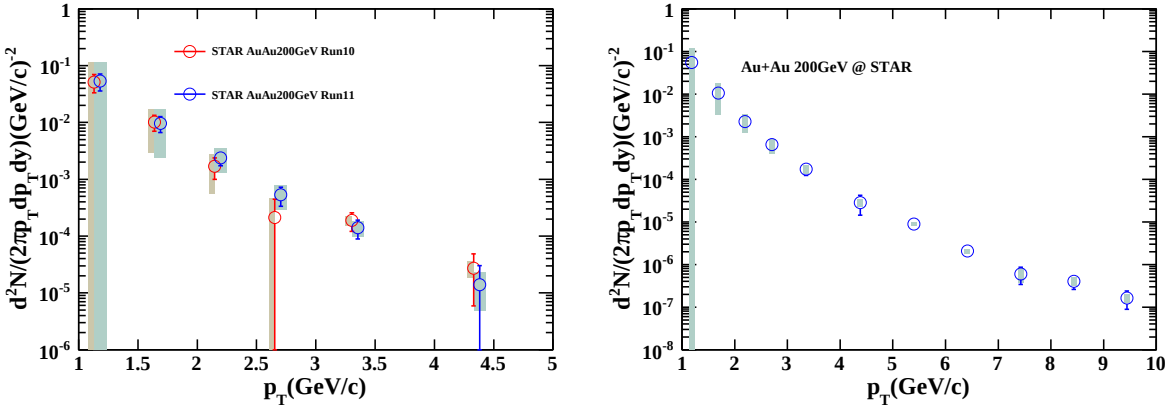

Figure 4.39: The invariant yield of direct virtual photon. Left panel: results for Run10 and Run11. Right panel: results for combined di-electron continuum and Run11 EMC triggerd events. The error bars and the error band represent the statistical and systematic uncertainties, respectively.

Fig. 4.40 shows the comparison and ratio between STAR and PHENIX results. The PHENIX data is taken from [Ada10a, Afa12], only statistical error is taken into account. The STAR result is consistent with the PHENIX measurements within errors except in $1.0 < p_T < 2.0\ GeV/c$ where the systematic uncertainty is large. This indicates the virtual photon method gives the comparable result to real photon method in high p_T range.

4.8 Systematic Uncertainty

For the analysis range is in low mass region, the systematic uncertainty is studied only in the like-sign method region ($M_{ee} < 0.7\ GeV/c$). The systematic uncertainties come from two main parts.

1. The uncertainty from di-electron continuum

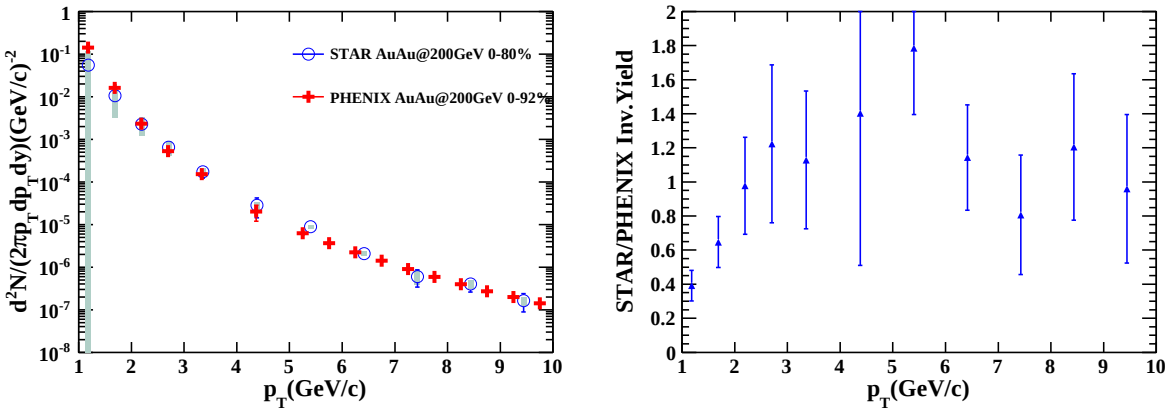

Figure 4.40: The invariant yield of direct virtual photon from STAR and PHENIX measurements. The PHENIX data is taken from [Ada10a, Afa12], only statistical error is taken into account. Left panel: invariant yield comparison. Right panel: ratio of STAR over PHENIX results. In high p_T, for STAR data in a certain p_T bin, the average of PHENIX data in the same bin is used to take the ratio.

2. The uncertainty from the fitting method

4.8.1 Uncertainty from di-electron continuum

The following bullets show the contributed sources for the uncertainty from di-electron continuum.

1. ϕ_V cut uncertainty
2. Uncertainty from the acceptance correction for like-sign pair
3. Detection efficiency and acceptance uncertainty

For ϕ_V cut uncertainty calculation, another ϕ_V cut with different shape is applied to the analysis. The final efficiency corrected di-electron continuum with this ϕ_V cut is generated with the same steps as mentioned. The difference between this di-electron continuum and the previous default value is set as the uncertainty came from the ϕ_V cut.

For the uncertainty from acceptance correction between unlike-sign and like-sign electron pairs, considering the source of this uncertainty, the acceptance factor (Eq. 4.4) difference between full magnetic field (FF) and reversed full magnetic field (RFF) is considered as the main contributed source. The relative uncertainty from this source can

be calculated by taking the ratio of the relative acceptance factor uncertainty over the like-sign signal over background ratio. Fig. 4.41 shows the relative uncertainties from different sources for di-electron continuum in a p_T slice. These uncertainties are generated and involved for different p_T slices and point by point, respectively.

The uncertainty of the pair detection efficiency is a overall value without p_T and mass dependence. It will not significantly impact to the fraction mean value but just the fitting error. This uncertainty is set to 15% based on the relative di-electron study for Au+Au 200GeV MB data at STAR. The di-electron continuum with systematic uncertainty is shown in Fig. 5.3. Seen from Fig. 5.4, comparing the results from the di-electron continuum with only statistical errors ($SET1$) on left panels and with statistical and systematic combined errors ($SET2$) on right panels, the fraction mean values from both error sets do not show significant changing and the fitting errors for $SET2$ are larger. For the fraction generation, $SET2$ is set as the default errors for the data points. With this setting, the systematic uncertainty from di-electron continuum is contained in the fraction fitting errors.

For high p_T EMC triggered data, since the acceptance correction is very close to unity, only the uncertainty from ϕ_V cut and efficiency correction is considered. The uncertainties from normalization process to MB data and EMC efficiency are still ongoing.

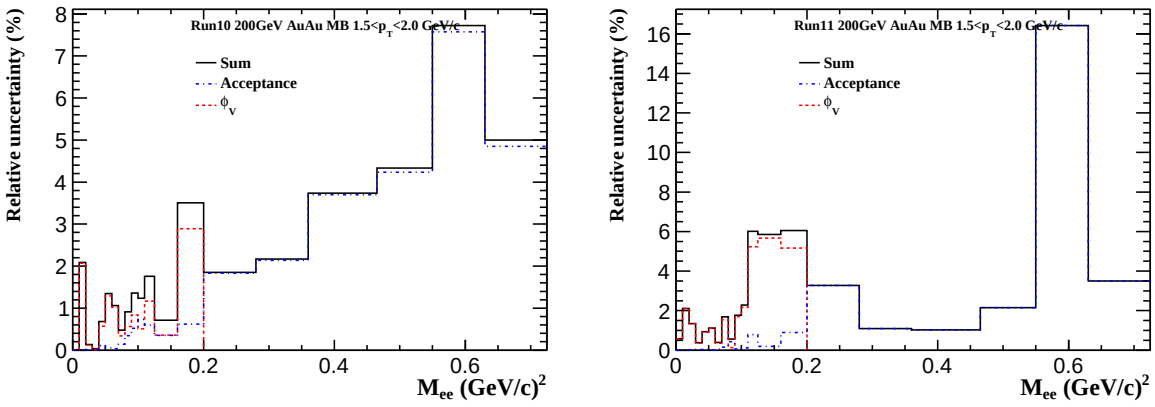

Figure 4.41: The relative uncertainties from different sources for di-electron continuum in $1.5 < p_T < 2\ GeV/c$.

4.8.2 Uncertainty from the fitting method

Two sources are considered as the main uncertainty contribution sources from the fitting method. One is the uncertainty of the cocktail and the other is the uncertainty caused by the fitting range.

4.8.2.1 Uncertainty from fitting range

To get the uncertainty from the fitting range, the results from fitting range $0.08 < M_{ee} < 0.3\ GeV/c^2$ and $0.12 < M_{ee} < 0.3\ GeV/c^2$ are generated. The maximum difference between both results and the default value which is with the fitting range $0.1 < M_{ee} < 0.3\ GeV/c^2$ is set as the uncertainty from fitting range. The relative uncertainty from this source can be found in Fig. 4.43.

4.8.2.2 Uncertainty from cocktail

As the cocktail is used for the two components fitting, its uncertainty especially the π^0 and η sources will impact the fraction and yield significantly. The excess will increase with increased π^0 and decreased η contribution. From Tab. 4.4, the uncertainty of rapidity density dN/dy for π^0 and η is 8% and 30%, respectively. As mentioned in Sec. 4.5.1, a TBW model fitting to published data is used as the input p_T shape. For η source, since there is no low p_T measurements, the p_T shape in low p_T range for η is only the model prediction. Another prediction is the m_T scaling p_T shape [Ada10a]. A Hagedorn function given by Eq. 4.18 is modified by fitting the π^0 yield. For other mesons, p_T in Eq. 4.18 is replaced by $\sqrt{m^2 - m_\pi^2 + (p_T/c)^2}$, where m is the meson mass.

$$E\frac{d^3\delta}{dp^3} = A(e^{-(ap_T+bp_T^2)} + p_T/p_0)^{-n} \tag{4.18}$$

Fig. 4.42 shows the difference between TBW and m_T scaling p_T shape for η. There is big difference in low p_T and this is the main contribution for the 30% difference compared with PHENIX data. Also the invariant yield measurements for η have the uncertainty on

the same level. Three p_T and dN/dy input sets below are used to modify this uncertainty contribution.

m_T scaling p_T input, π^0 dN/dy - 8%, η dN/dy + 30%

TBW p_T input, π^0 dN/dy - 8%, η dN/dy + 30%

TBW p_T input, π^0 dN/dy + 8%, η dN/dy - 30%

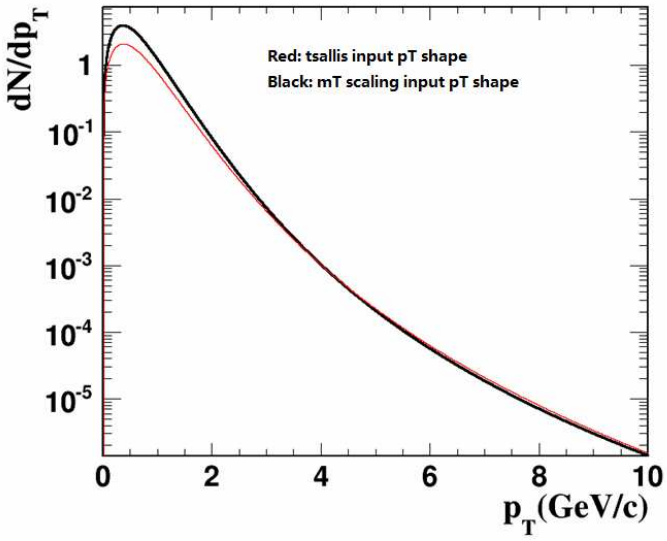

Figure 4.42: The input p_T shapes from TBW model and a m_T scaling prediction for η source in cocktail simulation.

The maximum relative uncertainty which is the maximum relative difference between the results from this set and the default value is set as the uncertainty from p_T and dN/dy input. Seen from Fig. 4.43, this uncertainty has p_T dependence which is consistent with the difference shown in Fig. 4.42. The overall relative uncertainty and its contributed sources are shown in the same plot. The fraction and invariant yield with systematic uncertainty can be found in Fig. 4.38 and Fig. 4.39, respectively.

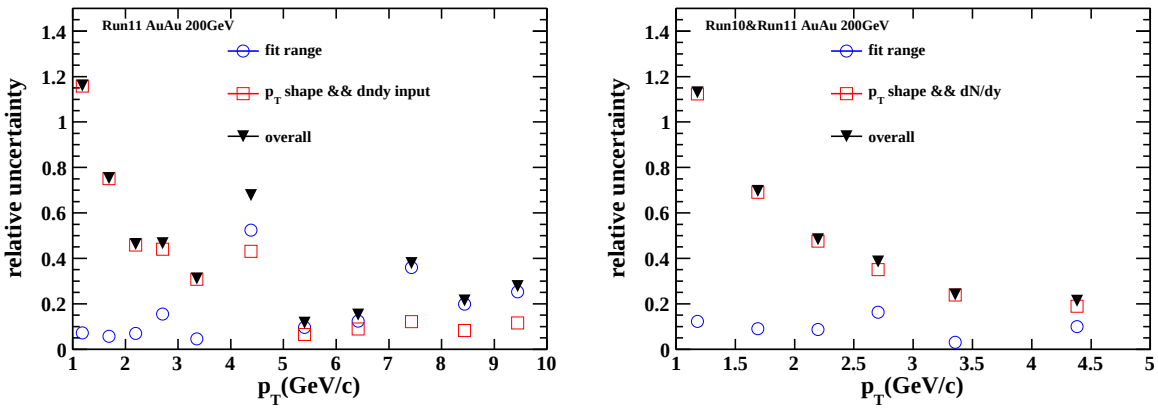

Figure 4.43: The relative uncertainty and its contributed sources with Run10 and Run11 Au+Au 200GeV data. Left panel: Run11 data. Right panel: Run10 and Run11 combined data.

CHAPTER 5

Results and Discussion

The di-electron continuums for both Run10 and Run11 Au+Au 200GeV Min.Bias data are generated in $0 < p_T < 5\ GeV/c$ while the EMC triggered events extend the range to $5 < p_T < 10\ GeV/c$. Like-sign background with acceptance correction is subtracted to obtain to low mass continuum ($M_{ee} < 0.7\ GeV/c^2$) while mixed-event background is used for the mass range above. A combined results are generated from Run10 and Run11 results. The continuums for different p_T slices will also be discussed in this chapter. Based on the p_T differential continuum, the direct virtual photon production is done to this data set. A two-components fitting is applied to the low mass continuum to get the fraction of direct virtual photon which stands for the ratio of direct virtual photon versus inclusive photon. The yield of direct virtual photon is extracted accordingly. The comparison to model prediction will be discussed.

5.1 Di-electron Continuum

After efficiency correction, the Run10, Run11 and their combined invariant mass spectrums of di-electron within STAR acceptance compared to cocktail in Au+Au collisions at 200 GeV are obtained. Fig. 5.1 is the Run10 and Run11 signals compared to cocktail with different contributions. Fig. 5.2 shows the p_T dependence results from Run10 and Run11 while Fig. 5.3 shows the combined results with Run11 EMC triggered high p_T ($> 5\ GeV/c$) measurements.

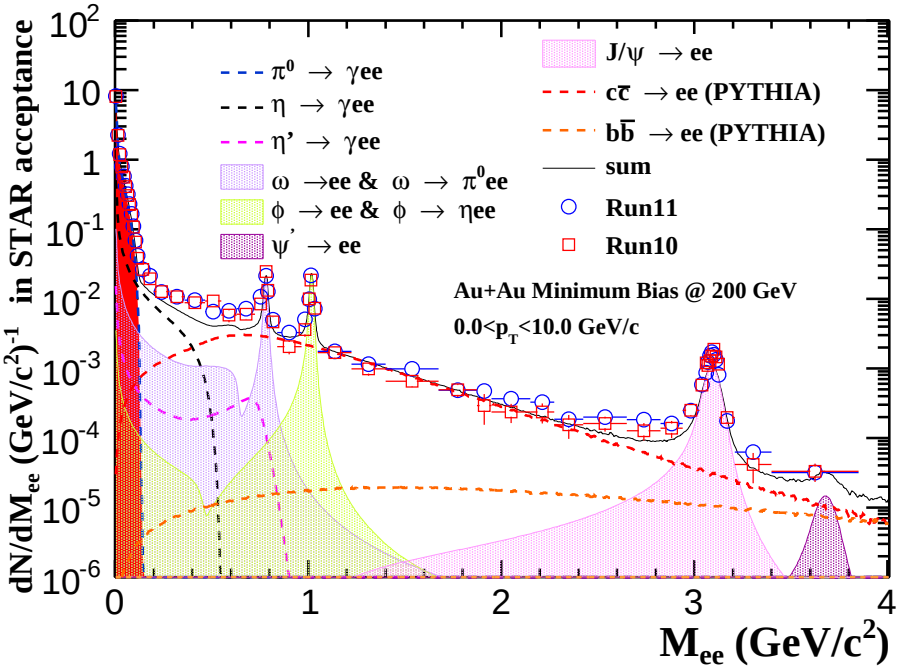

Figure 5.1: The di-electron continuum from Run10 and Run11 compared to cocktail with different contributions.

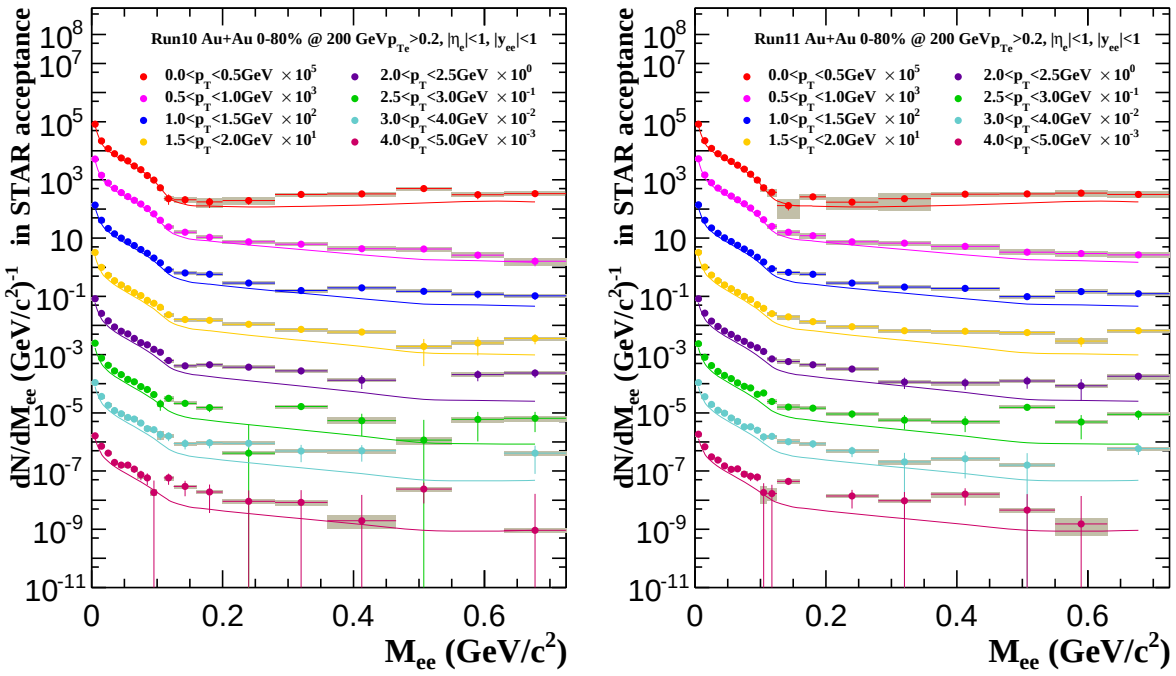

Figure 5.2: The Run10 and Run11 di-electron continuum with systematic uncertainties compared with cocktail at low mass in p_T slices. Left panel: Run10. Right panel: Run11。

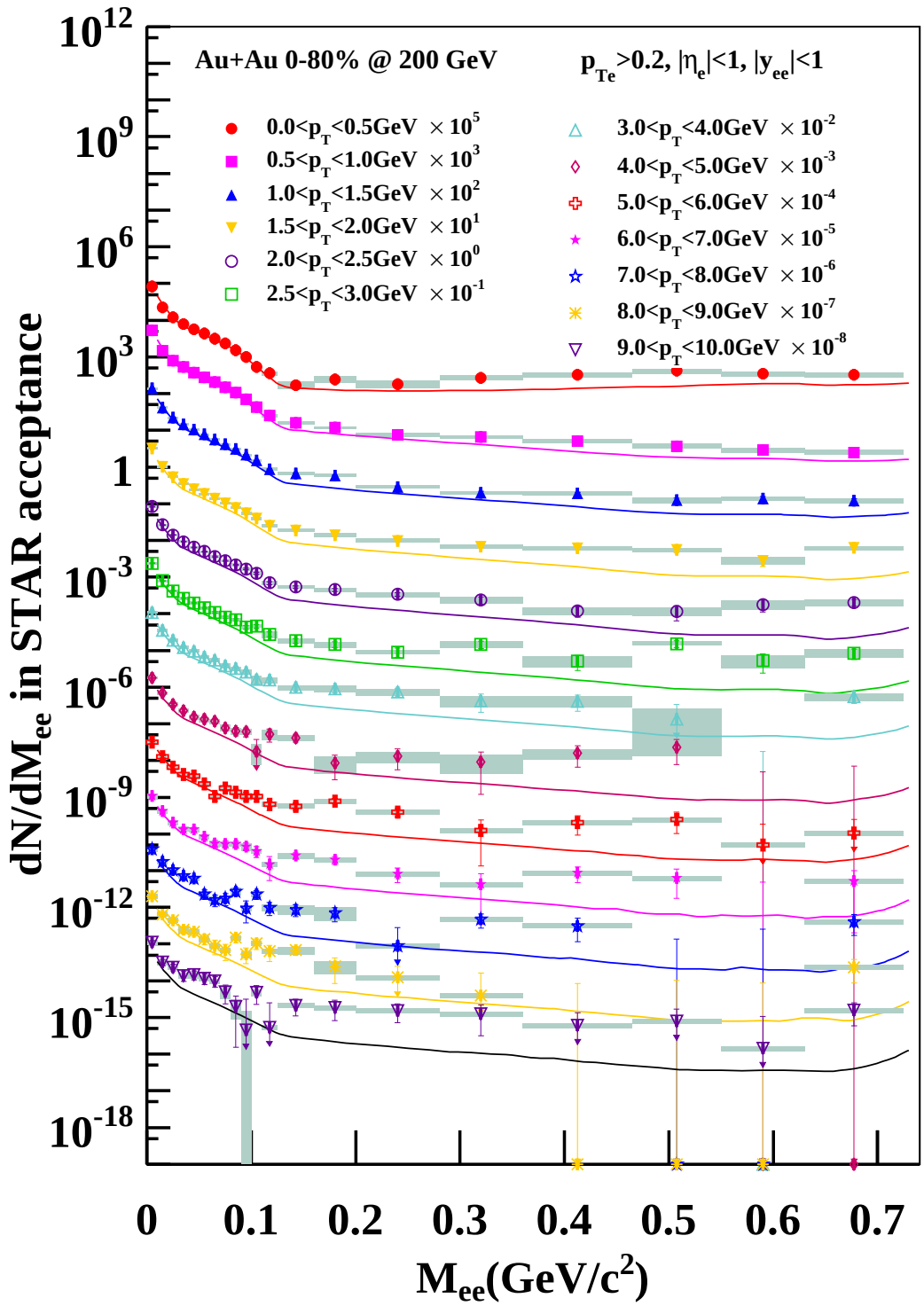

Figure 5.3: The combined di-electron continuum with systematic uncertainties compared with cocktail at low mass in p_T slices. The results in $p_T > 5\ GeV/c$ is from Run11 EMC triggered events。

Table 5.1: The two component function fitting parameters.

p_T GeV/c	Run10 $r \times 10$	Run11 $r \times 10$	Run10 $\oplus$ Run11 (*stat.* only) $r \times 10$	Run10 $\oplus$ Run11 $r \times 10$
0.0-0.5	0.0 ± 0.2	0.2 ± 0.2	0.2 ± 0.1	0.2 ± 0.1
0.5-1.0	0.2 ± 0.1	0.2 ± 0.1	0.2 ± 0.0	0.2 ± 0.1
1.0-1.5	0.5 ± 0.2	0.5 ± 0.2	0.6 ± 0.0	0.5 ± 0.1
1.5-2.0	0.7 ± 0.2	0.7 ± 0.2	0.8 ± 0.1	0.7 ± 0.1
2.0-2.5	0.8 ± 0.3	1.1 ± 0.3	1.2 ± 0.1	1.0 ± 0.2
2.5-3.0	0.5 ± 0.5	1.3 ± 0.4	1.8 ± 0.3	1.5 ± 0.4
3.0-4.0	2.5 ± 0.9	1.8 ± 0.7	2.5 ± 0.5	2.3 ± 0.6
4.0-5.0	2.9 ± 2.2	1.5 ± 1.7	3.3 ± 1.2	3.0 ± 1.5
5.0-6.0		6.2 ± 1.2		
6.0-7.0		5.2 ± 1.3		
7.0-8.0		4.5 ± 1.9		
8.0-9.0		7.3 ± 2.5		
9.0-10.0		6.1 ± 2.6		

5.2 Direct Virtual Photon

5.2.1 Direct virtual photon fraction

Due to the method discussed in Sec. 4.7, a two-components fitting is applied to the di-electron continuum in the range $0.1 < M_{ee} < 0.3\ GeV/c^2$. The comparison between the fitting on combined di-electron continuum with statistical errors only and with the quadrature sum of statistical and systematic errors is shown in Fig. 5.4. For the EMC triggered events for Run11 Au+Au collisions at 200 GeV, the fitting plots can be found in Fig. 5.5.

Fig. 5.6 shows the ratio of di-electron continuum over the total fit function and the ratio of di-electron continuum over the normalized cocktail in different p_T slices. In the range with good statistics, the ratio of di-electron continuum over the total fit function is consistent with 1 within in errors.

Tab. 5.1 lists all the fitting parameters for Fig. 4.36, Fig. 5.4 and Fig. 5.5.

The fraction for direct virtual photon which stands for the ratio of direct virtual photon versus inclusive photon is obtained from the two-components fitting. Fig. 5.7 shows the

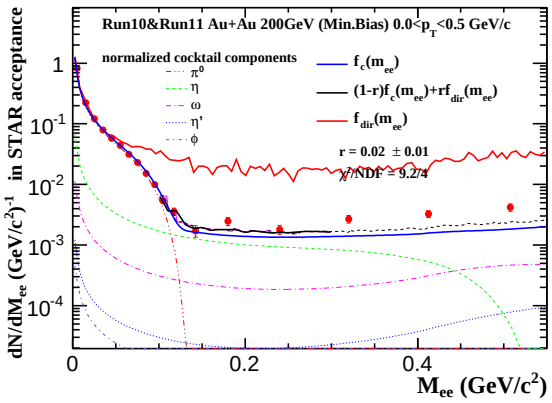
Run10&Run11 Au+Au 200GeV (Min.Bias) 0.0<p_T<0.5 GeV/c
normalized cocktail components
π0
η
ω
η'
φ
f_c(m_ee)
(1-r)f_c(m_ee)+rf_dir(m_ee)
f_dir(m_ee)
r = 0.02 ± 0.01
χ²/NDF = 9.2/4
dN/dM_ee (GeV/c²)⁻¹ in STAR acceptance
M_ee (GeV/c²)

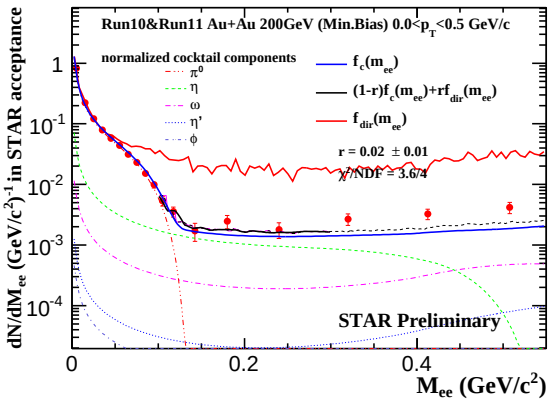
Run10&Run11 Au+Au 200GeV (Min.Bias) 0.0<p_T<0.5 GeV/c
normalized cocktail components
π0
η
ω
η'
φ
f_c(m_ee)
(1-r)f_c(m_ee)+rf_dir(m_ee)
f_dir(m_ee)
r = 0.02 ± 0.01
χ²/NDF = 3.6/4
STAR Preliminary
dN/dM_ee (GeV/c²)⁻¹ in STAR acceptance
M_ee (GeV/c²)

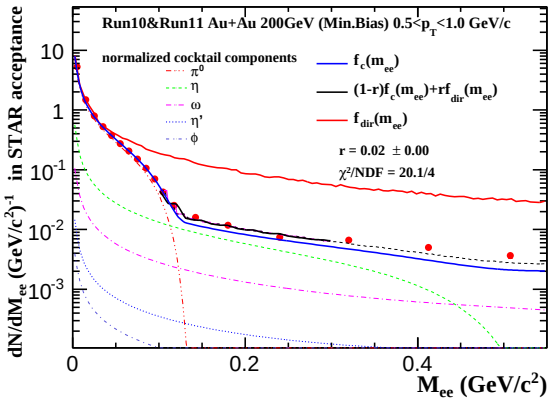
Run10&Run11 Au+Au 200GeV (Min.Bias) 0.5<p_T<1.0 GeV/c
normalized cocktail components
π0
η
ω
η'
φ
f_c(m_ee)
(1-r)f_c(m_ee)+rf_dir(m_ee)
f_dir(m_ee)
r = 0.02 ± 0.00
χ²/NDF = 20.1/4
dN/dM_ee (GeV/c²)⁻¹ in STAR acceptance
M_ee (GeV/c²)

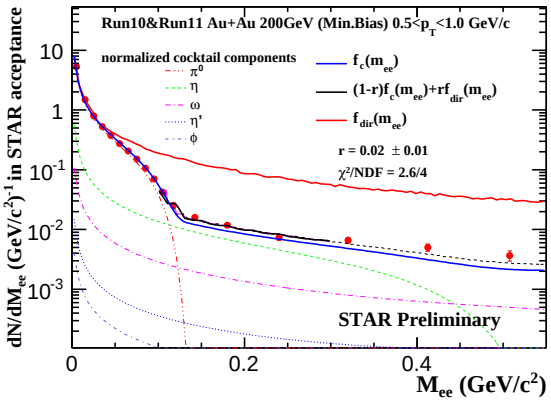
Run10&Run11 Au+Au 200GeV (Min.Bias) 0.5<p_T<1.0 GeV/c
normalized cocktail components
π0
η
ω
η'
φ
f_c(m_ee)
(1-r)f_c(m_ee)+rf_dir(m_ee)
f_dir(m_ee)
r = 0.02 ± 0.01
χ²/NDF = 2.6/4
STAR Preliminary
dN/dM_ee (GeV/c²)⁻¹ in STAR acceptance
M_ee (GeV/c²)

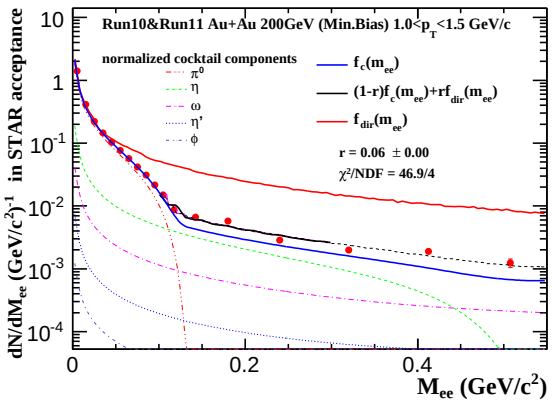
Run10&Run11 Au+Au 200GeV (Min.Bias) 1.0<p_T<1.5 GeV/c
normalized cocktail components
π0
η
ω
η'
φ
f_c(m_ee)
(1-r)f_c(m_ee)+rf_dir(m_ee)
f_dir(m_ee)
r = 0.06 ± 0.00
χ²/NDF = 46.9/4
dN/dM_ee (GeV/c²)⁻¹ in STAR acceptance
M_ee (GeV/c²)

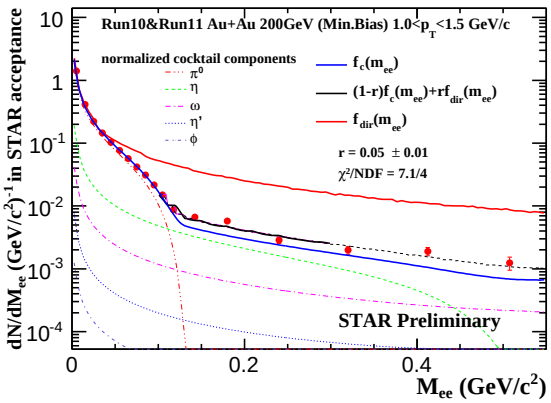
Run10&Run11 Au+Au 200GeV (Min.Bias) 1.0<p_T<1.5 GeV/c
normalized cocktail components
π0
η
ω
η'
φ
f_c(m_ee)
(1-r)f_c(m_ee)+rf_dir(m_ee)
f_dir(m_ee)
r = 0.05 ± 0.01
χ²/NDF = 7.1/4
STAR Preliminary
dN/dM_ee (GeV/c²)⁻¹ in STAR acceptance
M_ee (GeV/c²)

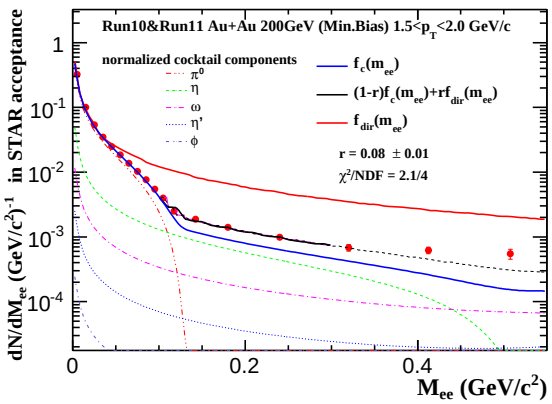
Run10&Run11 Au+Au 200GeV (Min.Bias) 1.5<p_T<2.0 GeV/c
normalized cocktail components
π0
η
ω
η'
φ
f_c(m_ee)
(1-r)f_c(m_ee)+rf_dir(m_ee)
f_dir(m_ee)
r = 0.08 ± 0.01
χ²/NDF = 2.1/4
dN/dM_ee (GeV/c²)⁻¹ in STAR acceptance
M_ee (GeV/c²)

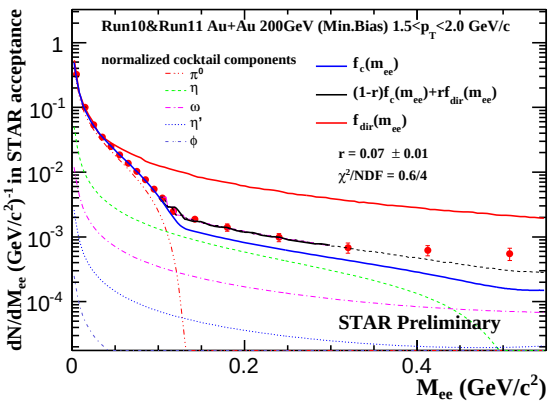
Run10&Run11 Au+Au 200GeV (Min.Bias) 1.5<p_T<2.0 GeV/c
normalized cocktail components
π0
η
ω
η'
φ
f_c(m_ee)
(1-r)f_c(m_ee)+rf_dir(m_ee)
f_dir(m_ee)
r = 0.07 ± 0.01
χ²/NDF = 0.6/4
STAR Preliminary
dN/dM_ee (GeV/c²)⁻¹ in STAR acceptance
M_ee (GeV/c²)

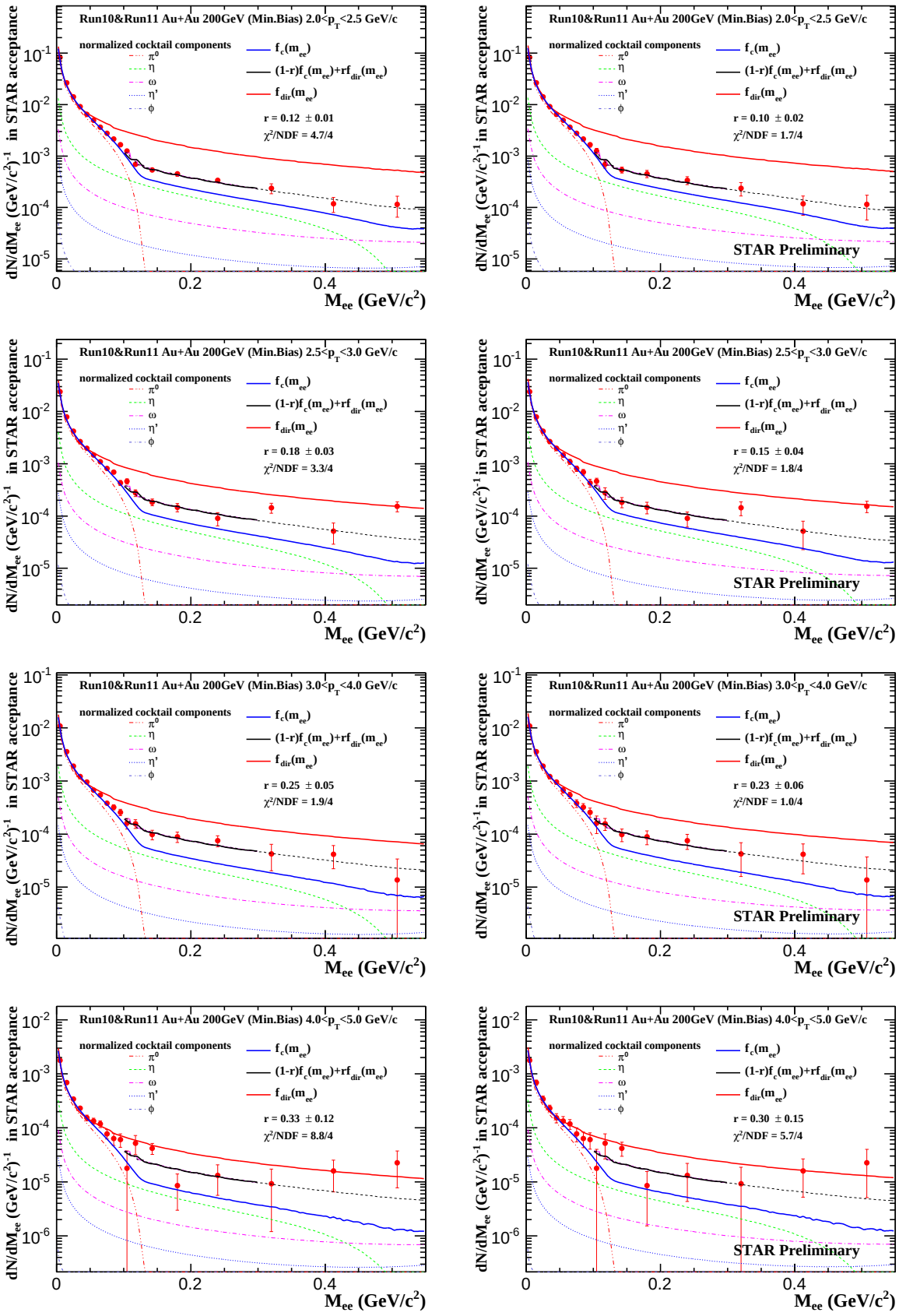

Figure 5.4: The two component function fit on Run10 and Run11 combined Au+Au di-electron continuum in $0.1 < M_{ee} < 0.3\ GeV/c^2$ at 200GeV. Left panels: w/ statistical errors only. Right panels: w/ errors setting as the quadrature sum of statistical and systematic errors.

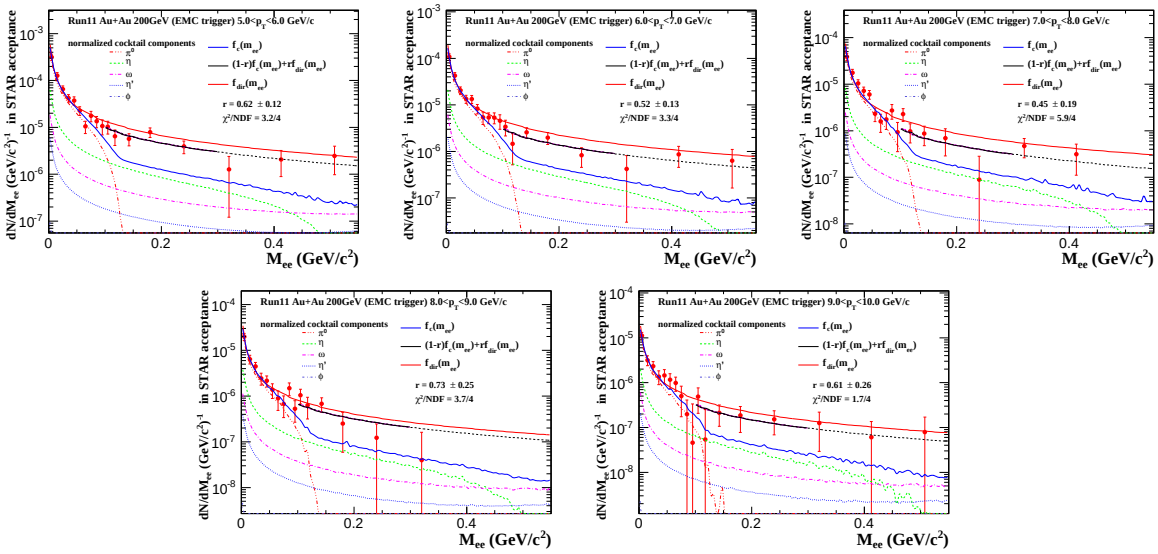

Figure 5.5: The two component function fit on Run11 Au+Au di-electron continuum in $0.1 < M_{ee} < 0.3\ GeV/c^2$ at 200GeV with EMC triggered events in high p_T. The errors shown are the quadrature sum of statistical and systematic errors.

fraction compared with the next-to-leading-order perturbative QCD (NLO pQCD) calculation [GV93]. PHENIX result shows the consistence on the $p+p$ results to this model prediction while the fraction in Au+Au is larger than the calculation for $p_T < 3.5\ GeV/c$ which is shown in Fig. 1.6. The results from STAR shows the larger fraction to the NLO pQCD prediction for $p_T < 4.0\ GeV/c$ while the results in $1.0 < p_T < 2.0\ GeV/c$ are with big systematic uncertainties which are mainly caused by the η contributed uncertainty.

As mentioned in Sec. 1.4.2.1, PHENIX collaboration gave a measurement in $p_T < 5.0\ GeV/c$ with the same virtual photon method. Fig. 5.8 shows a comparison between STAR measurements and PHENIX published data. The statistical and systematic uncertainties are shown by the bars and bands, respectively. The biggest difference comes from $1.0 < p_T < 2.0\ GeV/c$. In this p_T range, both input η p_T shape and rapidity density are from estimation. As mentioned before, a extension of η measurement in this range will help to reduce the uncertainty a lot.

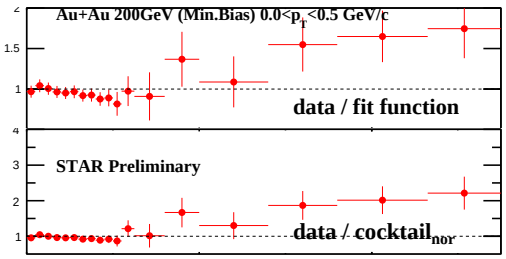
Au+Au 200GeV (Min.Bias) 0.0<p_T<0.5 GeV/c
data / fit function
STAR Preliminary
data / cocktail_nor

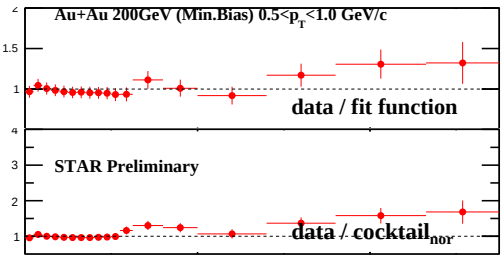
Au+Au 200GeV (Min.Bias) 0.5<p_T<1.0 GeV/c
data / fit function
STAR Preliminary
data / cocktail_nor

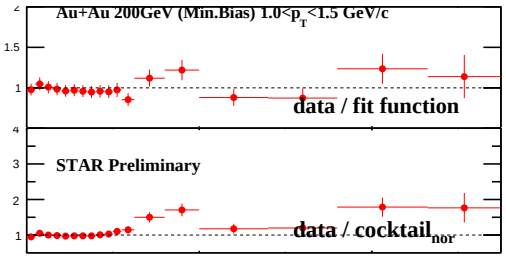
Au+Au 200GeV (Min.Bias) 1.0<p_T<1.5 GeV/c
data / fit function
STAR Preliminary
data / cocktail_nor

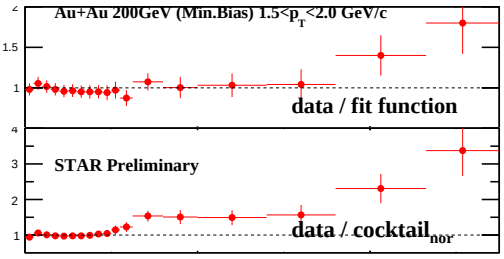
Au+Au 200GeV (Min.Bias) 1.5<p_T<2.0 GeV/c
data / fit function
STAR Preliminary
data / cocktail_nor

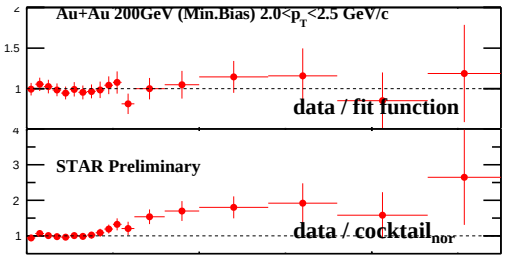
Au+Au 200GeV (Min.Bias) 2.0<p_T<2.5 GeV/c
data / fit function
STAR Preliminary
data / cocktail_nor

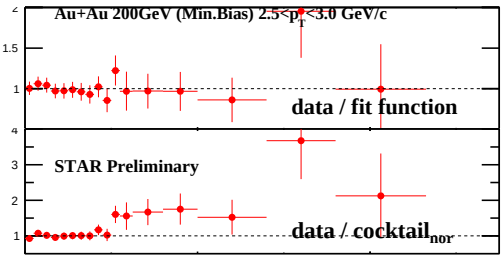
Au+Au 200GeV (Min.Bias) 2.5<p_T<3.0 GeV/c
data / fit function
STAR Preliminary
data / cocktail_nor

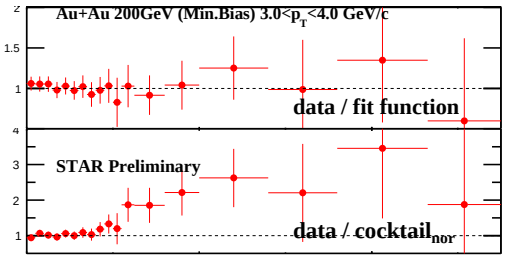
Au+Au 200GeV (Min.Bias) 3.0<p_T<4.0 GeV/c
data / fit function
STAR Preliminary
data / cocktail_nor

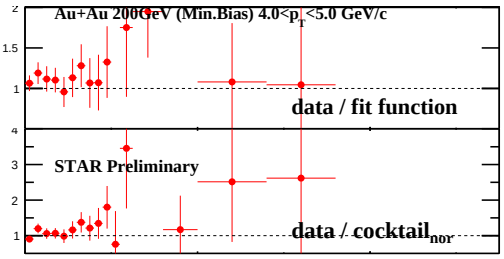
Au+Au 200GeV (Min.Bias) 4.0<p_T<5.0 GeV/c
data / fit function
STAR Preliminary
data / cocktail_nor

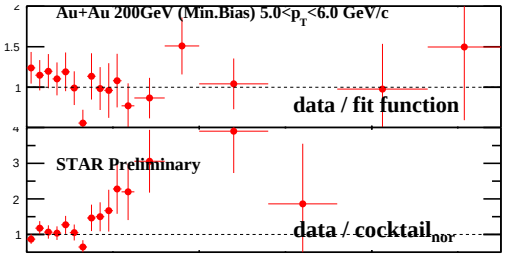
Au+Au 200GeV (Min.Bias) 5.0<p_T<6.0 GeV/c
data / fit function
STAR Preliminary
data / cocktail_nor

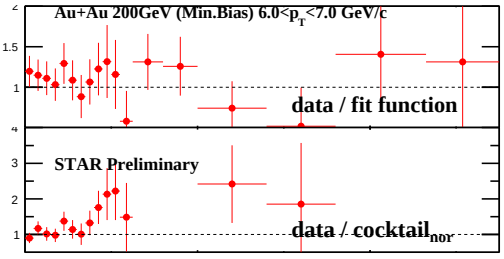
Au+Au 200GeV (Min.Bias) 6.0<p_T<7.0 GeV/c
data / fit function
STAR Preliminary
data / cocktail_nor

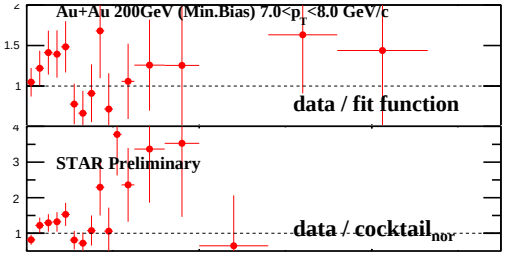
Au+Au 200GeV (Min.Bias) 7.0<p_T<8.0 GeV/c
data / fit function
STAR Preliminary
data / cocktail_nor

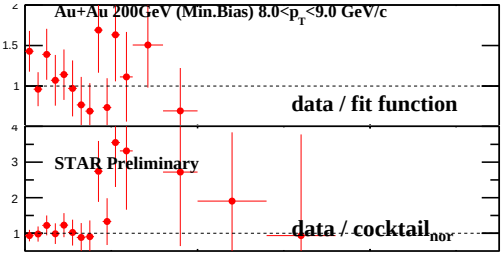
Au+Au 200GeV (Min.Bias) 8.0<p_T<9.0 GeV/c
data / fit function
STAR Preliminary
data / cocktail_nor

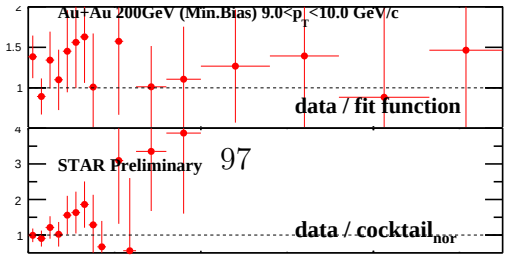
Au+Au 200GeV (Min.Bias) 9.0<p_T<10.0 GeV/c
data / fit function
STAR Preliminary
data / cocktail_nor

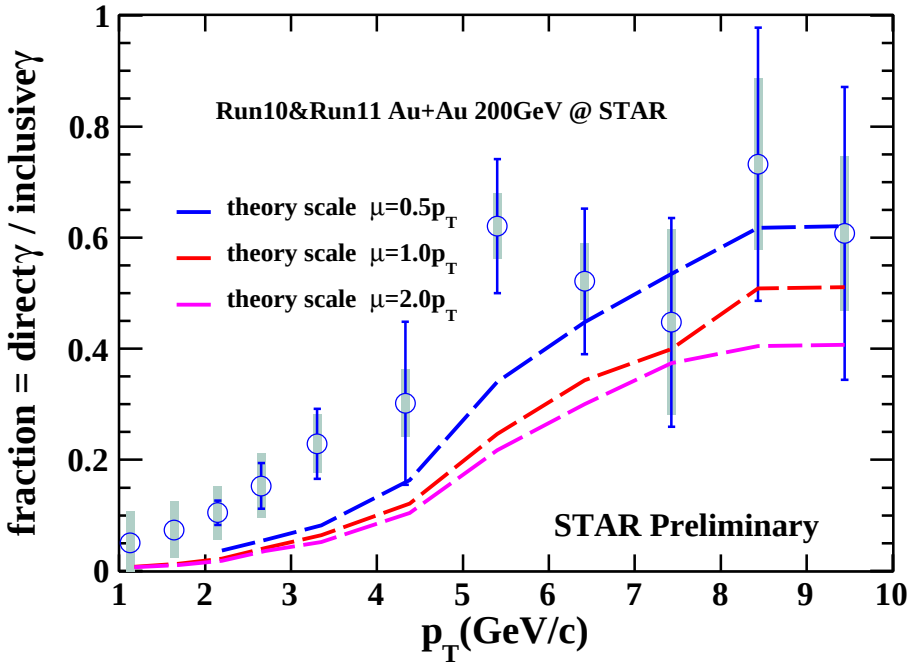

Figure 5.7: The fraction of direct photon compared with the NLO pQCD prediction. The curves represent $T_{AA}d\sigma_{\gamma}^{NLO}(p_T)/dN_{\gamma}^{inclusive}(p_T)$, showing the scale dependence of the theory [GV93]。

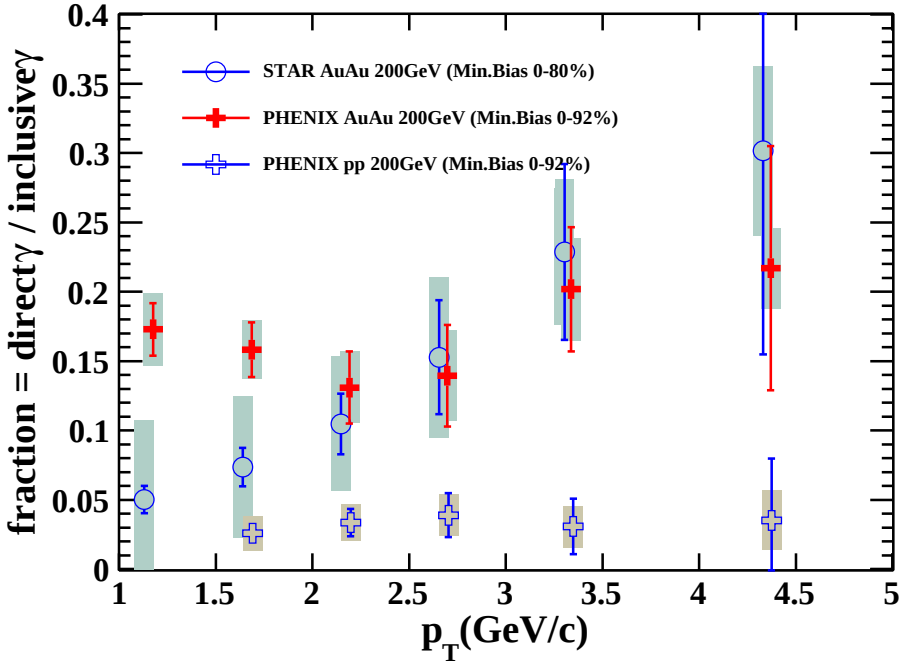

Figure 5.8: The fraction of direct photon compared to PHENIX measurement. The PHENIX published data is from [Ada10b]。

5.2.2 Direct virtual photon invariant yield

By treating the excess as internal conversion of direct photons, the direct virtual photon yield is deduced.

A T_{AA} scaled fit function modified by PHENIX 200 GeV $p+p$ cross section is used for comparison. Fig. 5.9 shows this comparison. For $p_T > 5\ GeV/c$, the direct virtual photon invariant yield follows the T_{AA} scaled $p+p$ cross section [Adl07, Ada10a] within uncertainties (fit function modified by $p+p$ cross section / 42 (mb) $\times$ N_{coll}^{STAR}) which indicates a dominant contribution from the primordial step of hard parton scattering. This conclusion is consistent with all published measurements from other collaborations (Sec. 1.4.2). This consistence indicates that the virtual photon method for direct virtual photon measurement could also be extended to high p_T range and is consistent with the results from the real photon measurement. In the p_T range $1 < p_T < 5\ GeV/c$, an excess of direct virtual photon compared to T_{AA} scaled $p+p$ cross section is observed.

In this p_T range, a theoretical calculation from private communication with Ralf Rapp is also used for comparison. Fig. 5.10 shows this comparison. Within uncertainties, the direct virtual photon invariant yield is consistent with the sum of QGP, hadron gas and primordial contribution. A window for the in-medium effect study is opened.

In Fig. 5.11, an exponential plus the T_{AA} scaled power-law function modified by PHENIX published $p+p$ cross section is used to fit the direct virtual photon invariant yield in $1 < p_T < 3\ GeV/c$. A fitting range scan is applied to calculate the systematic uncertainty. The fit function is shown as Eq. 5.1, where A is converted to dN/dy for $p_T > 1\ GeV/c$ and $N_{coll}^{STAR} = 302.6$. The fitting results can be found in Fig. 5.11. The error bars is the quadrature sum of statistical and systematic errors. An inverse slope parameter $T_{AuAu} = 330 \pm 160^{stat} \pm 137^{syst}$. If the direct photons in Au+Au collisions are of thermal origin, the inverse slope T_{AuAu} is related to the initial temperature T_{init} of the dense matter. In hydrodynamical models, T_{init} is 1.5 to 3 times T_{AuAu} due to the space-time evolution [dP06]. Several hydrodynamical models predict the initial temperature is from $T_{init} = 300\ MeV$ at thermalization time $\tau_0 = 0.6\ fm/c$ to $T_{init} = 600\ MeV$ at

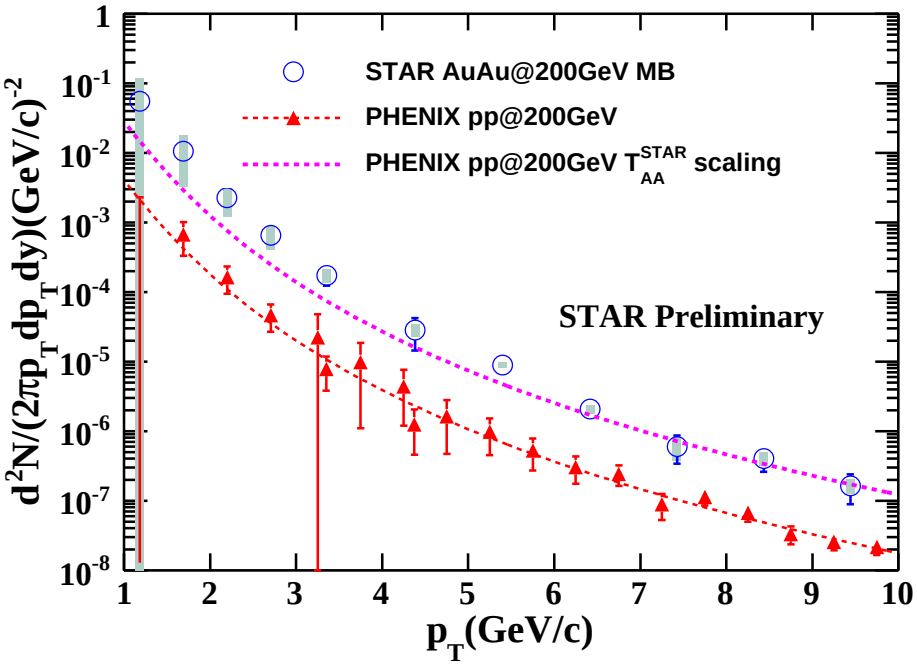

Figure 5.9: The direct virtual photon invariant yield. The statistical and systematic uncertainties are shown by the bars and bands, respectively. Pink curve represents a function modified by PHENIX 200 GeV $p+p$ cross section (red markers, obtained from [Adl07, Ada10a]) scaled by T_{AA} of STAR。

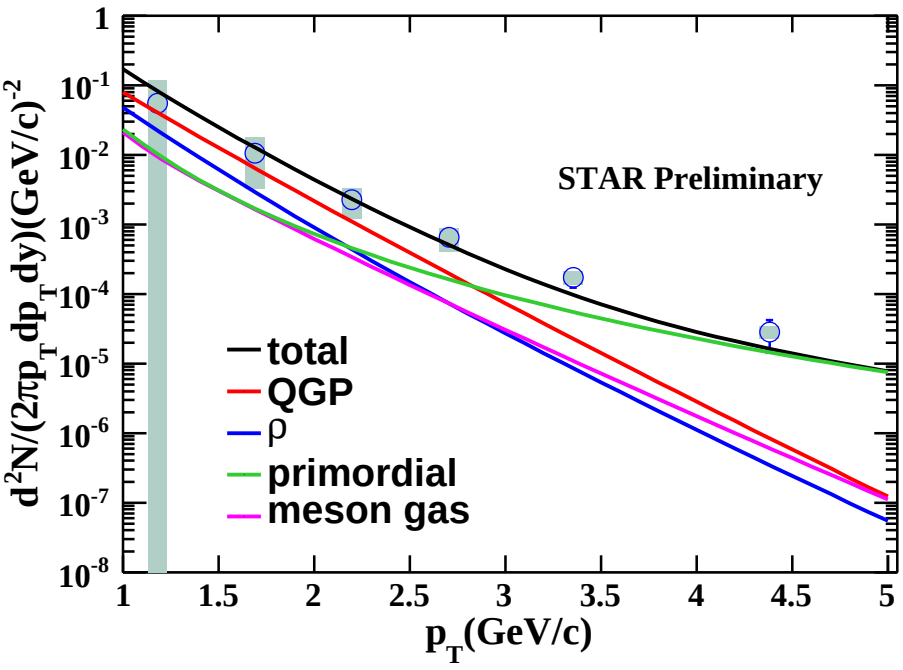

Figure 5.10: The direct virtual photon invariant yield. The statistical and systematic uncertainties are shown by the bars and bands, respectively. Model predictions are from Ralf Rapp's calculation。

$\tau_0 = 0.15\ fm/c$ [dP06]. The precision of the measured slope temperature is not enough. The method to reduce the uncertainty in low p_T will be discussed in Sec. 6.2.

$$Ae^{-p_T/T} + \frac{N_{coll}^{STAR}}{42.} \times A_{pp}(1 + p_T^2/b)^{-n} \tag{5.1}$$

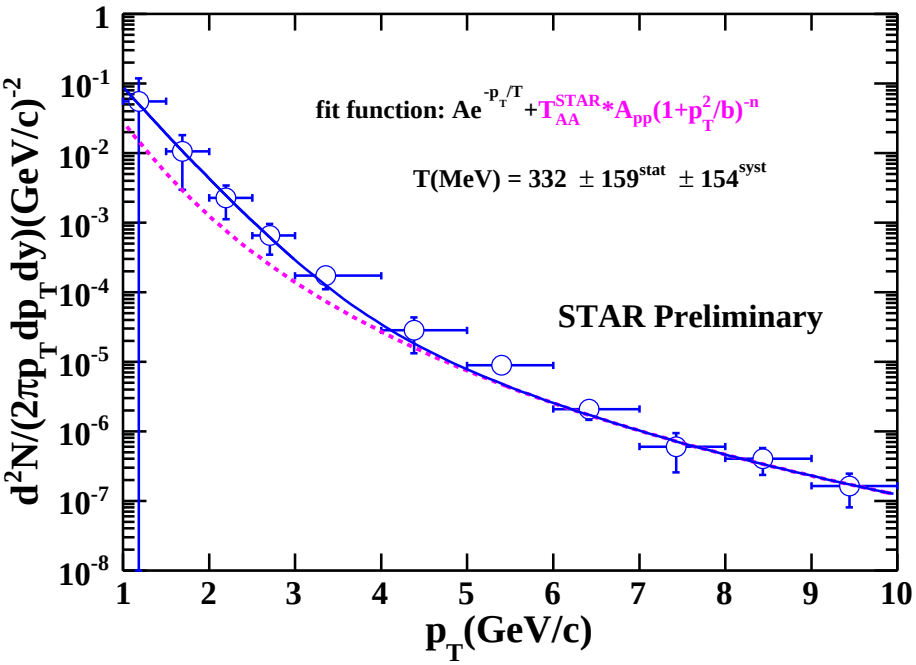

Figure 5.11: An exponential plus modified power-law function (Eq. 5.1) fitting to direct virtual photon invariant yield. The extracted inverse slope parameter shown in the plot. The pink dashed line is the same as it in Fig. 5.9。

CHAPTER 6

Summary and Outlook

6.1 Summary

In summary, the di-electron continuum in Au+Au collisions at $\sqrt{s_{NN}} = 200\ GeV$ within STAR acceptance at RHIC is measured. A combined di-electron continuum is generated based on the Run10 and Run11 Min.Bias data and Run11 EMC triggered data. The p_T differential continuum is measured accordingly.

An enhancement above cocktail is observed clearly in low mass range. Treating the excess as photon internal conversions, the fraction of direct virtual photon in $1 < p_T < 10\ GeV/c$ is obtained from the low p_T combined di-electron continuum and high p_T EMC triggered data. The comparison to NLO pQCD prediction shows a deviation above the model calculation. The uncertainties in $1 < p_T < 2\ GeV/c$ are large due to the uncertainty of η prediction in this range.

The invariant yield of direct virtual photons is deduced in $1 < p_T < 10\ GeV/c$. Compared to T_{AA} scaled $p+p$ cross section, an enhancement is observed in $1 < p_T < 5\ GeV/c$. The invariant yield is consistent with model prediction which includes the contributions from QGP, hadron gas and primordial step. In low p_T range, the dominant contribution comes from the QGP thermal radiation and the thermal from hadron gas. In high p_T range, the invariant yield is consistent with the T_{AA} scaled $p+p$ cross section. This stands for that most of the high p_T direct photons come from the primordial production.

The measurement on direct virtual photon gives two kinematic range: the low p_T measurement allows the study on the in-medium effect, the high p_T measurement provides a region to study the hard parton scattering.

6.2 Outlook

In this study, a dominant systematic uncertainty in low p_T comes from the uncertainty of η source. To get the measurement on η in low p_T, a possible way is to reconstruct η with $\eta \rightarrow \gamma\gamma$ decay channel. Opposite to γ conversion rejection, the events with at least 2 conversion γ need to be selected. If the η measurement can be extended to low p_T, a more precise inverse slope parameter can be obtained since the invariant yield in $1 < p_T < 2\ GeV/c$ significantly impacts it.

Until now, this direct virtual photon analysis is only studied in 0-80% centrality. The centrality dependence study will give R_{cp} measurements on direct virtual photon. Also the direct virtual photon measurement with $p+p$ 200 GeV data collecting at STAR will be a good reference. A study on $p+p$ collisions at 200 GeV will give the comparison with Au+Au results in the same experiment. The R_{AA} measurement can be compared to various model predictions.

As a virtual photon can decay into e^+e^- pair, it can also decay into $\mu^+\mu^-$ pair if $Q^2 > 2M_\mu$. In Run14, the full MTD system (Chap. 3) was installed and took data smoothly. A di-muon trigger which is mentioned in Sec. 3.3.2 is set to trigger on events with at least two μ hits on MTD. Until now, the maximum trigger rate of this trigger label is at about 900 Hz without pre-scale. The single μ trigger also worked well. This allows the measurement of $\mu^+\mu^-$ pair in different kinematics.

Fig. 6.1 is based on Run11 200 GeV MB data (w/o full statistics). Both of them are 2D e^+e^- signal with like-sign background subtraction. In left panel, two different p_T cuts are applied to the electron candidates which is $0.15 < p_{Te1} < 0.3\ GeV/c$ and $p_{Te2} > 1.2\ GeV/c$. The low p_T cut is the μ identification range just via TPC dE/dx while the high one is for MTD selected μ. The right plot uses the MTD p_T cut for both electron candidates. For the low mass region where the direct virtual photon analysis is interested in, $TPC\ \mu \oplus MTD\ \mu$ can give the kinematic from 1.35 GeV/c while $MTD\ \mu \oplus MTD\ \mu$ will start the measurement from 2.4 GeV/c. The fully installed MTD will open a new window to this direct virtual photon analysis. MTD also enables many other important

measurements which can be found in Sec. 3.1.

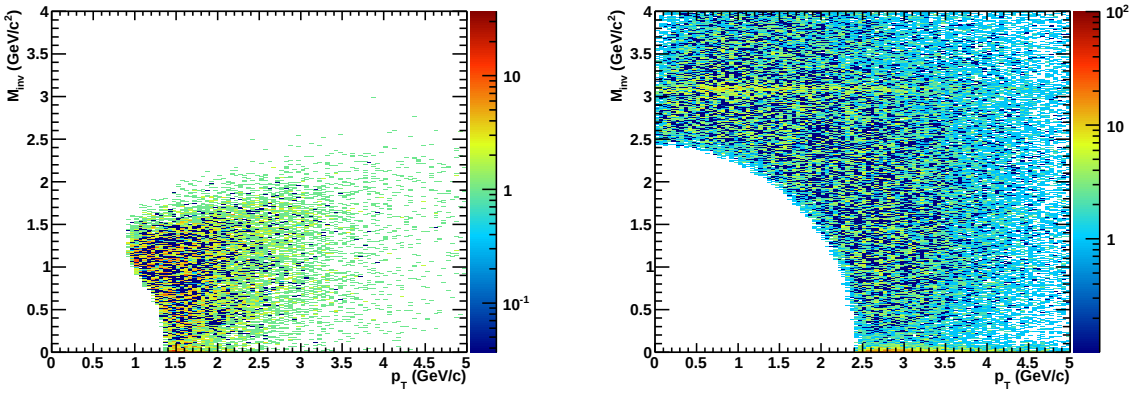

Figure 6.1: The 2D di-electron continuum with like-sign background subtraction based on Run11 200 GeV Au+Au collisions MB data in different kinematics. Left panel: $0.15 < p_{Te1} < 0.3 GeV/c$ and $p_{Te2} > 1.2 GeV/c$. Right panel: $p_{Te1} > 1.2 GeV/c$ and $p_{Te2} > 1.2 GeV/c$

References

[AAA13] A. Adare, S.S. Adler, S. Afanasiev, C. Aidala, N.N. Ajitanand, et al. "Direct photon production in d+Au collisions at $\sqrt{s_{NN}} = 200$ GeV." *Phys.Rev.*, **C87**:054907, 2013.

[Abe06] B. I. Abelev et al. "Identified baryon and meson distributions at large transverse momenta from Au + Au collisions at $\sqrt{s_{NN}} = 200$ GeV." *Phys. Rev. Lett.*, **97**:152301, 2006.

[Ack03] K. H. Ackermann et al. "STAR detector overview ." *Nucl. Instrum. Meth.*, **A499**:624–632, 2003.

[Ada04] John Adams et al. "Identified particle distributions in pp and AuAu collisions at sqrt(NN) = 200 GeV." *Phys. Rev. Lett.*, **92**:112301, 2004.

[Ada05a] John Adams et al. "Experimental and theoretical challenges in the search for the quark gluon plasma: The STAR collaboration's critical assessment of the evidence from RHIC collisions." *Nucl. Phys.*, **A757**:102–183, 2005.

[Ada05b] John Adams et al. "Phi meson production in Au + Au and p + p collisions at s**(1/2) = 200-GeV." *Phys. Lett.*, **B612**:181–189, 2005.

[Ada07] A. Adare et al. "J/ψ production vs centrality, transverse momentum, and rapidity in Au+Au collisions at $\sqrt{s_{\rm NN}}$= 200 GeV." *Phys. Rev. Lett.*, **98**:232301, 2007.

[Ada10a] A. Adare et al. "Detailed measurement of the e^+e^- pair continuum in $p+p$ and Au+Au collisions at $\sqrt{s_{NN}} = 200$ GeV and implications for direct photon production." *Phys.Rev.*, **C81**:034911, 2010.

[Ada10b] A. Adare et al. "Enhanced production of direct photons in Au+Au collisions at $\sqrt{s_{NN}} = 200$ GeV and implications for the initial temperature." *Phys.Rev.Lett.*, **104**:132301, 2010.

[Ada12] L. Adamczyk et al. "Measurements of D^0 and D^* Production in p+p Collisions at $\sqrt{s} = 200$ GeV." *Phys.Rev.*, **D86**:072013, 2012.

[Adc03] K. Adcox et al. "PHENIX detector overview." *Nucl.Instrum.Meth.*, **A499**:469–479, 2003.

[Adl07] S.S. Adler et al. "Measurement of direct photon production in p + p collisions at s**(1/2) = 200-GeV." *Phys.Rev.Lett.*, **98**:012002, 2007.

[Afa12] S. Afanasiev et al. "Measurement of Direct Photons in Au+Au Collisions at $\sqrt{s_{NN}} = 200$ GeV." *Phys.Rev.Lett.*, **109**:152302, 2012.

[Ago03] S. Agostinelli et al. "GEANT4: A simulation toolkit." *Nucl. Instrum. Meth.*, **A506**:250–303, 2003.

[All03] C. E. Allgower et al. "The STAR endcap electromagnetic calorimeter." *Nucl. Instrum. Meth.*, **A499**:740–750, 2003.

[All06] John Allison et al. "Geant4 developments and applications." *IEEE Trans. Nucl. Sci.*, **53**:270, 2006.

[Ams08] C. Amsler et al. "Review of particle physics." *Phys. Lett.*, **B667**:1, 2008.

[And03] M. Anderson et al. "The STAR time projection chamber: A unique tool for studying high multiplicity events at RHIC." *Nucl. Instrum. Meth.*, **A499**:659–678, 2003.

[Arl06] Francois Arleo. "Hard pion and prompt photon at RHIC, from single to double inclusive production." *JHEP*, **0609**:015, 2006.

[Bed03] M. Beddo et al. "The STAR barrel electromagnetic calorimeter." *Nucl. Instrum. Meth.*, **A499**:725–739, 2003.

[Ber03] F. Bergsma et al. "The STAR detector magnet subsystem." *Nucl. Instrum. Meth.*, **A499**:633–639, 2003.

[Bet09] Siegfried Bethke. "The 2009 world average of α_s." *The European Physical Journal C - Particles and Fields*, **64**:689–703, 2009. 10.1140/epjc/s10052-009-1173-1.

[Bic06] H. Bichsel. "A method to improve tracking and particle identification in TPCs and silicon detectors." *Nucl. Instrum. Meth.*, **A562**:154–197, 2006.

[CCH96] E. Cerron Zeballos, I. Crotty, D. Hatzifotiadou, J. Lamas Valverde, S. Neupane, et al. "A New type of resistive plate chamber: The Multigap RPC." *Nucl.Instrum.Meth.*, **A374**:132–136, 1996.

[Cha08] S. Chatrchyan et al. "The CMS experiment at the CERN LHC." *JINST*, **3**:S08004, 2008.

[Cha12] Serguei Chatrchyan et al. "Measurement of isolated photon production in *pp* and PbPb collisions at $\sqrt{s_{NN}} = 2.76$ TeV." *Phys.Lett.*, **B710**:256–277, 2012.

[col] STAR collaboration. "proposal for alarge area time of flight system for STAR.".

[Das09] Debasish Das. "Recent results from STAR experiment in Au+Au collisions at $\sqrt{s_{NN}} = 9.2$ GeV." 2009.

[Don06] Xin Dong. "The time-Of-flight detector for RHIC / STAR and the related physics." *AIP Conf. Proc.*, **865**:332–337, 2006.

[dP06] David G. d'Enterria and Dmitri Peressounko. "Probing the QCD equation of state with thermal photons in nucleus-nucleus collisions at RHIC." *Eur.Phys.J.*, **C46**:451–464, 2006.

[Eng05] J.J. Engelen. "The LHC project: Overview and status." *Czech.J.Phys.*, **55**:B13–B21, 2005.

[FG72] Harald Fritzsch and Murray Gell-Mann. "Current algebra: Quarks and what else?" *eConf*, **C720906V2**:135–165, 1972.

[GKS95] R. Gavai, D. Kharzeev, H. Satz, G.A. Schuler, K. Sridhar, et al. "Quarkonium production in hadronic collisions." *Int.J.Mod.Phys.*, **A10**:3043–3070, 1995.

[Gup98] R. Gupta. "Introduction to Lattice QCD." 1998.

[GV93] L.E. Gordon and W. Vogelsang. "Polarized and unpolarized prompt photon production beyond the leading order." *Phys.Rev.*, **D48**:3136–3159, 1993.

[GW73a] David J. Gross and Frank Wilczek. "Asymptotically Free Gauge Theories. I." *Phys. Rev. D*, **8**:3633–3652, Nov 1973.

[GW73b] David J. Gross and Frank Wilczek. "Ultraviolet Behavior of Non-Abelian Gauge Theories." *Phys. Rev. Lett.*, **30**:1343–1346, Jun 1973.

[Her01] Gunar Hering. "Dielectron production in heavy ion collisions at 158-GeV/c per nucleon." 2001. Ph.D. Thesis (Advisor: Peter Braun-Munzinger).

[HLO03] M. Harrison, T. Ludlam, and S. Ozaki. "RHIC project overview." *Nucl. Instrum. Meth.*, **A499**:235–244, 2003.

[HP74] H and David Politzer. "Asymptotic freedom: An approach to strong interactions." *Physics Reports*, **14**(4):129 – 180, 1974.

[KW55] Norman M. Kroll and Walter Wada. "Internal Pair Production Associated with the Emission of High-Energy Gamma Rays." *Phys. Rev.*, **98**(5):1355–1359, Jun 1955.

[Lan85] L. G. Landsberg. "Electromagnetic Decays of Light Mesons." *Phys. Rept.*, **128**:301–376, 1985.

[Lic95] Peter Lichard. "Formalism for dilepton production via virtual photon bremsstrahlung in hadronic reactions." *Phys. Rev. D*, **51**:6017–6035, Jun 1995.

[Llo05] W. J. Llope. "The large-area time-of-flight upgrade for STAR." *Nucl. Instrum. Meth.*, **B241**:306–310, 2005.

[Lud03] T. Ludlam. "Overview of experiments and detectors at RHIC." *Nucl.Instrum.Meth.*, **A499**:428–432, 2003.

[LZN14] W.J. Llope, J. Zhou, T. Nussbaum, G.W. Hoffmann, K. Asselta, et al. "The STAR Vertex Position Detector." 2014.

[MRS07] Michael L. Miller, Klaus Reygers, Stephen J. Sanders, and Peter Steinberg. "Glauber modeling in high energy nuclear collisions." *Ann.Rev.Nucl.Part.Sci.*, **57**:205–243, 2007.

[Pis82] Robert D. Pisarski. "Phenomenology of the Chiral Phase Transition." *Phys.Lett.*, **B110**:155, 1982.

[Pol73] H. David Politzer. "Reliable Perturbative Results for Strong Interactions?" *Phys. Rev. Lett.*, **30**:1346–1349, Jun 1973.

[Rap02] Ralf Rapp. "Thermal lepton production in heavy ion collisions." 2002.

[Rua09] L. Ruan et al. "Perspectives of a Midrapidity Dimuon Program at RHIC: A Novel and Compact Muon Telescope Detector." *J. Phys.*, **G36**:095001, 2009.

[RW00] R. Rapp and J. Wambach. "Chiral symmetry restoration and dileptons in relativistic heavy ion collisions." *Adv.Nucl.Phys.*, **25**:1, 2000.

[Sha06a] M. Shao et al. "Extensive particle identification with TPC and TOF at the STAR experiment." *Nucl. Instrum. Meth.*, **A558**:419–429, 2006.

[Sha06b] M. Shao et al. "Extensive particle identification with TPC and TOF at the STAR experiment." *Nucl. Instrum. Meth.*, **A558**:419–429, 2006.

[Sil09] Cesar Luiz da Silva. "Quarkonia measurement in p+p and d+Au collisions at s**(1/2) = 200- GeV by PHENIX Detector." *Nucl.Phys.*, **A830**:227C–230C, 2009.

[Sim08] F. Simon et al. "The Forward GEM Tracker of STAR at RHIC." 2008.

[SMS06] Torbjorn Sjostrand, Stephen Mrenna, and Peter Skands. "PYTHIA 6.4 physics and manual." *JHEP*, **05**:026, 2006.

[STA] Bingchu Huang for the STAR collaboration. "J/ψproduction in $Au + Au$collisions at center of mass energy = 200-GeV." Acta Phys. Pol. B Proc. 5, 471, (2012).

[Tan09] Zebo Tang et al. "Spectra and radial flow at RHIC with Tsallis statistics in a Blast-Wave description." *Phys. Rev.*, **C79**:051901, 2009.

[Ver09] E. Vercellin. "The ALICE experiment: Overview and status." *AIP Conf.Proc.*, **1120**:151–156, 2009.

[VZ08] Ivan Vitev and Ben-Wei Zhang. "A Systematic study of direct photon production in heavy ion collisions." *Phys.Lett.*, **B669**:337–344, 2008.

[Wil13] Martin Wilde. "Measurement of Direct Photons in pp and Pb-Pb Collisions with ALICE." *Nucl.Phys.*, **A904-905**:573c–576c, 2013.

[Xu08] Yi-chun Xu et al. "Calibration of ionization energy loss at relativistic rise with STAR Time Projection Chamber." 2008.

Acknowledgements

My gratitude goes to Prof. Cheng Li who has been my adviser since I was a undergraduate student. He introduced me to high energy nuclear physics and gave me very good suggestion once I needed to make choice. I would like to thank Prof. James Dunlop, Prof. Zhangbu Xu, Prof. Lijuan Ruan and the China Scholarship Council for offering me the opportunity to study at BNL, the excellent and wonderful place for the research on relativistic heavy ion collision physics.

I would especially thank Prof. Lijuan Ruan. In the three years at BNL, she guided me through all the details of my research as co-adviser. Her perpetual energy and enthusiasm in research had motivated me. I benefit a lot from her. I would not be here without her help. I would like to thank Prof. Zhangbu Xu. His broad academic view and frontier academic thought helped me a lot among every discussion. His suggestions will always point to the key part of the research. I also appreciate the important assistances from Prof. Zebo Tang, Prof. Yichun Xu who guided me to the heavy ion collision physics and Dr. Yi Zhou who advised me in the detector study. I would like to thank Dr. Bingchu Huang. He helped me a lot not only on my analysis but also on my living at BNL.

I would like to thank Prof. Yifei Zhang, Dr. Jie Zhao, Wangmei Zha and Yi Guo for enjoyable corporation on work and abundant helpful discussions. Especially thank Prof. Bill Christie, Prof. W.J.Llope and Robert Soja for their supports on my detector research. Thanks to Prof. Shusu Shi, Dr. Hao Qiu, Dr. Hongwei Ke, Dr. Hui Wang, Dr. Xiangli Cui, Dr. Lizhu Chen, Dr. Yuhui Zhu, Dr. Lixin Han, Qiye Shou, Xueye Hu, Chengming Du, Yan Yang, Hui Zhang, Shuai Yang, Yifei Xu, Zhengqiao Zhang and Jinlong Zhang who gave me a nice period in BNL. Thanks to all STAR collaborators for providing such a beautiful detector and the STAR Light Flavor Spectra physics working group especially the convenors.

I appreciate the High Energy Physics Group at USTC. Thanks to Prof. Zhengguo Zhao, Prof. Hongfang Chen, Prof. Zizong Xu, Prof. Xiaolian Wang, Prof. Ziping Zhang,

Prof. Qun Wang, Prof. Ming Shao and Dr. Yongjie Sun. I would like to thank USTC and all my friends. Thanks to all the physicists who I met and discussed with.

At the end, my deepest gratitude goes to my family. Thanks to your understanding, your supporting, your encouraging and your dedication. I love you so much. Wish you all the best. I would dedicate the thesis to my family especially to my grandpa.

Talks and publications

Talks:

1. Direct virtual photon and dielectron production in Au+Au collisions at $\sqrt{s_{NN}}$ = 200 GeV at STAR

   XXIV International Conference on Ultrarelativistic Nucleus-Nucleus Collisions(Quark Matter 2014), 19-24 May 2014, Darmstadt, Germany

2. Direct Virtual Photon Production in AuAu Collisions at 200GeV from STAR

   Workshop on MTD and HFT and related physics, September 2013, Hefei, China

3. Performance of the Muon Telescope Detector (MTD) in STAR at RHIC

   RHIC & AGS Annul Users' Meeting, June 2013, BNL, NY, USA

4. Performance of the Muon Telescope Detector (MTD) in STAR at RHIC

   XXIII International Conference on Ultrarelativistic Nucleus-Nucleus Collisions(Quark Matter 2012), 13-18 August 2012, DC, USA

5. GEM detector and readout methods

   Micro-Pattern Gas Detector Workshop, May 2010, Lujiang, China

Main Publications:

1. Calibration and performance of the STAR Muon Telescope Detector using cosmic rays

   Chi Yang, et al.

   Nucl.Instrum.Meth. A 762, 1 (2014) DOI: 10.1016/j.nima.2014.05.075

2. Direct photon production in Au+Au collisions at $\sqrt{s_{NN}} = 200$ GeV at STAR

   Chi Yang (for STAR Collaboration)

   Nucl.Phys. A (2014) DOI: 10.1016/j.nuclphysa.2014.08.042

3. Dielectron Azimuthal Anisotropy at mid-rapidity in Au+Au collisions at $\sqrt{s_{NN}}$ = 200 GeV

   L. Adamczyk et al. (STAR Collaboration)

   Phys.Rev. C90 (2014) 6, 064904 DOI: 10.1103/PhysRevC.90.064904

4. Dielectron Mass Spectra from Au+Au Collisions at $\sqrt{s_{NN}}$ = 200 GeV

   L. Adamczyk et al. (STAR Collaboration)

   Phys.Rev.Lett. 113 (2014) 2, 022301 DOI: 10.1103/PhysRevLett.113.049903

5. Systematic study of the experimental measurements on ratios of different v states

   Wangmei Zha, Chi Yang, Bingchu Huang, Lijuan Ruan, Shuai Yang, Zebo Tang, and Zhangbu Xu

   Phys. Rev. C 88, 067901 DOI: 10.1103/PhysRevC.88.067901

6. The STAR Vertex Position Detector

   Llope, W.J., et al.

   Nucl.Instrum.Meth. A759 (2014) 23-28 DOI: 10.1016/j.nima.2014.04.080

7. Energy dependence of moments of net-proton multiplicity distributions at RHIC

   L. Adamczyk et al. (STAR Collaboration)

   Phys.Rev.Lett. 112 (2014) 3, 032302 DOI: 10.1103/PhysRevLett.112.032302

8. Neutral pion cross section and spin asymmetries at intermediate pseudorapidity in polarized proton collisions at $\sqrt{s}$ = 200 GeV

   L. Adamczyk et al. (STAR Collaboration)

   Phys.Rev. D89 (2014) 1, 012001 DOI: 10.1103/PhysRevD.89.012001

9. Fluctuations of charge separation perpendicular to the event plane and local parity violation in $\sqrt{s}$ = 200 GeV Au + Au collisions at the BNL Relativistic Heavy Ion Collider

L. Adamczyk et al. (STAR Collaboration)

Phys.Rev. C88 (2013) 6, 064911 DOI: 10.1103/PhysRevC.88.064911

10. Freeze-out dynamics via charged kaon femtoscopy in $\sqrt{s} = 200$ GeV central Au+Au collisions

L. Adamczyk et al. (STAR Collaboration)

Phys.Rev. C88 (2013) 3, 034906 DOI: 10.1103/PhysRevC.88.034906